Metal-Semiconductor Transition Materials: FeS and VO_2 Thin Films by RF Reactive Sputtering

Dissertation zur Erlangung des Doktorgrades

der Naturwissenschaften von

Ganhua Fu

Betreuer: Prof. Dr. B. K. Meyer

I. Physikalisches Institut

Justus-Liebig-Universität Gießen

Gießen, June 2007

Contents

Chapter 1 Introduction

Metal-nonmetal transition in many transition-metal oxides and sulfides has been the subject of considerable experimental and theoretical work for over sixty years. Many reviews and books are published on this subject [1-6]. From the theoretical side, different mechanisms, such as Anderson transition, Peierls transition and Mott-Hubbard transition were proposed to clarify the metal-nonmetal transition. From the experimental side, numerous systems are found to show this transition and the physical properties around the transition are extensively investigated. A metal-nonmetal transition is accompanied by the abrupt change in some physical properties of systems, such as the electrical conductance, optical transmittance, and so on. By detecting the variation of these physical properties around the transition, it is possible to make some switching devices triggered by heat, pressure, etc. In this work, two Metal-Semiconductor Transition (MST) systems, VO_2 and FeS in the thin film state, were investigated.

Vanadium Oxide

Vanadium dioxide (VO_2) exhibits a reversible MST at 68 ^oC [7]. Below this transition temperature, it is a narrow gap (0.65 eV) semiconductor with a monoclinic structure. Above 68 ^oC, it transforms into a tetragonal (TiO_2) structure and exhibits metallic properties. This transition is accompanied by the abrupt change in the electrical resistivity, optical transmittance and reflectance. For example, the VO_2 film in the infrared region has a very low transmittance in the metallic phase but rather high transmittance in the semiconducting phase. This has lead to many applications of the material in infrared light (IR)-switching or bolometric devices [8, 9] or especially as intelligent energy conserving window coating (smart window) [10].

The smart window plays an important role in future glazings [11]. Upon a change in electrical field, light intensity or temperature, it exhibits a large change in optical properties totally or partly over the visible and solar spectrum. The smart window can control the flow of heat through a window and thus has a considerable energy advantage over that of conventional double glazed windows. Applications include glazings in

buildings, vehicles, aircrafts, spacecrafts and ships. The smart window is classified into two major types: non-electrically activated and electrically activated. The electrically activated devices have the advantage of user or automatic control. The phase dispersed liquid crystals, dispersed particle systems and electrochromics belong to this type. The non-electrically activated type has the advantage of being self-regulating with local control. This type includes some photochromic, thermochromic and thermotropic materials.

VO_2 is one of the most potential materials for the application as non-electrically activated smart window. For an application as smart window coating, the transition temperature has to be lowered to about 25 ^oC, the luminous transmittance T_{lum}, the transmittance of the semiconducting phase in the visibe region, should be as high as possible and the color of the VO_2 thin film should be human comfortable, for example, colorless or blue. The required reduction of the transition temperature can be achieved by the substituting doping. Tungsten is the most effective dopant [12, 13], with an effect of ≈ –23 K/at.% W, up to concentrations of a few percent. Other dopants are, e.g. fluorine (-20 K/at.% F) [14], rhenium (-18 K/at.% Re) and molybdenum (-10 K/at.% Mo) [15]. The reduction of the transition temperature by the replacement of V^{4+} with higher-valence ions was explained with a charge-transfer mechanism [16]. The luminous transmittance can be enhanced by depositing a TiO_2, ZrO_2, or SiO_2 layer on the VO_2 layer as antireflection layer [17-19]. M. S. R. Khan et al. claimed that the electrochemical lithiation of the VO_2 thin film not only changed its color to be blueish but also increased its luminous transmittance [20]. This method, however, is not available for the large scale production. In this work, Li and H were tried to dope into VO_2 thin films to modify the switching behavior by reactive sputtering. In addition, the thermal stability of VO_2 thin films was investigated.

Iron sulfide

Iron sulfide (FeS) shows a MST at around 147 ^oC [21]. It is associated with the structural transition from the NiAs type structure at high temperatures to the closely related superstructure at low temperatures. The transition temperature is sensitive to the composition. With the decrease of the temperature through this transition temperature there is an abrupt decrease by two orders of magnitude in the electrical conductivity and FeS

transforms from a metal into a semiconductor. This is probably accompanied by the change of the optical transmittance and reflectance, which has never been investigated. The prerequisite for studying the optical properties is the successful preparation of FeS films because the bulk material is too thick to measure the transmittance for some nontransparent materials. However, FeS films have never been prepared although it is still important for understanding of this material. Here we present the deposition and characterization of FeS films by the reactive sputtering.

The plan of this thesis is as follows. Chapter 2 first introduces the principles and instrumentation of the deposition and characterization techniques used in this work. The structure of FeS is briefly introduced in Chapter 3. Chapter 4 reports the deposition and characterization of FeS films. Following the short introduction of VO_2 in Chapter 5, the Li and H doping and thermal stability of VO_2 thin films are reported in Chapter 6. At the end a short summary is given in Chapter 7.

Chapter 2 Preparation and characterization techniques: principles and instrumentation

In the present study, radio frequency reactive sputtering was used to deposit FeS and VO_2 thin films. The sputtered films were characterized by several techniques. X-ray diffraction and reflectivity were employed for structural characterization. The surface and morphology analysis was accomplished by scanning electron microscopy, respectively. Energy-dispersive X-ray analysis, Rutherford backscattering spectroscopy, elastic recoil detection analysis and secondary ion mass spectrometry were utilized to examine the composition. The optical and electrical properties of the films were determined by optical transmittance measurements and electrical measurements by van der Pauw technique, respectively.

In this chapter, the principles and instrumentation of these techniques are briefly described.

2.1 Radio frequency reactive sputtering

Sputtering provides a very useful method for preparing a wide range of thin films with the good control over film properties. It is widely used in industry from microelectronics to decorative coating of automobiles.

When a solid surface is bombarded with energetic particles such as accelerated ions, surface atoms of the solid are partly scattered backward due to collisions between the surface atoms and the energetic particles. This phenomenon is called sputtering, which is widely used for thin film deposition, surface cleaning and etching, etc.

The basic sputter deposition system is composed of a pair of planar electrodes, as shown in Fig. 2.1. One of the electrodes is the cold cathode and the other is anode. The front surface of the cathode is covered with the target material to be sputtered. The substrate is placed on the anode. The sputter chamber is filled with the sputter gas, typically Argon. The glow discharge is maintained under the application of the voltage between the electrodes. The Ar^+ ions generated in the glow discharge are accelerated towards the cathode (target). The bombardment of the target by these energetic positive ions causes the

removal of target atoms. These target atoms deposit on the substrate so the thin film is formed. In this process, no chemical reaction happens between the gas and the target atoms. However, if at least one reactive gas (e.g. Oxygen or Nitrogen) is added in chamber besides Ar, the reactive gas will react with target atoms forming a compound layer on the substrate. This technique is known as reactive sputtering.

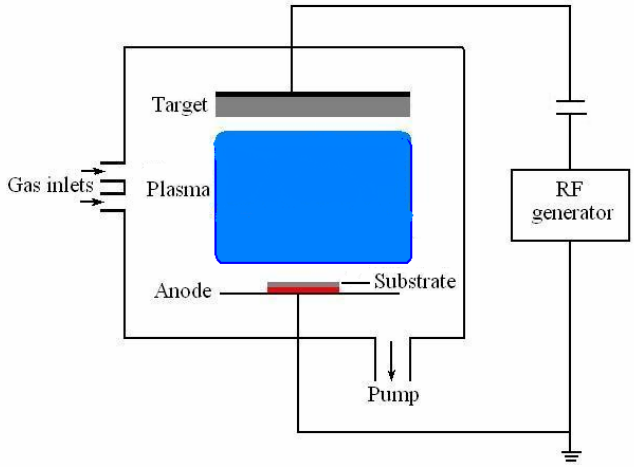

Figure 2.1 RF reactive sputter deposition system [22].

If the applied potential between the cathode and anode is constant with time, the process is called DC sputtering, by which the highly electrically conductive materials like metallic targets can be sputtered. For the insulating targets, however, the glow discharge in this DC sputtering system, can not be sustained because the surface of target will charge up so that the fluxes of positive ions and electrons to the surface become equal, regardless of the potential applied to the electrode backing the insulating target, and then these ions and electrons recombine on the surface. In this case, a radio frequency (RF) voltage is applied to the targets, which avoids the charge on the targets. This is called RF sputtering.

Figure 2.1 illustrates the RF reactive sputtering system used in the present work. The complete sputter system basically consists of five parts: the RF generator, pumping system, sputter chamber, gas inlet system and matching unit, which is designed to achieve an efficient energy transfer from the RF generator to the sputter chamber. In our sputter apparatus, the distance between the target and substrate is approximately 8 cm. The RF generator is used to create a dense glow discharge between the target and the substrate, and to cause a bias potential to build up on the target surface. The positively charged ions in

the plasma are, by several orders of magnitude, heavier than the negatively charged electrons. While the electrons can follow and neutralize positive charges, the ions no longer follow the high frequency switching, particularly in the radio frequency (13.56 MHz) regime, leading to an unaltered negative self biasing of the target, as shown in Fig. 2.2 [23]. The negative bias potential of the target results in the ion bombardment.

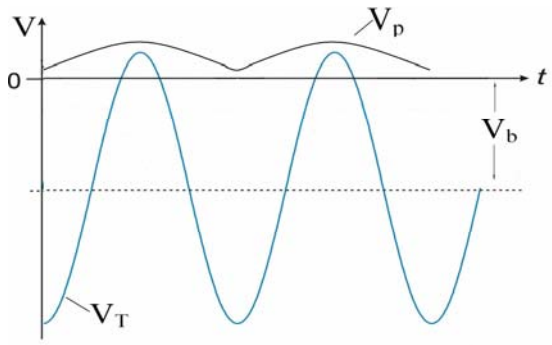

Figure 2.2 The target potential (V_T) and plasma potential (V_P) in a RF sputter process as a function of time, and the self bias potential of the target, V_b, with respect to the ground.

For more details of sputtering please read refs. [24-26].

2.2 Characterization techniques

2.2.1 X-Ray diffraction and reflectivity

X-ray diffraction

X-ray Diffraction (XRD) is a powerful non-destructive technique for characterization of crystalline materials. It provides the information on structure, phase, preferred crystal orientation (texture) and other structural parameters, such as average grain size, crystallinity, strain and crystal defects.

When a monochromatic X-ray beam with wavelength λ, on the order of lattice spacing d, is projected onto a crystalline material at an angle θ, X-ray diffraction peaks are produced by constructive interference of monochromatic beam scattered from each set of lattice planes at specific angles. Constructive interferences give the diffraction peaks according to Bragg's law,

$$2d\sin\theta = n\lambda \tag{2.1}$$

By varying the angle θ, the Bragg's Law condition is satisfied by different d-spacings in crystalline materials. Plotting the angular positions and intensities of the resultant diffracted peaks of radiation produces a pattern, which is characteristic of the material.

The full width at half maximum (FWHM) of the peak, $\Delta(2\theta)$ (in radians), is a measure of the grains size b in a polycrystalline film or the mosaic blocks in an epitaxial layer, as described by Scherrer's formula:

$$b = \frac{0.89\lambda}{\Delta(2\theta)\cdot\cos(\theta)} \tag{2.2}$$

When the grains are larger than the film thickness, h, then $b=h$.

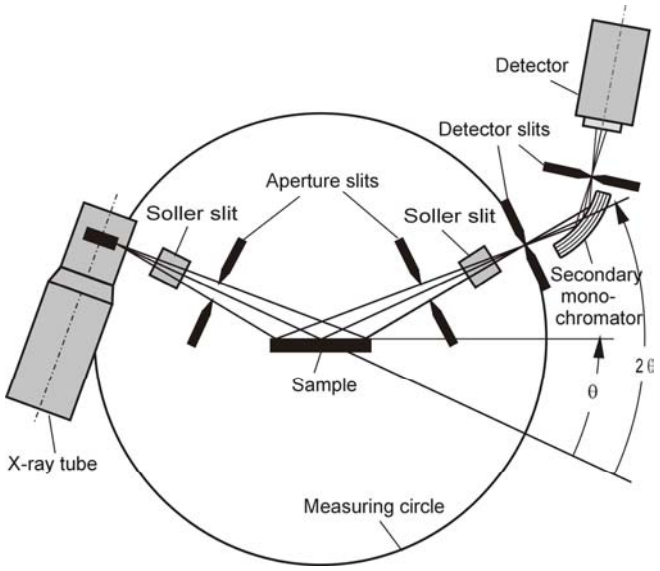

Figure 2.3 Schematic representation of Bragg-Brentano powder diffractometer, Siemens D5000.

Figure 2.3 shows the schematic representation of a standard Bragg-Brentano powder diffractometer, Siemens D5000, with Cu K_α (λ= 0.15418 nm) radiation and a scintillation detector. The X-ray tube was typically operated at a voltage of 40 kV and a current of 20 mA. In this work, two scan modes, θ-2θ scan and ω-scan, were used for structural characterization. For the θ-2θ scan, the detector is rotated twice as fast and in the same direction around the diffractometer axis as the sample. This technique is also called locked-coupled scan. In θ-2θ scan, the reflections from the planes parallel to the substrate surface are detected. This allows to determine the orientation along the growth direction of

an epitaxial or polycrystalline films with respect to the substrate. In ω-scan, also called rocking-curve scan, the detector is fixed in position (2θ) with wide open entrance slits and the sample is rotated by a small angle around the Bragg angle θ. FWHM of the rocking-curve is a direct measure of the range of orientations present in the crystal. Thus, it is usually used for evaluating the out-of-plane ordering of the epitaxial layers.

X-ray reflectivity

X-ray Reflectivity (XRR), a technique related to X-ray diffraction, is now becoming a widely used tool for the characterization of thin film and multilayer structures. Using a simulation or the least-squared fit of the reflectivity pattern, one can obtain accurate information of thickness, interface roughness and layer density for either crystalline or amorphous thin films or multilayers.

The index of refraction of light in the X-ray range in any media can be written as

$$n = 1 - \delta - i\beta \tag{2.3}$$

where δ is the dispersive term and β the absorptive term (both in the order of 10^{-6}).

When X-rays hit the smooth surface of a sample at a critical incidence angle θ_c, the total reflection happens. Neglecting absorption (β=0), the X-ray critical angle θ_c is given by

$$\cos\theta_c = n \tag{2.4}$$

Since θ_c is very small, Equation (2.4) leads, on expansion of the cosine for small angles, to

$$\theta_c \approx \sqrt{2\delta} \sim \sqrt{\rho\left(Z + f'\right)}\lambda \tag{2.5}$$

where ρ is the mass density of the sample, Z is the atomic number and f' is the real (dispersion) part of the dispersion corrections and λ is the wavelength of X-rays.

Now let us consider a thin film on a substrate. When the incident angle θ_i of the incoming X-ray wave exceeds θ_c for the layer, the reflectivity will show oscillations as function of θ_i due to interferences of waves reflected from the top surface and waves reflected from the interface. The thickness of the film d is related to the maxima positions θ_m by

$$\frac{1}{2}(2m+1)\lambda = 2d\sqrt{\theta_m{}^2 - \theta_c^2} \tag{2.6}$$

where m is an integer.

For XRR measurements, a controllable beam stop and a metal absorber for reducing the too high intensity of the totally reflected X-rays are added, as illustrated in Fig. 2.4.

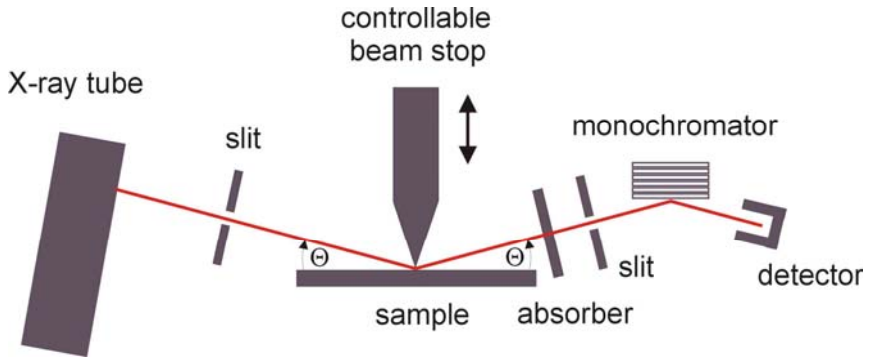

Figure 2.4 The illustration of the setup for X-ray reflectivity

.

For more information about XRD and XRR please go to refs. [27, 28].

2.2.2 Scanning electron microscopy

Scanning electron microscopy (SEM) is a widely used technique to study surface morphology and topography.

In a SEM a finely focused electron beam scanned across the surface of the sample generates secondary electrons, backscattered electrons, and characteristic X-rays. These signals are collected by detectors to form images of the sample displayed on a cathode ray tube screen. Inelastic electron scattering caused by the interaction between the sample's electrons and the incident electron beam results in the emission of low-energy electrons from near the sample's surface. These dislodged electrons from the sample's surface are known as secondary electrons. Secondary electron imaging provides high-resolution imaging of fine surface morphology. Backscattered electrons are produced by the elastic interactions between the sample and the incident electron beam. Some of the incident electrons may strike an atomic nucleus and bound back into the vacuum. Compared with secondary electrons, these electrons have high energy, known as backscattered electrons. Backscattered electron imaging provides elemental composition variation, as well as surface topography. The generated X-rays are the basis of Energy-dispersive X-ray spectroscopy technique, which will be discussed later.

For the scanning of insulating samples, a conductive coating should be placed on it to avoid the charging. Field Emission Scanning Electron Microscope (FESEM) solves this

problem. In FESEM, the electron gun is a field-emission cathode, which provides a narrower probing beam, resulting in both improved spatial resolution and minimized sample charging.

In the present study, the LEO SEM was operated at the acceleration voltage of 3-15 kV to observe the surface as well as cross-sectional morphology of the films.

The reader who is interested in more details of SEM is referred to refs. [29, 30].

2.2.3 Energy-dispersive X-ray spectroscopy

Energy-dispersive X-ray spectroscopy (EDXS) is a technique for measuring the elemental composition of the material. It is usually used in conjunction with a SEM. Most of the chemical elements can be identified by EDXS. The only limit is whether the particular type of detector window registers soft X-rays of the light elements. Thus detectors equipped with Be windows only enable detection of elements of atomic number $Z \geq 11$ (Na), whereas detectors with ultrathin light-element windows can even be used for analysis of boron ($Z=5$). The X-rays are generated in a region about 2 microns in depth.

When a material is hit by electrons, different inelastic scattering processes can also be observed as a result of direct interaction between the primary energetic electrons and the electrons in inner shells and the valence or conduction band of the material, as shown in Fig. 2.5. First, the primary electrons transfer energy to the tightly bound core electrons or the more loosely bound valence electrons, which thus are excited to higher unoccupied energy states in the conduction band (process 1), or even be set free into the vacuum (process 2). Thus, a hole is generated and the atom becomes ionized. After a certain dwell time of excitation the system relaxes and the hole state in the originally excited level is filled with an electron from an outer shell. There is a certain probability that the energy set free by this process leads to the excitation of characteristic X-rays (process 3). The energy of the emitted X-rays is measured to detect the elements in the material. This technique is called EDXS. Or the energy is given to an electron in the same or an outer shell, resulting in the emission of Auger electrons (process 4), a process competing with the emission of X-rays. The sum of both the fluorescence yield of X-rays and probability of Auger electron emission is always equal to 100%. The fluorescence yield of X-rays increases with atomic number Z, while the portion of emitted Auger electrons behaves in the opposite manner.

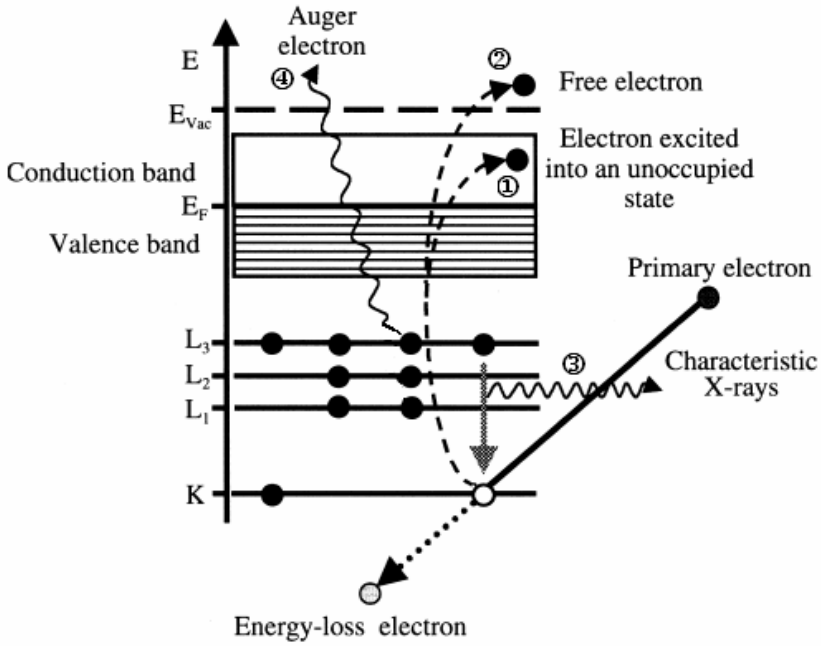

Figure 2.5 Atomistic view of interaction processes between incident high-energy electrons and electrons of an individual atom [31].

For ionization of the K shell and filling of the remaining hole by electrons from the L or M shells, emission of so-called K_α or K_β X-rays occurs. And the filling of the hole in the L shell by electrons from the M or N shells gives rise to the emission of L_α or L_β radiation, respectively. For heavier elements electrons from more outer shells can also occupy the holes, although not all conceivable transitions between the existing electronic energy levels are allowed. The physically allowed transitions are determined by the quantum-mechanical selection rules.

The energies of the X-ray quanta of the K and L series for an element (Z) can be calculated by equations:

$$E\left(K\xi(n)\right) = E_{A(n+1)} - E_K = hcR(Z-1)^2\left(1/n^2 - 1\right) \tag{2.7}$$

and

$$E\left(L\xi(n)\right) = E_{A(n+2)} - E_L = hcR(Z-7.4)^2\left(1/n^2 - 1/2^2\right) \tag{2.8}$$

where ξ(n)=α, β, γ,…, A(n)=K, L, M, …, and n=1, 2, 3, …, R is the Rydberg constant, h is Planck's constant, and c is the velocity of light.

For a compound A_mB_n, the concentration ratio can be given by formula:

$$\frac{n}{m} = \frac{N_A}{N_B} = k_{AB} \frac{I_A}{I_B} \tag{2.9}$$

where I_A and I_B are the measured intensities of element *A* and *B* and k_{AB} is the Cliff-Lorimer factor, which is not a constant and depends on the acceleration voltage, the detector efficiency and several other factors.

More details of EDXS are given in ref. [31].

2.2.4 Secondary ion mass spectrometry

Secondary ion mass spectrometry (SIMS) is often used to conduct mass spectrum analysis of all elements in the periodic table and depth profile analysis up to some μm depth in materials.

In SIMS the surface of the sample is subjected to the bombardment by high energy ions. This leads to the ejection (or sputtering) of both neutral and charged (+/-) species from the surface, including secondary electrons, Auger electrons, photons, neutrals, excited neutrals, positive secondary ions. The emitted ions can be detected and mass analysed to determine what the sample is made of. This is the basis of the SIMS technique. The most commonly employed incident ions used for bombarding the sample are Argon and Cesium ions (Ar^+ and Cs^+) but other ions (e.g. alkali metal ions, Ga^+) are preferred for some applications.

When a heavy energetic particle such as an Argon ion (typically 1 to 5 keV) hits a surface, it will not be stopped short by the first layer of atoms but continue into the surface until it comes to a halt as a result of energy loss in atomic and electronic scattering. Along its way the ion displaces some atoms from their original positions in the solid structure, which displace others as they recoil, and so on, resulting in a complex sequence of collisions. Depending on the energy absorbed in an individual collision, some atoms are permanently displaced from their normal positions, wheras others return elastically after temporary displacement. This sequence is called a collision cascade and is illustrated schematically in Fig. 2.6, along with some other processes. The erosion of the sample by the ion beam can provide a depth profile of the sample, and the ion beam can be scanned

over the surface to provide an image of the presence of particular elements or molecules on the surface. The eroding nature of the beam makes SIMS a destructive technique.

The SIMS technique is the most sensitive of all the commonly employed surface analytical techniques because of the inherent sensitivity associated with mass spectrometric-based techniques.

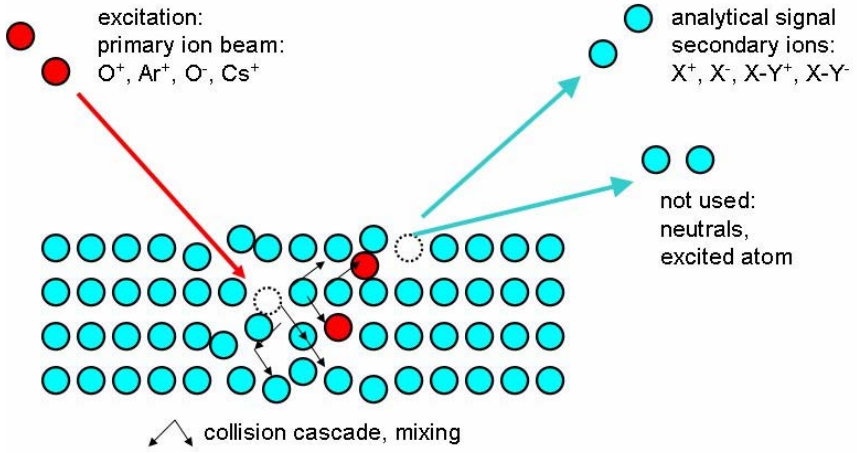

Figure 2.6 The schematic diagram of the sputtering process in SIMS.

The reader who is interested in more details of SIMS is referred to refs. [32, 33].

2.2.5 Rutherford Backscattering Spectroscopy

Rutherford back-scattering spectroscopy (RBS) is one of the most frequently used techniques for quantitative analysis of composition, thickness, and depth profiles of thin solid films.

In RBS, a beam of monoenergetic ions, usually H^+ or He^+ of typical energy of 0.5 to 2.5 MeV, is directed at a target, and the energies of the ions which are scattered backwards are analyzed. In the back-scattering collision, energy is transferred from the impinging particle to the stationary target atom. Figure 2.7 shows the collision kinematics between a projectile atom (M_p, Z_p) and a target atom (M_r, Z_r) in RBS. The energy ratio between the projectile energy E_1 after collision and the energy E_0 before collision, derived from binary collision theory, is

$$K = \frac{E_1}{E_0} = \left[\frac{\left(M_r^2 - M_p^2 \sin^2\theta\right)^{1/2} + M_p \cos\theta}{M_r + M_p} \right]^2 \tag{2.10}$$

The energy ratio E_1/E_0, called the kinematic factor K, shows that the energy after scattering depends on the mass M_p of the projectile, the mass M_r of the target atom, and the scattering angle θ (i.e. the angle between incident and scattered beams). If M_p, E_0, and θ are known, M_r may be determined and the target element is identified.

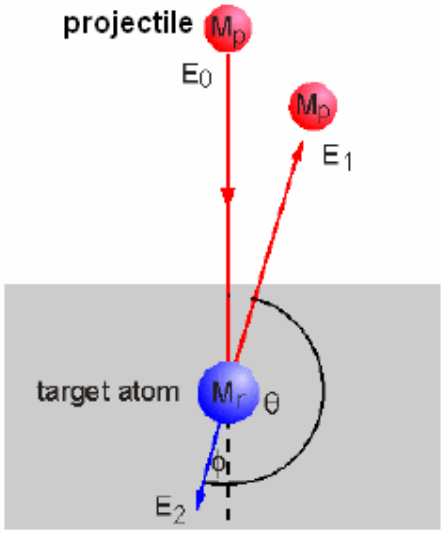

Figure 2.7 Collision kinematics between a projectile atom M_p and a target atom M_r in RBS.

For an ion beam with the total number Q of ions impinging on a target, the number, Q_r, of ions backscattered from target atoms and registered in the detector gives the concentration of the corresponding element. It is given by:

$$Q_r = Q N_r \sigma_r \Delta\Omega \tag{2.11}$$

where N_r is the areal density of target atoms in the sample (atom cm^{-2}), σ_r the differential scattering cross-section (cm^2 sr^{-1}) and $\Delta\Omega$ is the solid angle for the detector. The differential scattering cross-section describes the probability of a projectile being scattered by a target atom through an angle, θ, into a solid angle, $d\Omega$, centered about θ. If the interaction potential between the projectile and the target atom during scattering is given by the Coulomb potential, the cross-section is given by the Rutherford formula:

$$\sigma = \left(\frac{Z_p Z_r e^2}{16\pi\varepsilon_0 E_0} \right)^2 \frac{4\left[\left(M_r^2 - M_p^2 \sin^2\theta\right)^{1/2} + M_r \cos\theta\right]^2}{M_r \sin^4\theta \left(M_r^2 - M_p^2 \sin^2\theta\right)^{1/2}} \tag{2.12}$$

For a compound film A_mB_n, the composition can be calculated from Eq. (2.11) to be:

$$\frac{n}{m}=\frac{N_B}{N_A}=\frac{Q_B}{Q_A}\frac{\sigma_A}{\sigma_B} \tag{2.13}$$

The energy of the backscattered ion is given by Eq. (2.10) only for scattering by an atom at the target surface. In RBS, however, the ion beam penerates the target and an ion might be backscattered by target atoms at any point along its path, as shown in Fig. 2.8. In the energy region used for RBS the ion trajectory is a straight line (apart from the backscattering collision) along which the ions lose energy primarily through excitation and ionization of atomic electrons (electronic energy loss). The energy loss per unit path length, *dE/dx*, is called the stopping power. These additional energy losses broaden the peak to be observed in an RBS spectrum of a thin film.

In this method, projectiles scattered by angles larger than 90° are analyzed. Because projectiles with mass M_p can only be backscattered from a target atom with mass M_r if $M_p < M_r$, light projectiles such protons and He ions are usually used in RBS. High back-scattered energies and large backscattering cross-sections are found for heavy target atoms. RBS is, therefore, well suited to the analysis of heavy target elements, but its sensitivity for light elements is poor.

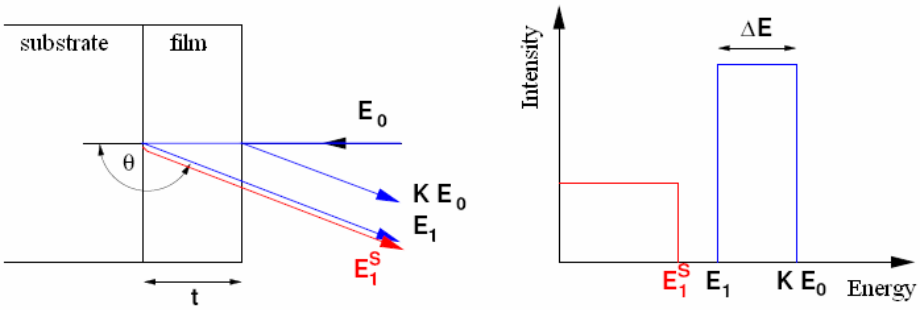

Figure 2.8 Schematic representation how the depth corresponds to different energy signals. This difference in energy can then quantify the amount of a particular element in the sample.

For more information of RBS, please go to ref. [31].

2.2.6 Elastic Recoil Detection Analysis

Elastic Recoil Detection Analysis (ERDA) is mainly used for light element profiling, including hydrogen, which is hardly possible by RBS.

In ERDA the sample is irradiated with high energetic heavy ions under grazing conditions. The energy as well as the number of the outscattered atoms (recoils) of the sample components are measured at a fixed angle relative to the beam direction, as shown in Fig. 2.9. Owing to the element specific energy loss in material it is possible to calculate the depth dependent concentration distributions for all components of a sample from the measured energy spectra.

When a projectile of mass M_p, energy E_0, and atomic number Z_1 collides with a target atom of mass M_r and atomic number Z_r, it will transfer energy E_2 to the target atom at a recoil angle ϕ, which is given by:

$$E_2 = k_r E_0, \quad k_r = \frac{4M_p M_r \cos^2 \phi}{(M_p + M_r)^2} \tag{2.14}$$

where K_r is the kinematic factor for elastic recoil. If M_p, E_0, and ϕ are known, M_r may be determined and the target element is identified.

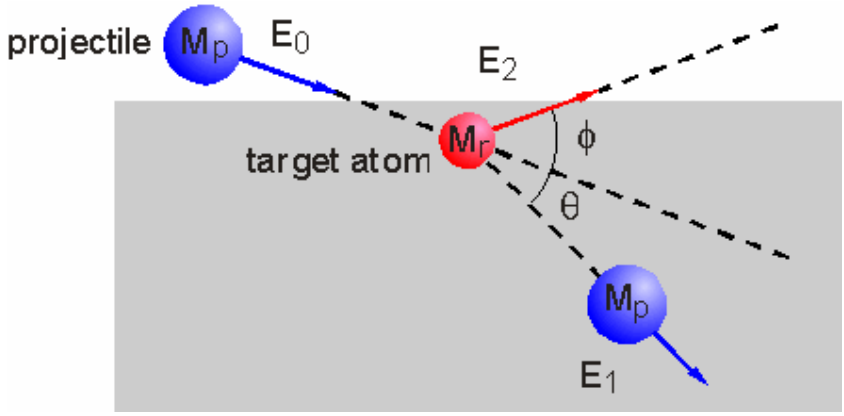

Figure 2.9 Collision kinematics between a projectile atom M_p and a target atom M_r in ERDA.

The total number of target atoms N_r is calulated from the measured number N_r' of the corresponding forward scattered atoms from the target with the formula:

$$N_r = \frac{N_r'}{\sigma_r \Delta\Omega N_0} \tag{2.15}$$

where σ_r is the differential recoil cross-section, $\Delta\Omega$ is the solid angle for the detector and N_0 the number of the incident projectile ions. σ_r is given by the formula:

$$\sigma_r = \left(\frac{e^2}{2E_0}\right)^2 \left(\frac{Z_p Z_r \left(M_p + M_r\right)}{M_r}\right)^2 \frac{1}{\cos^3 \phi} \tag{2.16}$$

For the cases of $M_p \gg M_r$ the differential recoil cross-section, also the detection sensitivity, is almost the same for all elements but enhanced by a factor of 4 for hydrogen.

The content of Li in the films was determined by ERDA at the Rossendorf 5 MV tandem accelerator. The measurements were performed with 30 MeV Cl^{7+} ions hitting the samples under an angle of 10° relative to the surface. The light recoiled atoms (Li and O) and the scattered chlorine ions were detected by a Bragg-Ionization-Chamber under a foreward direction of 30°.

The reader interested in more details of ERDA is referred to ref. [31, 34].

2.2.7 Optical transmittance

The optical transmittance of the sputtered films is measured by a Lambda 19 UV/VIS/NIR spectrometer by Perkin Elmer at different temperatures in the wavelength range of 250~3000 nm. Two light sources, a deuterium lamp (for UV) and a halogen lamp (for VIS and NIR) cover the working wavelength range of the spectrometer from 180 to 3300 nm. Radiation from the light source passes through an optical filter (depending on the wavelength being produced), the first monochromator, grating, and a second monochromator. The monochromatic light is split into sample and reference beam paths before reaching the sample compartment and then is reflected by the optics of the detector assembly onto the appropriate detectors. A photomultiplier is used in the UV/VIS and a PbS detector in the NIR range.

The experimental details are given in ref. [35].

2.2.8 Electrical resistivity

In this work, the van der Pauw technique was used to determine the electrical resistivity of the thin films. As originally derived by van der Pauw [36], one uses an arbitrarily shaped (but simply connected, i.e., no holes or nonconducting islands or inclusions), thin-plate

sample containing four very small contacts placed on the periphery (preferably in the corners) of the plate. A schematic of a rectangular van der Pauw configuration is shown in Fig. 2.10. A current must be forced through two adjacent contacts, and a voltage must be measured across the other two contacts. Let the current passing from contact *i* to contact *j* be denoted as I_{ij} and the voltage measured across contacts *k* (negative) and *l* (positive) be given by V_{kl}. Van der Pauw defines in his paper the resistance $R_{ij,kl}$ as:

$$R_{ij,kl} = \frac{V_{kl}}{I_{ij}} \tag{2.17}$$

Assuming that the contacts are numbered sequentially along the perimeter of the sample, van der Pauw discovered that the sheet resistance R_s of samples with arbitrary shape can be determined from $R_{12,34}$ and $R_{23,41}$. The actual sheet resistance R_s is obtained by solving:

$$e^{-\pi R_{12,34}/R_s} + e^{-\pi R_{23,41}/R_s} = 1 \tag{2.18}$$

The sheet resistivity ρ is defined as

$$\rho = R_s d \tag{2.19}$$

where *d* is the thickness of the sample.

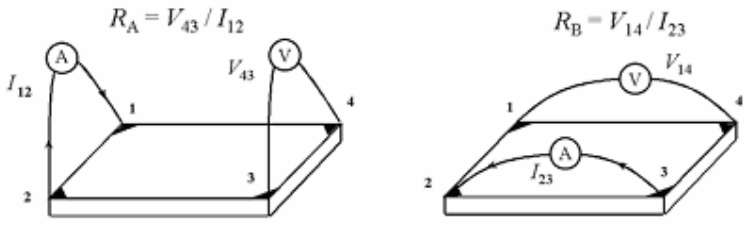

Figure 2.10 A schematic of a rectangular van der Pauw configuration for resistivity measurement.

The reader who is interested in more detail is referred to ref. [37].

Chapter 3 FeS material: a brief introduction

The crystallographic structure, the phase transition and the related magnetic and electrical properties of FeS are a source of interest for condensed matter physics. The early work focused on the structure and physical properties of FeS at ambient pressure [38-42]. Later its structure and physical properties were investigated at very high pressure with the improvement of the experimental setup [43-46]. In this chapter, a brief introduction of the structure and physical properties of FeS is provided.

3.1 Crystal structure

Figure 3.1 shows the phase diagram of FeS derived from X-ray studies of Kusaba *et al.* [43-45]. It can be seen that FeS exhibits a number of structural transitions under various *P-T* conditions. At ambient pressure, FeS has the NiAs-type structure ($a=a_f$ and $c=c_f$, where a_f and c_f are the lattice parameters of the fundamental NiAs cell) above 147 ^oC, belonging to the space group $P6_3/mmc$. The ideal hexagonal unit cell is illustrated in Fig. 3.2. It consists of an *hcp* lattice of S atoms with Fe atoms inserted in the octahedral sites, following the stacking sequence ABACABAC . . . , with Fe atoms on A sites and S atoms on B and C. Below 147 ^oC FeS is transformed to the troilite structure ($a = \sqrt{3}\, a_f$ and $c = 2\, c_f$)), which is a hexagonal superstructure derivative of the NiAs unit cell and belongs to the space group $P\bar{6}2c$. In this structure, Fe atoms are displaced from the NiAs positions and form triangular clusters in the hexagonal plane. This structural transition is called α-transition, and the transition temperature is called T_α. Since the length of the c-axis of the super-cell is twice that of the high-temperature phase with the NiAs structure, one call the high-temerature phase the 1*c* phase, and the low-temperature hexagonal superstructure phase the 2*c* phase. Increasing the pressure to around 3.5 GPa at room temperature results in a structural transformation to a hexagonal NiAs-type superstructure having unit-cell dimensions ($2a_f$, c_f). Further increase of pressure along the room temperature isotherm gives rise to another structrural transformation at 7 GPa to a new phase that may be indexed by a monoclinic unit cell in the space group $P2_1$ or $P2_1/m$, although details of the

new structure (e.g., atomic positions) are less well established. Table 3.1 shows the crystal structure, space group, and lattice constants of different FeS phases.

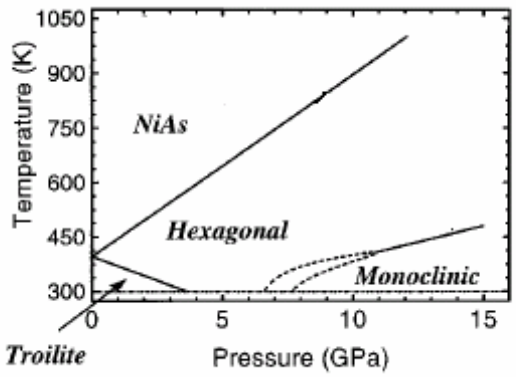

Figure 3.1 Structural phase diagram of FeS derived from X-ray studies of Kusaba et al. under various *P-T* conditions. The dashed phase boundaries (6.5-7.5 GPa) demarcate a range where two phases coexist [45].

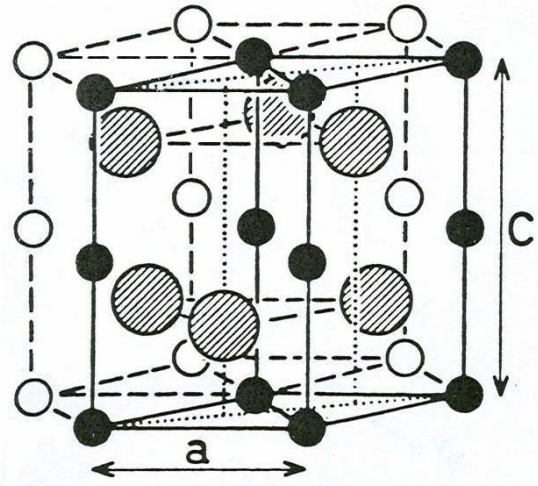

Figure 3.2 The NiAs type structure of FeS (small and large circles represent Fe and S atoms, respectively).

Table 3.1 Summary of crystal structure, space group, and lattice constants of different FeS phases.

phase	Space group (class)	Lattice constant (Å)
troilite phase	$P\bar{6}2c$ (190)	a=b=5.967, c= 11.761
NiAs type phase	$P6_3/mmc$ (194)	a=b=5.967, c= 23.522
hexagonal phase	?	a=b=6.549, c= 5.357
monoclinic phase	$P2_1$ (4) or $P2_1/m$ (11)	a=8.044, b=5.611, c=6.433, β=93.11°

Figure 3.1 shows the most accepted phase diagram of FeS. However, there are a few reports aclaimed that the diagram is not completely correct. For example, Fei *et al.*

proposed that besides these four phases, FeS has a MnP type phase with the orthorhombic cell ($a=c_f$, $b=a_f$ and $c=\sqrt{3}\,a_f$, space group: P*nma*) in the small region surrounded by the troilite, hexagonal and monoclinic phases [47]. Li and Franzen proposed that the phase transition from troilite structure to the NiAs-type structure occurs at the Néel temperature, not at T_α [48].

3.2 Electrical and magnetic properties

Since we are not interested in the behavior of FeS at very high pressure, here only the physical propreties of FeS at ambient pressure are introduced. Accompanying the structural transformation the physical properties of FeS vary significantly. At ambient pressure, FeS shows three phase transitions, one structural and the others magnetic.

(1) The MST at about T_α, 147 ^{o}C for bulk FeS, is associated with the structural transition from the NiAs-type structure at high temperatures to a closely related superstructure at low temperatures. On decreasing the temperature through T_α there is an abrupt decrease by two orders of magnitude in the electrical conductivity and FeS converts from a metal to a p-type semiconductor. T_α is sensitive to the composition of FeS.

(2) Neutron diffraction on nearly stoichiometric FeS powder shows that on heating the spins rotate from parallel to the c axis to perpendicular to the c axis at the temperature T_s (~180 ^{o}C). This transition is called Morin transition or α_s transition. T_s is very sensitive to the composition.

(3) The third transition occurs at the Néel temperature T_N (~327^{o}C). FeS is antiferromagnetic below T_N but paramagnetic above T_N. This transition is called β-transition. T_N is proved to be insensitive to the composition.

Chapter 4 Deposition, characterization and electrical properties of FeS thin films

As mentioned before, previous work on FeS focused on bulk FeS. Recently, a small attempt was made to produce FeS films. The first try was conducted by Shyu *et al.* via MOCVD [49], but the deposited films were not pure FeS thin films, containing some S-rich compounds, $Fe_{1-x}S$. Later on Lee *et al.* applied plasma sulfnitriding technique, in which a small amount of H_2S gas has been added to the gas mixture of N_2 and H_2 used in the glow discharge plasma nitriding method, to prepare FeS films used as solid lubrication coating [50, 51]. The present work concentrated on the deposition by reactive sputtering, characterization and electrical properties of FeS thin films, aiming to describe the MST of FeS thin films. The influence of sputter parameters, such as the H_2S flow, sputter power, substrate temperature and substrates, on the structure and electrical properties of FeS thin films was investigated systematically in order to optimize the sputter process. In addition, it has been found that the vacuum-annealing and air-aging have a significant influence on MST of FeS thin films. Finally, the influence of the film thickness and O doping on MST of FeS thin films will be discussed briefly.

4.1 Structure and morphology of FeS films

4.1.1 Deposition of FeS films

For the sputtering, Argon, as the working gas for providing the plasma, and H_2S, as the reactive gas, were let into the sputter chamber. The Ar flow was fixed at 2.5 standard cubic centimetres per minute (sccm) in all the deposition processes and the H_2S flow was variable. Figure 4.1 shows the partial pressure of Ar and H_2S with the change of flows in our sputter chamber. In the range applied for the deposition of FeS films, the partial pressure for both gases is linear with the gas flow. In this section, all the thin films were deposited on float glass at 500 ^{o}C and 200 W and the sputter time was 15 min, if not stated especially.

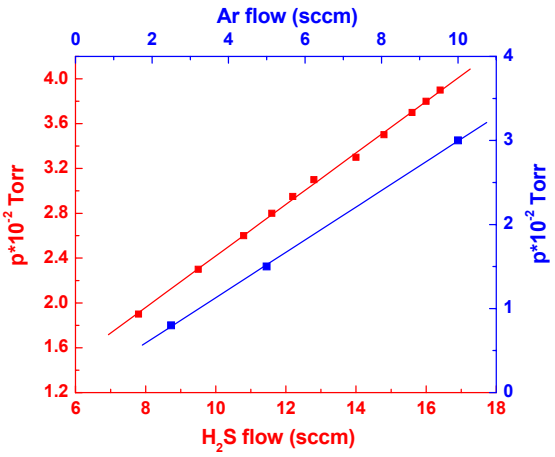

Figure 4.1 The partial pressure of Ar and H_2S as a function of gas flows in the sputter chamber.

The XRD spectra of the films deposited with different H_2S flows are presented in Fig. 4.2. From this figure one can see a suitable H_2S flow is necessary to prepare FeS thin films with a pure phase. When the H_2S flow is 9.0 sccm, a peak centered at 44.7^o corresponding to the Fe phase is visible besides other peaks from the FeS phase, indicating the H_2S flow is not high enough to react with the sputtered Fe atoms completely. If, however, the H_2S flow is increased to 10.0 sccm, a $Fe_{1-x}S$ phase appears. Only with the H_2S flow adjusted at 9.5 sccm, a film with a pure FeS phase could be prepared.

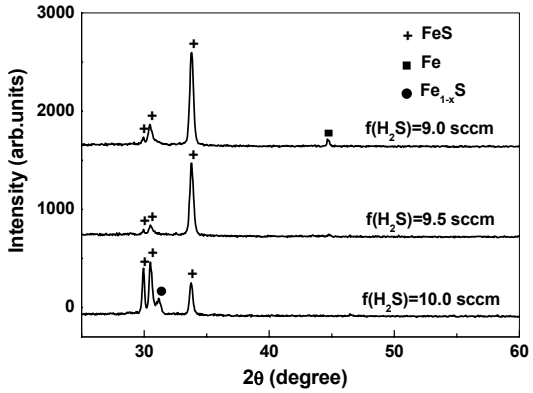

Figure 4.2 XRD patterns of the films deposited on float glass at 500 ^{o}C in the mixture of Ar and H_2S with different flows for 15 min.

Since only film thicknesses below 200 nm are measurable by XRR, a very thin FeS film was deposited to calculate the sputter rate at first. Figure 4.3 shows the measured and

simulated XRR spectra of an FeS film with the sputter time of 5.4 min. The simulated and measured curves are in good agreement with respect to the position of the total reflection angle and the maxima or minima of the oscillations. The simulated density of the FeS film is 4.52 g/cm^3, slightly lower than the bulk value (4.74 g/cm^3), which is understandable because a film is less dense than the bulk material. The sputtered FeS film has a quite smooth surface with a root mean square (RMS)-roughness of around 0.95 nm. The sputter rate at the sputter power of 200 W is around 20 nm/min. According to this sputter rate, the FeS films with the sputter time of 15 min have thicknesses of around 300 nm.

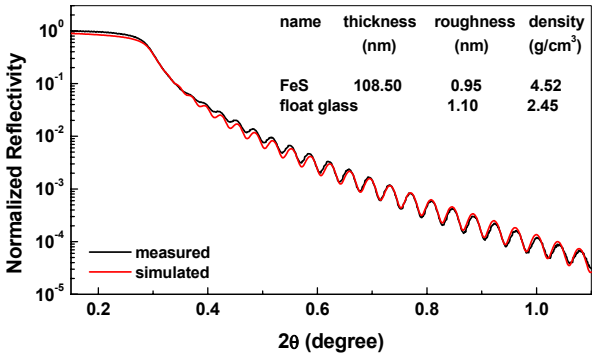

Figure 4.3 The measured and simulated XRR spectra of the FeS film sputtered on float glass for 5.4 min with simulation parameters of the layer thickness, roughness and density.

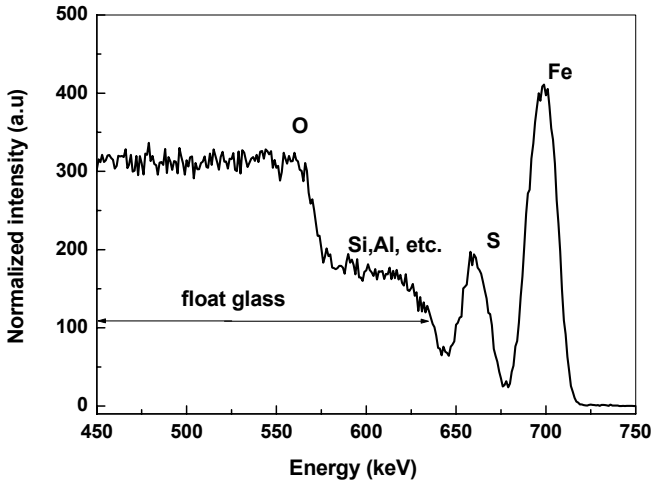

Figure 4.4 RBS spectrum of the FeS film deposited on float glass.

Figure 4.4 exhibits the RBS spectrum of the FeS film on float glass with the sputter time of 15 min. The signals of Fe and S from the FeS film, the signals of O, Si, Al, etc. from the

float glass are shown in the figure. The composition of the film calculated from this spectrum is $Fe_{0.94\pm0.10}S$. Taking the density of bulk FeS (4.74 g/cm^3), the thickness of this film is calculated to be about 270 nm, in agreement with the XRR measurement.

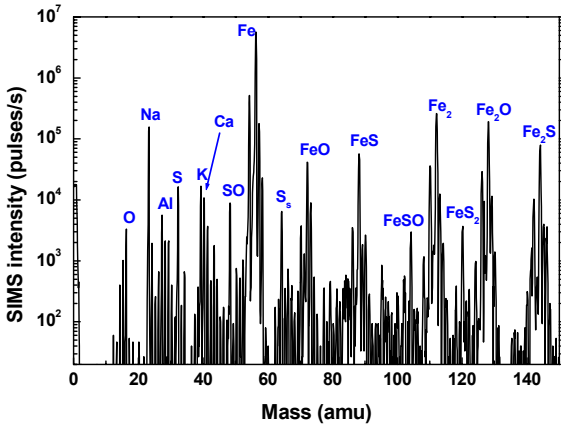

Figure 4.5 The typical SIMS mass spectrum of an FeS film on float glass.

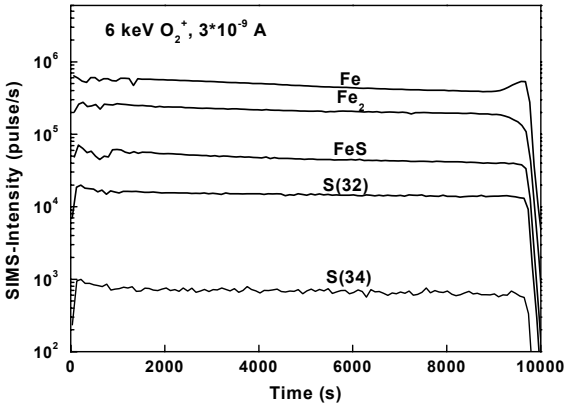

Figure 4.6 The SIMS depth profile of the FeS film on float glass.

The surface impurities as well as the depth homogeneity of FeS films are examined by SIMS measurements. Figure 4.5 is a positive ions mass spectrum for the surface of a typical FeS film on float glass, recorded with a 6 keV O_2^+ ion beam and 3×10^{-8} A current. Apart from the main elements Fe, S and their compounds, impurities such as O, Na, K, Ca and Al are detected at the surface. Obviously, Na, K, Ca and Al are diffused from the float glass to the film. O is partly contaminated from the air and partly diffused from the float glass. The depth profile of the the same sample is shown in Fig. 4.6. The constant

intensities of all elements related with Fe and S in the whole thickness of the film reveals a very good homogeneity and constant composition of the sputtered film.

4.1.2 Influence of the substrate temperature

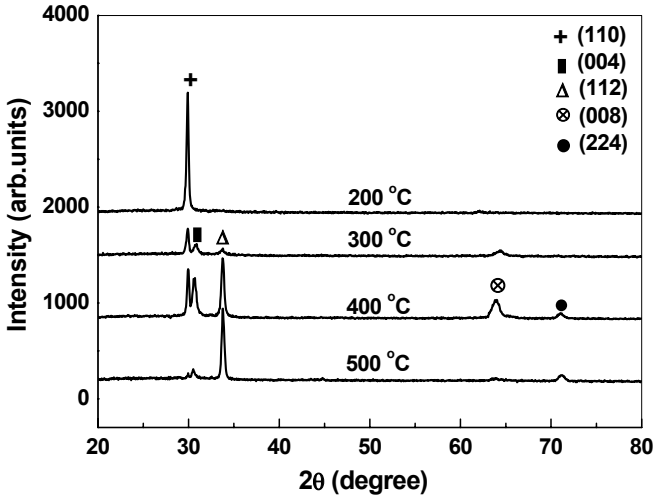

Figure 4.7 XRD patterns of FeS films prepared at 200 W and different substrate temperatures.

Figure 4.7 shows the XRD spectra of FeS films deposited at different temperatures. These films show a troilite structure. It can be seen that the crystal structure of the films depends on the substrate temperature. The film deposited at 500 ^{o}C shows (112) preferential orientation. If the substrate temperature decreases, the (112) reflection decreases in intensity, and finally disappears, while the growth on (110) planes predominates. The results agree with the mechanism, which states there is a relationship between the energy supplied to the adatoms during the growth and the different growth rates on different planes [52-54]. The lower this energy is, the more predominant the growth on (110) planes is, while the energy is increased, the c-axis gradually tilts away from the surface parallel to the surface normal, namely, the film has (001) orientation. In a sputter process, one way to supply this energy is to heat up the substrate. In our work, the low substrate temperature, for example 200 ^{o}C, results in the low energy supplied to the adatoms, which gives rise to the growth of (110) oriented films. When the substrate temperature is increased, the supplied energy is also increased. But it still not high enough to make the film grow on (001) faces. The c-axis just gradually tilts away from the surface parallel and the film

begins to grow on other faces such as (004) and (112) faces. But the growth rate on (112) faces is faster than that on (004) faces at higher temperature so that finally the (112) peak dominates.

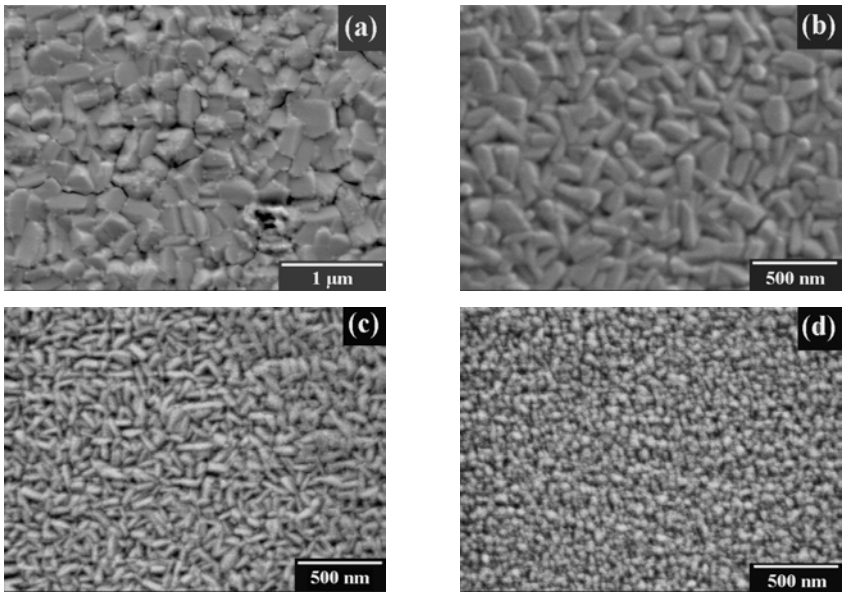

Figure 4.8 The surface morphology of FeS films deposited at 200 W and different substrate temperatures: (a) 500 ^{o}C; (b) 400 ^{o}C; (c) 300 ^{o}C; (d) 200 ^{o}C; respectively.

In addition to crystallinity, the surface morphology of the films grown at different temperatures is shown in Fig. 4.8. For the film obtained at 500 ^{o}C with the (112) orientation, stone-like particles with 300 nm in size were observed. If the substrate temperature is decreased to 400 ^{o}C, spindle-like particles appear. Further decrease of the substrate temperature gives rise to the decrease of the particle size and the increase of mean aspect ratio of the particles. The (110) oriented film deposited at 200 ^{o}C has spherical granular particles with an average size of 50 nm.

4.1.3 Influence of the sputter power

The influence of the sputter power on the structure and morphology of FeS films was also investigated. As usual, the higher the sputter power is, the more H_2S flow is needed to get the single phase FeS film. However, the sputter power does not have significant influence

on the structure and morphology of FeS films. Besides 200 W, the sputter power of 150 and 300 W were applied. Table 4.1 shows the optimal parameters for the deposition of FeS films with the same thickness of 300 nm at different sputter power. And Figure 4.9 shows the sputter rate of FeS thin films at different sputter power. It's interesting that the sputter rate is linear with the sputter power.

Table 4.1 The sputter parameters of the deposition of FeS thin films with the thickness of 300 nm.

Sputter power (W)	Ar flow (sccm)	H_2S flow (sccm)	Temperature (^oC)	Sputter time (min)
150	2.5	7.8~8.5	200~500	20
200	2.5	9.5~10.6	200~500	15
300	2.5	11.8~14.4	200~500	10

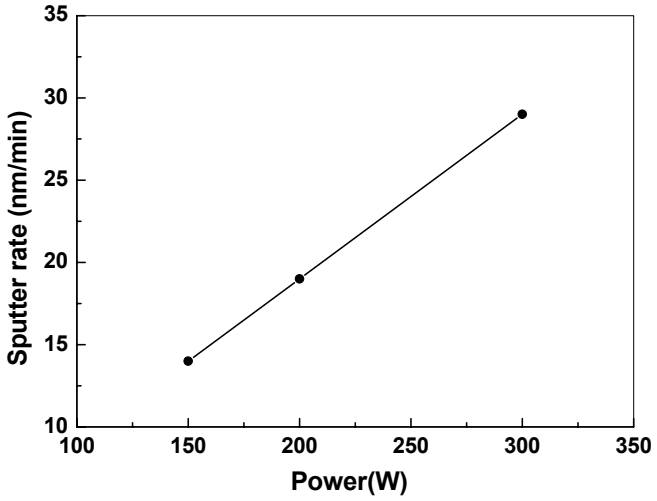

Figure 4.9 The sputter rate of FeS thin films at different sputter power.

Figure 4.10 presents the XRD patterns of 300nm-FeS thin films deposited on float glass at the sputter power of 150 and 300 W and different temperatures. These films also show the temperature dependent orientation, similar to the case of the sputter power of 200 W. At 200 ^oC, the films have the (110) orientation, whereas the (112) orientation is mostly important when the substrate temperature is 500 ^oC.

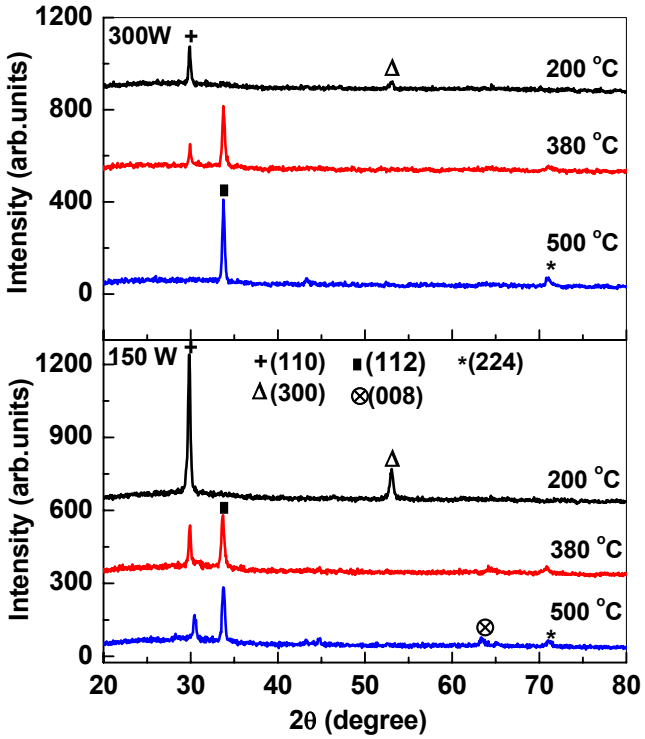

Figure 4.10 XRD patterns of FeS films prepared at different substrate temperatures and sputter power.

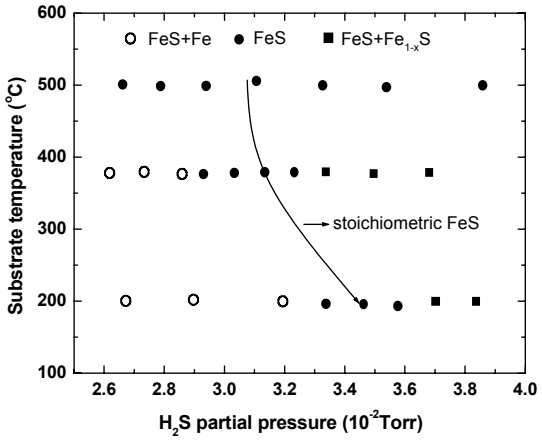

Figure 4. 11 The influence of the partial pressure of H_2S on the structure of FeS films deposited at 300 W and different temperatures.

Figure 4.11 shows the influence of the partial pressure of H_2S on the structure of FeS films deposited at 300 W and different temperatures. At 500 °C, all the films prepared in the

range of H_2S partial pressures from $2.5 \cdot 10^{-2}$ to $4.0 \cdot 10^{-2}$ Torr are single phase FeS films. With the decrease of the substrate temperature down to 380 ^oC, only the films deposited in the partial pressure of H_2S between $2.9 \cdot 10^{-2}$ and $3.3 \cdot 10^{-2}$ Torr are single phase FeS films. The films present a mixture of FeS and Fe phases below this range and a mixture of FeS and $Fe_{1-x}S$ phases above this range. The solid line describes the partial pressure of H_2S required for the stoichiometry at different temperatures. When the substrate temperature decreases, the optimal partial pressure of H_2S increases. It is understandable that the film formation in reactive sputtering is a reaction rate limited process. At higher deposition temperatures, the reaction happens faster so that less H_2S is required in order to get stoichiometric iron sulfide films.

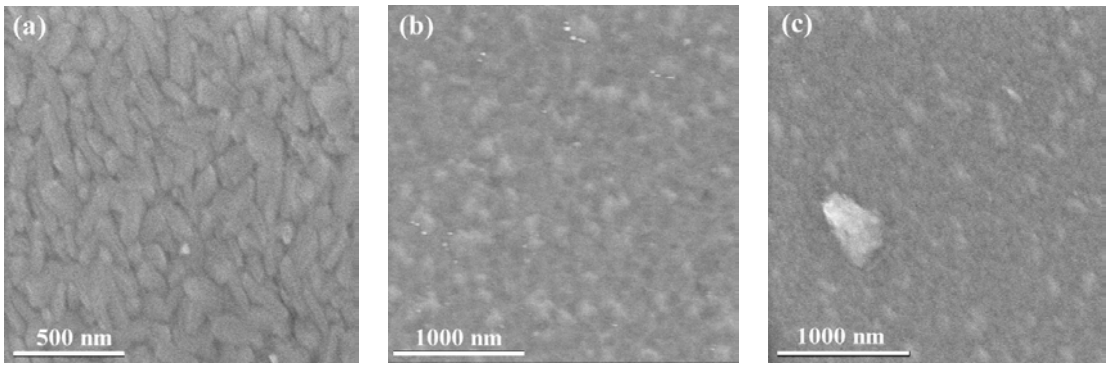

Figure 4.12 The surface morphology of FeS films deposited at 150 W and at different substrate temperatures: (a) 500 ^oC; (b) 380 ^oC; (c) 200 ^oC; respectively.

The surface morphology and cross sectional picture of FeS films deposited at different temperatures and at 150 and 300 W are shown in Figs. 4.12 and 4.13. At 150 W, the particle size of the films deposited at 200 and 380 ^oC are quite small and can't be distinguished. The film sputtered at 500 ^oC has the similar particles to the FeS film sputtered at 400 ^oC and 200 W (Fig. 4.8 (b)). At 300 W, the films deposited at 500 and 380 ^oC show the similar morphology and particle size of FeS films sputtered at the corresponding temperature with 200 W (Fig. 4.8 (a) and (b)). The film sputtered at 200 ^oC shows some spindle-like particles. From Figures 4.8, 4.12 and 4.13, it can be concluded that the morphology of FeS films is controlled by the energy of the sputtered atoms. If the sputtered atoms have low energy, FeS thin films containing spherical granular grains are formed. With the increase of the energy of the sputtered atoms by increasing substrate

temperature or sputter power some spindle-like particles are produced. Further increasing the energy, square stone-like particles can be observed. From the cross-sectional picture of the FeS film deposited at 500 ^{o}C and 300 W (Fig. 4.13 (d)), the film thickness of about 270 nm is calculated, in agreement with the XRR measurements.

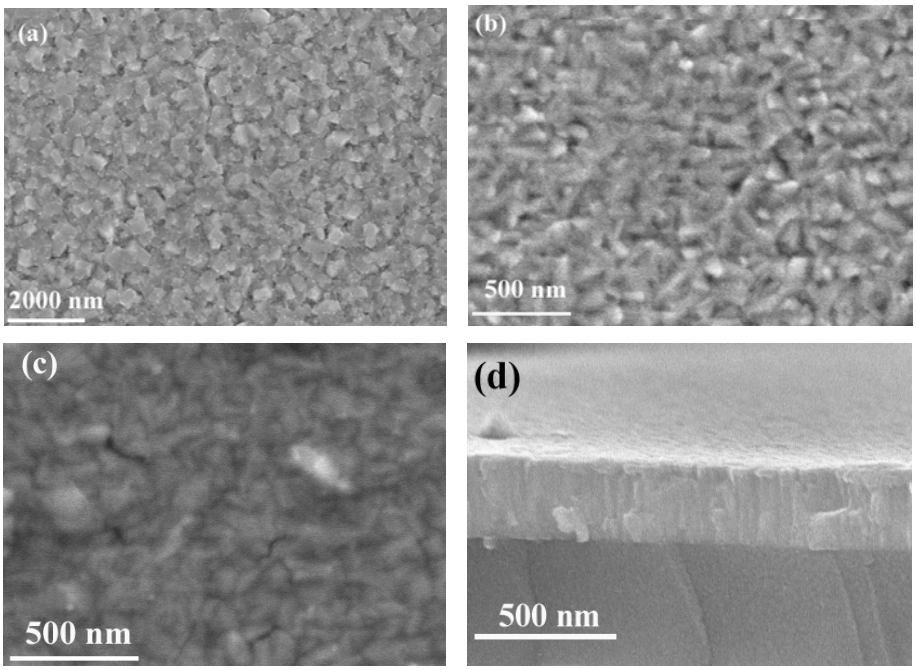

Figure 4.13 Surface morphology of FeS films deposited at 300 W and at different substrate temperatures: (a) 500 ^{o}C; (b) 380 ^{o}C; (c) 200 ^{o}C; (d) cross-sectional picture of FeS prepared at 500 ^{o}C; respectively.

4.1.4 Influence of the substrates

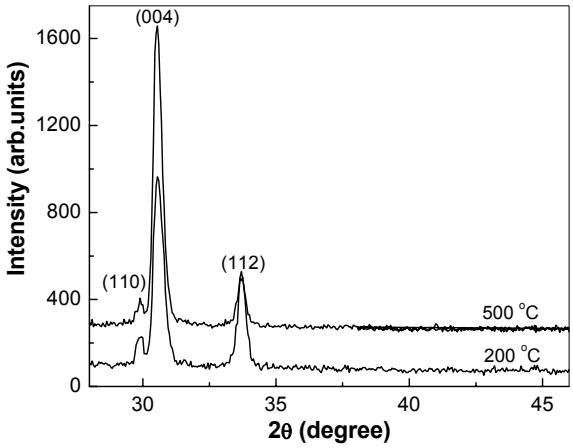

Figure 4.14 XRD patterns of FeS films deposited on quartz glass at 500 and 200 ^{o}C.

Besides float glass, quartz glass and single crystal sapphire were also used to deposit FeS films. All the FeS films on quartz glass and sapphire were sputtered at 300 W. Figure 4.14 shows the XRD patterns of FeS films deposited on quartz glass at 500 and 200 ^{o}C. FeS films on quartz glass show different XRD patterns with those on float glass. As one can see, two FeS films on quartz glass both show (110), (004) and (112) peaks. Among these peaks, (004) is the strongest peak, indicating both films have (004) preferential orientation.

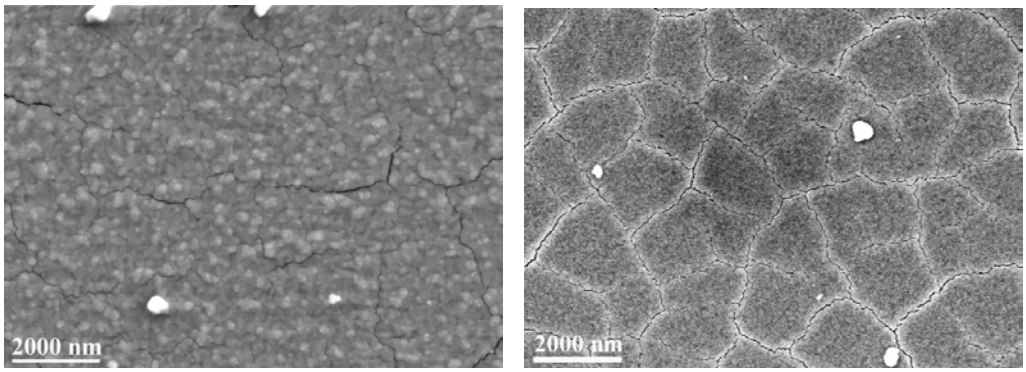

Figure 4.15 Surface morphology of FeS films deposited on quartz glass at 500 (left) and 200 ^{o}C (right).

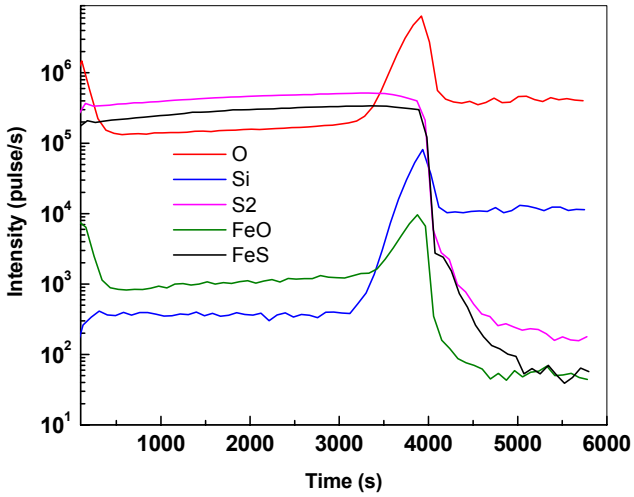

Figure 4.16 The SIMS depth profile of the FeS film prepared at 500 ^{o}C on quartz glass.

Figure 4.15 depicts the surface morphology of FeS films deposited on quartz glass at 500 and 200 ^{o}C. FeS films on quartz glass consist of spherical granular particles with smaller size than those on float glass.

The depth profile of FeS film prepared at 500 °C on quartz glass is shown in Fig. 4.16. Similar to that of FeS films on float glass, the intensities of the signals related to Fe and S are quite constant in the whole thickness, indicating the good homogeneity of FeS film on quartz glass. Si and O diffusing from the substrate are also presented.

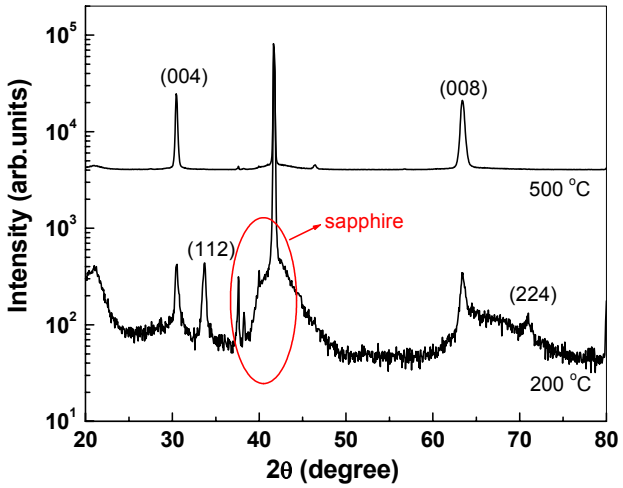

Figure 4.17 XRD patterns of FeS films prepared on single crystal sapphire with (0001) orientation at 200 and 500 °C.

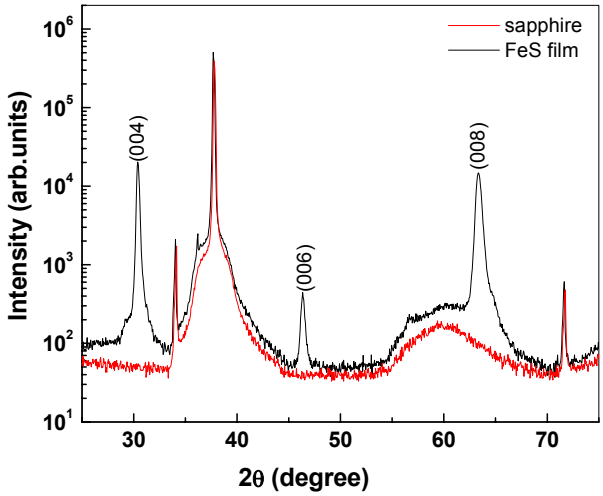

Figure 4.18 XRD patterns of FeS films prepared on crystal sapphire with (11 $\bar{2}$ 0) orientation at 500 °C.

The XRD patterns of FeS films on single crystal sapphire with (0001) orientation (c-Al_2O_3) are presented in Fig. 4.17. The FeS film prepared at 500 °C shows (004) and (008) peaks, following the orientation of the sapphire. At 200 °C, in addition to (004) and (008)

orientations, the FeS film also shows (112) and (224) orientations. In comparison, the single crystal sapphire with $(11\bar{2}0)$ orientation (a-Al_2O_3) was used to deposit the FeS film. The XRD patterns of the $(11\bar{2}0)$-oriented sapphire and FeS film prepared at 500 ^oC are shown in Fig. 4.18. Although the substrate is $(11\bar{2}0)$-oriented, the FeS film still shows the c-axis orientation.

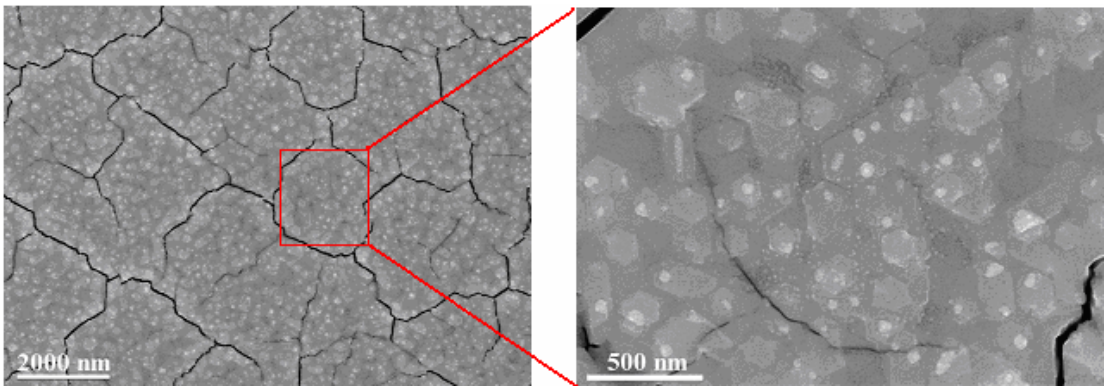

Figure 4.19 The surface morphology of FeS film deposited on (0001)-oriented sapphire at 500 ^oC.

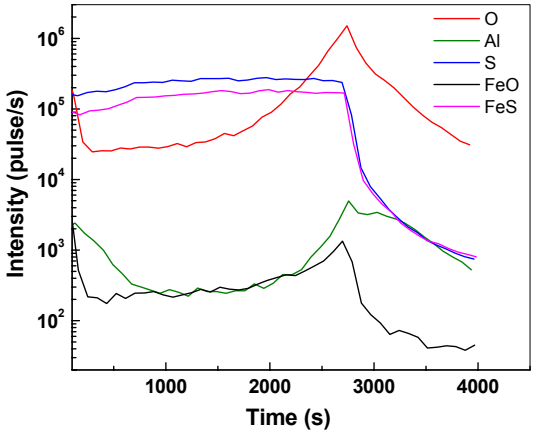

Figure 4.20 The SIMS depth profile of the FeS film deposited on (0001)-oriented sapphire at 500 ^oC.

The surface morphology of the FeS film prepared at 500 ^oC on sapphire with (0001) orientation is shown in Fig. 4.19. At low amplification, one can find the surface of the FeS film on sapphire consists of lots of dots with the size of 100~200 nm. In a closer look, some finer dots with a size of ~30 nm are found to be dispersed in those bigger dots.

Figure 4.20 shows the SIMS depth profile of the FeS film deposited on (0001)-oriented sapphire at 500 ^{o}C. Compared with Figs. 4.6 and 4.16, it can be seen that the homogeneity of the FeS film on sapphire is not as good as those of FeS films on float glass and quartz glass.

4.2 Electrical properties

MST of FeS films has been investigated extensively by different methods [38, 41, 55], such as the electrical resistivity measurements, Transmission Electron Microscopy, Differential Thermal Analysis, etc. Here the electrical resistvity of FeS films was measured by van der Pauw technique. To investigate the MST switching characteristics of FeS films quantitatively, we can analyse the derivative curve of the conductivity-temperature plot (i.e., dσ/dT), as shown in Fig. 4.21. Thus, the transition temperature during heating, T_α, or cooling T_α' can be defined as the maximum of the derivative curve [56], the loop width of the transition $\Delta T = T_\alpha - T_\alpha$' and the abruptness or sharpness of MST can be characterized by the full width at half maximum (FWHM) of the derivative curve.

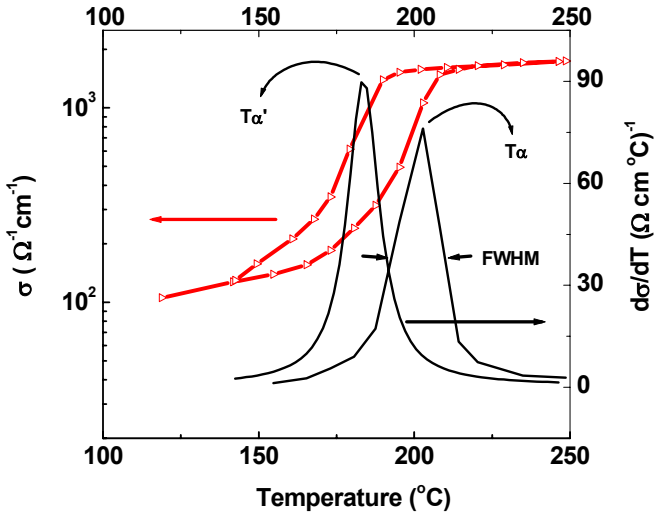

Figure 4.21 The analysis of the derivative conductivity curve.

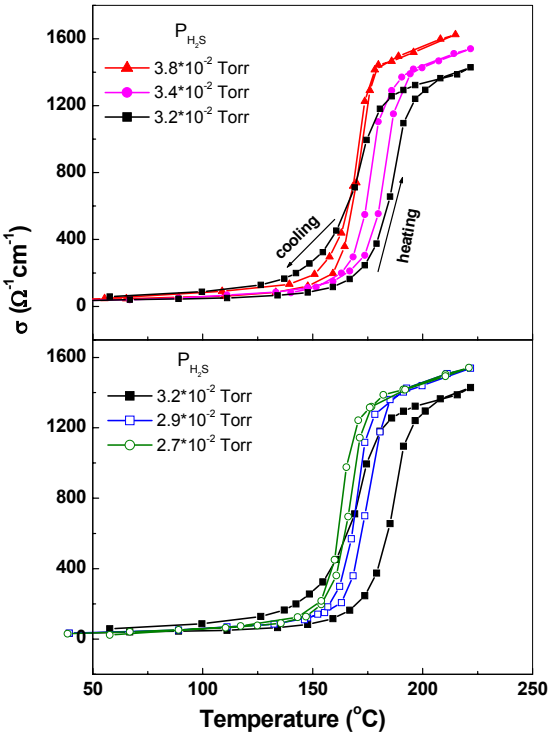

Figure 4.22 The electrical conductivity of FeS films prepared on float glass at 380 °C and 300 W with different H_2S partial pressure as a function of temperature.

Figure 4.22 shows the electrical conductivity of FeS films prepared on float glass at 380 °C and 300 W with different H_2S partial pressure. The conductivity at high temperatures is as high as ~ 10^3 $\Omega^{-1}cm^{-1}$, indicating FeS films are metallic although the conductivity still increases with the temperature; below T_α, the conductivity of FeS films is that of a semiconductor but the conductivity curves can not be fitted by the classical law ($\sigma = Ae^{-w/k_BT}$). The calculated T_α and ΔT of these FeS films are shown in Fig. 4.23. With the decrease of the H_2S partial pressure to $3.2 \cdot 10^{-2}$ Torr, T_α increases to a maximum of 188°C. Further decrease of the H_2S partial pressure results in the decrease of T_α. As shown in Fig. 4.11, $3.2 \cdot 10^{-2}$ Torr corresponds to the H_2S partial pressure necessary for stoichiometric film growth at this temperature. ΔT shows the similar behaviour. It first increases from 7 °C to a maximum of 16 °C and then shifts to lower values. Obviously, from Figs. 4.11 and 4.23, it can be seen that stoichiometric FeS films have the highest T_α and ΔT. Figure 4.23 shows T_α and ΔT of FeS films deposited at 200, 380 and 500 °C. T_α and ΔT of iron sulfide films deposited at different temperatures show the same trend with

the change of the H_2S partial pressure. They first increase, reaching a maximum at the stoichiometric composition, and then shift to lower values with a decrease of the H_2S partial pressure. By comparing T_α and ΔT of iron sulfide films prepared at different substrate temperatures, it can be found out that they decrease with decreasing substrate temperature.

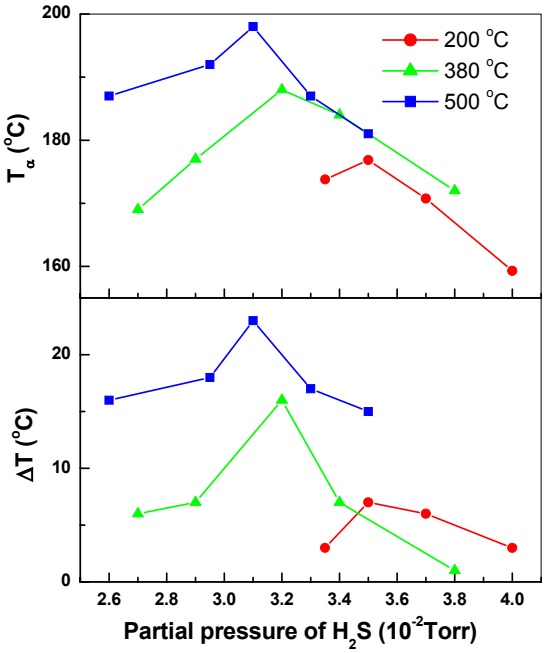

Figure 4.23 T_α and ΔT of FeS films deposited at 300 W and different temperatures and H_2S partial pressure.

The influence of stoichiometry on MST of bulk iron sulfide has been investigated extensively [57-59]. S-excess results in a decrease of T_α but to an increase of ΔT in bulk iron sulfide. In this work, the influence of S and Fe excess on MST of FeS films was investigated. Both lower T_α and ΔT. The decrease of T_α with Fe or S excess should be correlated with the introduction of defects, such as S or Fe vacancies, which decrease the transition energy. The decrease of ΔT of iron sulfide films with Fe or S excess is quite different from bulk iron sulfide, where it increases rapidly when the films are S-rich. This increase of ΔT in bulk iron sulfide is considered to be due to the disorder phenomena induced by vacancies when being S rich. However, in our case, both Fe and S excess results in the decrease of ΔT. Why ΔT of FeS films behaves differently compared to bulk material is a puzzle.

FeS films prepared at the sputter power of 200 and 150 W present almost the same electrical properties. Here just the electrical conductivity of stoichiometric FeS films prepared at 500 ^{o}C and different sputter power is compared, as shown in Fig. 4.24. All FeS films show almost the same conductivity. The only difference is the conductivity above T_a. The FeS film deposited at 300 W has the highest conductivity compared with the other two films. It should be induced by the good crystallinity of the film as a consequence of the high sputter power.

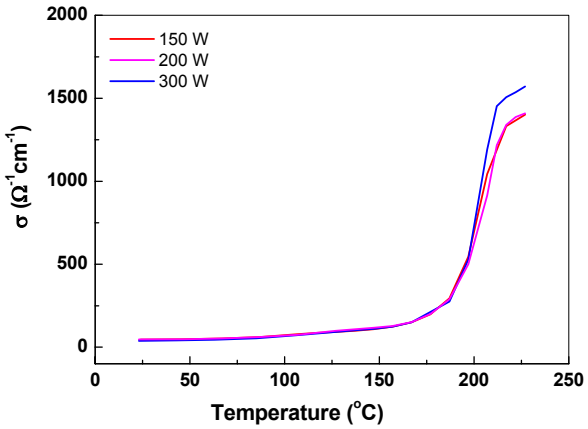

Figure 4.24 The electrical conductivity of stoichiometric FeS films prepared at 500 ^{o}C and at different sputter power.

From Fig. 4.23, we know that with the decline of the substrate temperature, T_α and ΔT of FeS films decrease. FeS films deposited at different substrate temperatures show different orientations, as shown in Figs 4.7 and 4.10. Both experimental findings indicate that the decrease of T_α and ΔT of FeS films with decreasing substrate temperature is probably caused by the different orientations of FeS films. In order to check it, different substrates, such as quartz glass and sapphire with different orientations, were used to deposit FeS films at different temperatures. The two FeS films on quartz glass show a strong (004) orientation. The temperature dependent conductivity and T_α and ΔT of FeS films on quartz glass are shown in Fig. 4.25. The stoichiometric FeS polycrystalline films on quartz glass deposited at 200 and 500 ^{o}C have different structure, as shown in Fig. 4.14, compared to the FeS films deposited on float glass. However, their T_α and ΔT decrease with the substrate temperature, similar to the behaviour of FeS films on float glass. T_α of the FeS

film deposited at 500 °C is about 200 °C. When the substrate temperature is 200 °C, T_α is decreased to 160 °C. With the decrease of the substrate temperature from 500 to 200 °C, ΔT is decreased from 20 to 5 °C.

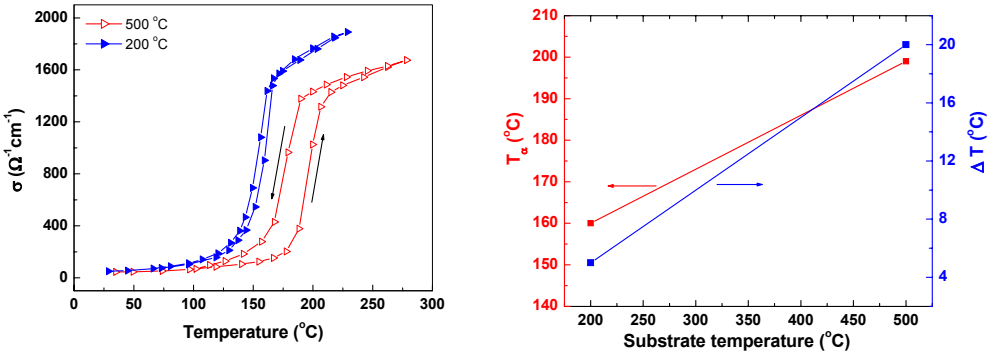

Figure 4.25 The conductivity and MST switching characteristic of FeS films deposited at 200 and 500 °C on quartz glass.

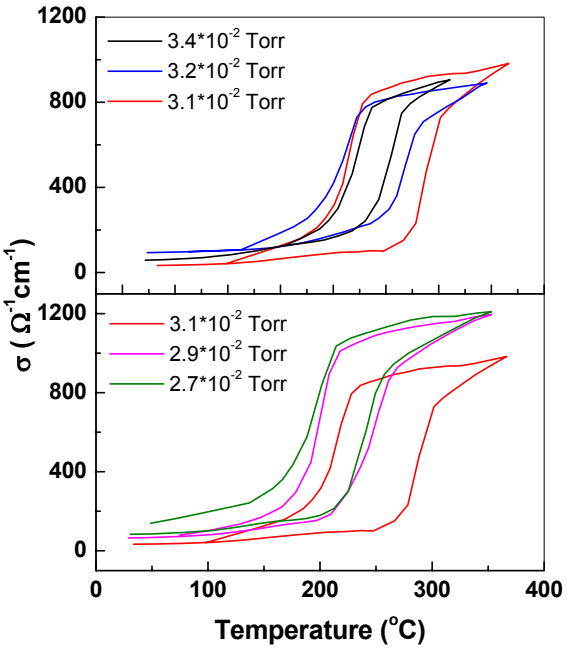

Figure 4.26 The temperature dependent conductivity of FeS films deposited on (0001)-oriented sapphire with the change of the H_2S partial pressure.

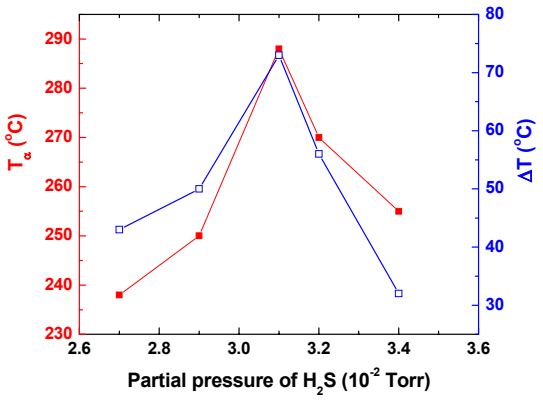

Figure 4.27 T_α and ΔT of the FeS films deposited on (0001)-oriented sapphire with the change of the H_2S partial pressure.

Figure 4.26 shows the electrical conductivity as a function of temperature of FeS films prepared on (0001)-oriented sapphire with different H_2S partial pressures at 500 °C and 300 W. The determined T_α and ΔT are shown in Fig. 4.27. Similar to the case of float glass, when decreasing partial pressure of H_2S to the optimal value for the stoichiometric FeS, T_α and ΔT increase. Further decrease of the partial pressure of H_2S results in the derease of the T_α and ΔT. But one significant difference to the FeS films on float glass is that the FeS films on sapphire have much higher T_α and ΔT.

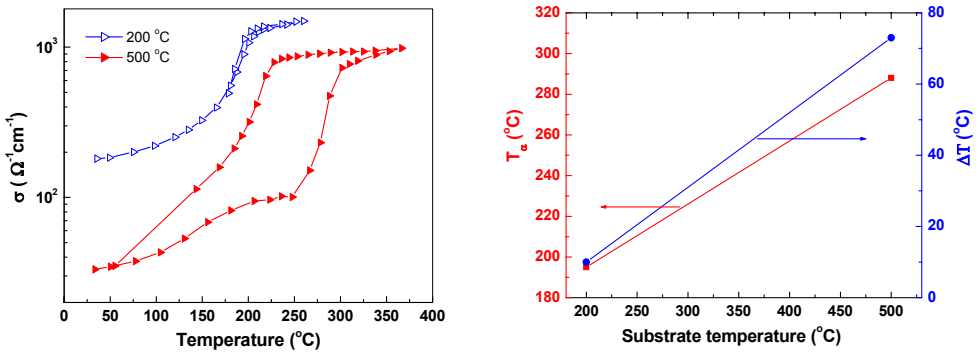

Figure 4.28 The electrical conductivity, T_α and ΔT of stoichiometric FeS films on (0001)-oriented sapphire prepared at 200 and 500 °C and at the sputter power of 300 W.

Figure 4.28 compares the electrical conductivity, T_α and ΔT of stoichiometric FeS films on (0001)-oriented sapphire prepared at 200 and 500 °C and at the sputter power of 300 W.

When the substrate temperature is decreased from 500 to 200 °C, T_α of FeS films decreases from 288 to 195 °C and ΔT decreases from 73 to 10 °C. In addition, the conductivity of FeS films in the whole measured temperature range shifts up.

We have so far investigated the structure and electrical behaviour of FeS films deposited on different substrates at different temperatures. FeS films on float glass show the (112) orientation at the substrate temperature of 500 °C and (110) orientation at 200 °C. In the case of quartz glass as the substrate, FeS films deposited at different temperatures show (004) orientation. The FeS films on (0001)-oriented sapphire at 500 °C show the c-axis orientation, following the orientation of the substrate. The films deposited at 200 °C show both c-axis and (112) orientations. However, T_α and ΔT of these FeS films on different substrates decrease with decreasing substrate temperature. It indicates that the variations of T_α and ΔT are not a consequence of the change of the orientation of FeS films.

In conclusion, we have prepared FeS thin films on different substrates by reactive sputtering. FeS films on float glass show substrate temperature dependent orientations. T_α and ΔT decrease with decreasing substrate temperature. In comparison to the cases of quartz glass and sapphire as substrate, it can be concluded that there is no relation between the orientation and metal-semiconductor transition temperature. The change of T_α and ΔT should be caused by other reasons.

4.3 Influence of the annealing on MST of FeS films

So far FeS films on different substrates have been prepared by reactive sputtering. The structure and electrical properties of FeS films were measured by XRD, SIMS, RBS, EDX and electrical resistivity measurements, etc. In this section the influence of the vacuum-annealing on MST of FeS films on float glass and sapphire is presented.

4.3.1 FeS films on float glass

FeS films prepared on float glass were annealed in vacuum at different temperatures. Figure 4.29 shows the electrical conductivity of FeS films on float glass before and after the vacuum-annealing at 360, 430, 500 and 600 °C for 1h. It can be seen that T_α of FeS films decreases after the as-prepared FeS film is annealed at 360 °C for 1h. With the

increase of the annealing temperature to 430 and 500 °C, T_α further decreases. But after the film is annealed at 600 °C for 1h, T_α increases. It can be realized that T_α first decreases from 202 to 185, 179 and 159 °C and then increases to 172 °C when the as-prepared FeS thin film is annealed for 1h from room temperature to 360, 430, 500 and 600 °C, respectively. Accompanying the variation of T_α, the electrical conductivity of FeS films at room temperature decreases from 80 to 10 $\Omega^{-1}cm^{-1}$ and then increases up to 80 $\Omega^{-1}cm^{-1}$ but the electrical conductivity at high temperatures keeping almost constant.

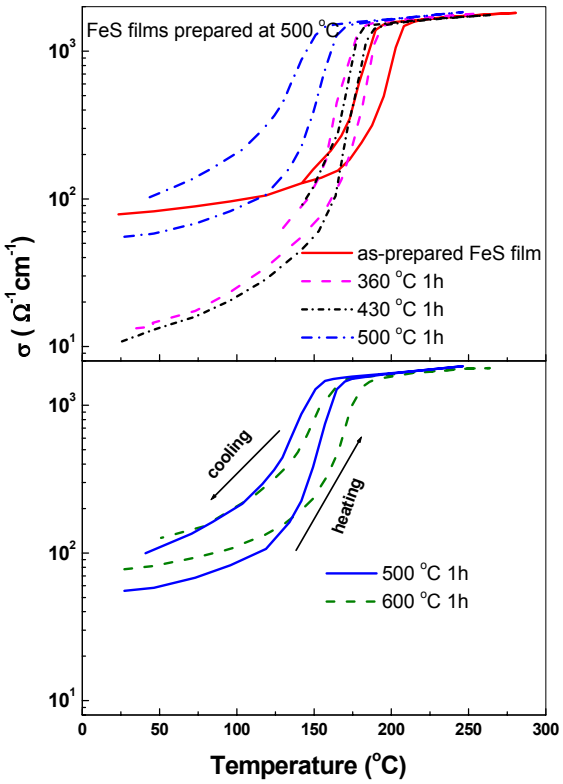

Figure 4.29 The temperature dependent conductivity of FeS films on float glass before and after the vacuum-annealing at 360, 430, 500 and 600 °C for 1h.

Figure 4.30 illustrates the change of ΔT, FWHM of the derivative of conductivity curve and position of the XRD peak (112) during the annealing process. With the increase of the annealing temperature from 360 to 430 °C, ΔT and FWHM decrease. But after the annealing at 500 and 600 °C for 1h, they increase again, similar to the behaviour of the conductivity at room temperature. As before, the as-prepared FeS thin film shows the (112) orientation. During the annealing process, this (112) peak shifts down from 33.776 to

33.763 ^{o} when the annealing temperature is increased to 430 ^{o}C. The (112) peak shifts up to 33.785 ^{o} with a further increase of the annealing temperature.

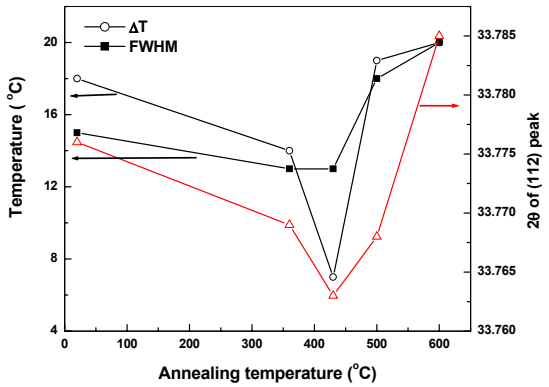

Figure 4.30 The variations of ΔT, FWHM of the derivative of conductivity curves and position of XRD peak (112) during the annealing process.

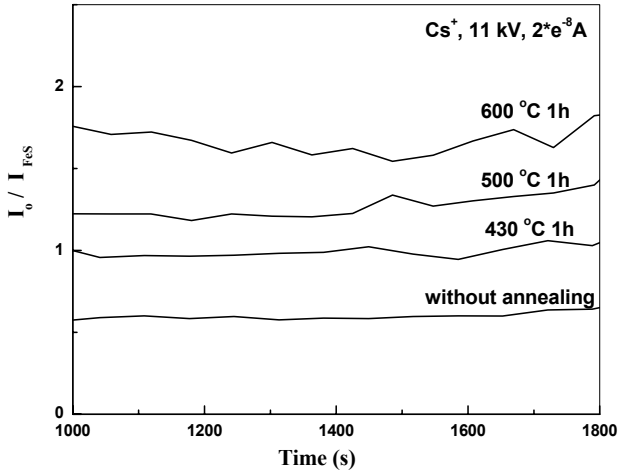

Figure 4.31 The change of the intensity ratio of O to FeS in the annealing process measured by SIMS.

It's well known that T_α of bulk FeS is about 147 ^{o}C and the electrical conductivity at room temperature and above T_α is in the range of 0-10 and 10^3 $\Omega^{-1}cm^{-1}$, respectively [38]. Figure 4.29 shows that with the increase of the annealing temperature, T_α and electrical conductivity at room temperature first decrease and then increase. It means that the behaviour of FeS films first changes close to bulk FeS and then deviates. During the

annealing process, some factors, such as the diffusion, crystallinity, grain size, and thermal stress may contribute to the variation of the MST switching characterics of FeS films.

Let us first look at the diffusion. As we know, the interdiffusion of elements between the film and substrate may change the composition of the film. As a consequence, the MST switching characterics may vary. Figure 4.31 shows the change of the intensity ratio of O to FeS due to the annealing process measured by SIMS. Other elements like Mg and Si show a similar behaviour. It indicates that with the increase of the annealing temperature, more and more impurities, like O, Mg and Si, diffuse into the film from the substrate, float glass. The results on the O doping in FeS films, as discussed later, show that T_α decreases and the conductivity at room temperature and FWHM increase with the increase of O concentration in the FeS film. It seems a reasonable contribution for the decrease of T_α with the increase of the annealing temperature from 360 to 500 ^{o}C. However, it can not account for the increase of T_α when the annealing temperature is increased to 600 ^{o}C.

Now we turn to the grain size and crystallinity. For the first order phase transition, with the increase of grain size, the transition temperature decreases [60]. Figure 4.32 shows the SEM pictures of an as-deposited FeS film and the FeS film after the annealing at 600 ^{o}C for 1h. It is found that after the annealing, there is little change of the morphology of the FeS film. The grain size, calculated by Scherrer formula, also has little variation (24~26 nm) for the FeS film before and after the vacuum-annealing. Such tiny change of the grain size should not affect MST of FeS film too much. Usually, material in the form of a polycrystalline film shows different characteristics than the bulk material and the better crystallinity the film has the closer behaviour to the bulk material. In our experiments, clearly the FeS polycrystalline film gets better crystallinity after it is annealed at higher temperature in vacuum. The as-deposited FeS film has a T_α of 202 ^{o}C, much higher than the bulk value. So with increasing annealing temperature, T_α should decrease down to the bulk value monotonously and MST of FeS film should sharpen so that the FWHM becomes smaller. However, Figs. 4.29 and 4.30 show T_α and FWHM do not behave as expected. As for the XRD peak (112), it should shift to lower values and get close to the bulk value of 33.69 ^{o}. From Fig. 4.30, it can be seen that this peak first shifts down and then up. Based on all these different findings, it is reasonable to believe that the variation of the MST switching characteristics of FeS films is not caused by the improvement of the film crystallinity.

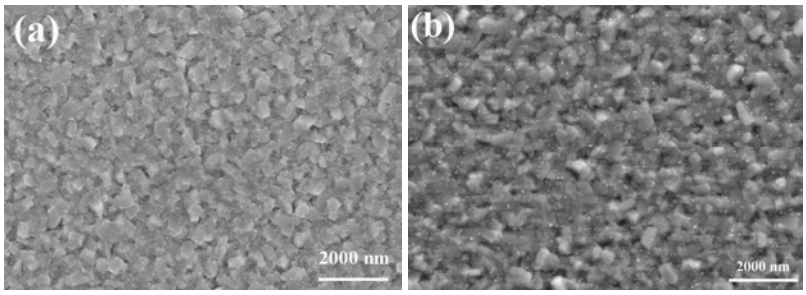

Figure 4.32 The SEM pictures of the FeS film before (a) and after the vacuum-annealing at 600 ^{o}C for 1h (b).

As we know, when a film is formed on a heated substrate by sputtering, a residual stress will develop in the film. For the FeS film prepared at 500 ^{o}C on float glass, obviously there is a certain value of residual stress in the film. This residual stress probably results in the shift of T_{α}. After the annealing of the FeS film at lower temperatures like 360 and 430 ^{o}C, the thermal stress is released so that the transition temperature decreased. When the annealing temperature is higher than 500 ^{o}C, the residual stress in the film will increase again, which results in the increase of T_{α}. According to this point, for an FeS film deposited at lower temperatures, for example 200 ^{o}C, one could expect, if this FeS film is annealed below or above 200 ^{o}C, T_{α} should decrease or increase due to the release or the increase of the residual stress, respectively.

This has been proven by our experiments. Figure 4.33 shows the electrical conductivity of FeS films prepared at 200 ^{o}C before and after the vacuum-annealing at 150, 360, 430 and 500 ^{o}C for 1h. The variations of T_{α} and ΔT for FeS films during the annealing process are shown in Fig. 4.34. When the annealing temperature is 150 ^{o}C, less than the deposition temperature 200 ^{o}C, T_{α} decreases from 177 to 162 ^{o}C. With the increase of the annealing temperature from 150 to 360, 430 and 500 ^{o}C, T_{α} increases from 162 to 168, 179, 182 ^{o}C, respectively. T_{α} of the FeS film after the vacuum-annealing at 500 ^{o}C decreases to 171 ^{o}C after the subsequent vacuum-annealing at 150 ^{o}C for 1h. According to the discussion above, the variation of T_{α} can be well understood. When the annealing temperature is lower than the deposition temperature, the residual stress inside the film is released. Consequently T_{α} decreases. At higher vacuum-annealing temperatures, for example, 360, 430 and 500 ^{o}C, the residual stress increases. This causes the increase of T_{α}. After the second annealing the FeS film at 150 ^{o}C for 1h, which was annealed at 500 ^{o}C before, the residual stress was released again so that T_{α} decreases again. ΔT should behave the similar

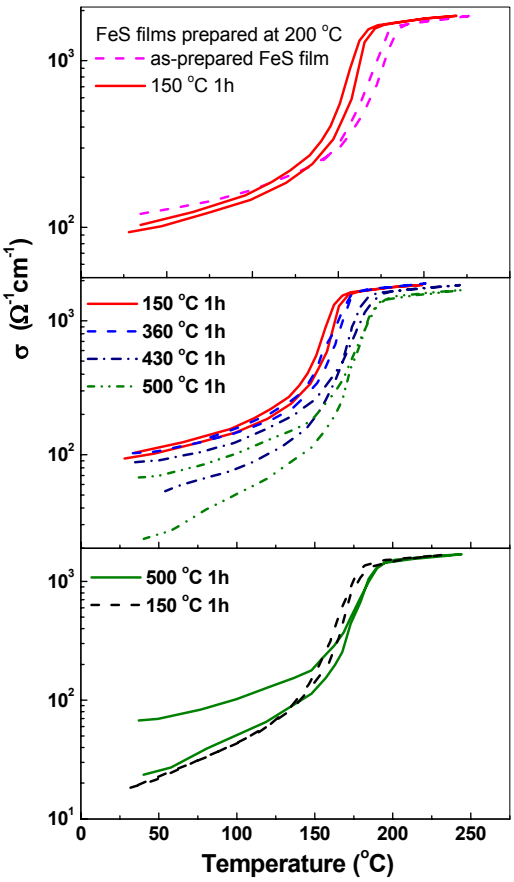

Figure 4.33 The electrical conductivity of FeS films prepared at 200 °C before and after the vacuum-annealing at 150, 360, 430 and 500 °C for 1h.

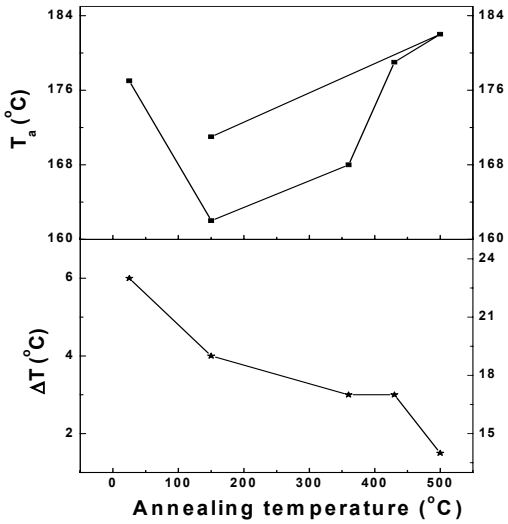

Figure 4.34 The variations of T_α and ΔT for FeS films before and after the vacuum-annealing at different temperatures.

behaviour, as discussed in the case of the annealing behaviour of the FeS film sputtered at 500 °C. When the annealing temperature is lower than the deposition temperature, ΔT should decrease, otherwise increase. But in this case, ΔT always decreases with the increase of the annealing temperature. It should be related to the improvement of the crystallinity of FeS film after the annealing at elevated temperatures. When the annealing temperature is 150 °C, both the improvement of the crystallinity and release of the residual stress make ΔT decrease. If the annealing temperature is higher than the deposition temperature, the release of the residual stress increases ΔT. On the other hand, the improvement of the crystallinity makes ΔT decrease. It should be noticed that the FeS film was prepared at 200 °C in this case. After the annealing at 360, 430 and 500 °C for 1h, the effect of the improvement of the crystallinity of FeS films probably dominates so that ΔT further decreases at elevated temperatures.

4.3.2 FeS films on sapphire with (0001) orientation

FeS films on sapphire with (0001) orientation show similar results. Here just FeS films deposited at 500 °C were discussed. Figure 4.35 shows the electrical conductivity and variations of T_α and ΔT of FeS films before and after the vacuum-annealing at 200, 360, 430 and 500 °C for 1h. With the increase of the annealing temperature, T_α and ΔT first decrease and then increase.

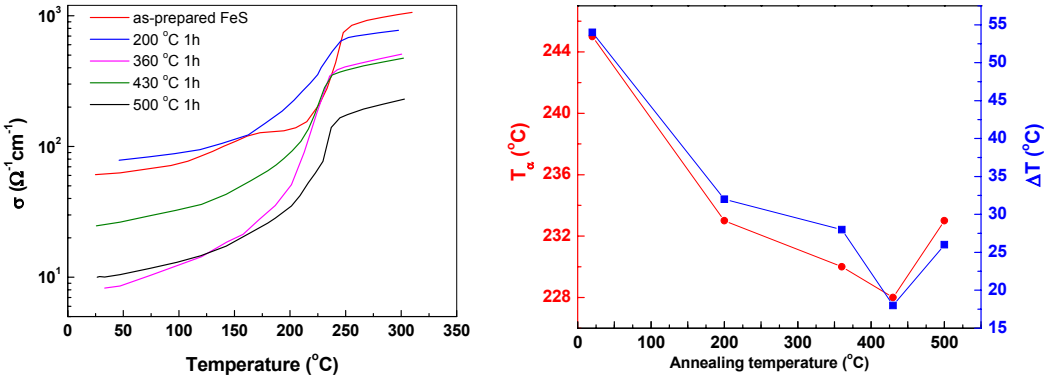

Figure 4.35 The electrical conductivity (left) and variations of T_α and ΔT (right) of FeS films prepared on sapphire with (0001) orientation at 500 °C before and after the vacuum-annealing at 200, 360, 430 and 500 °C for 1h.

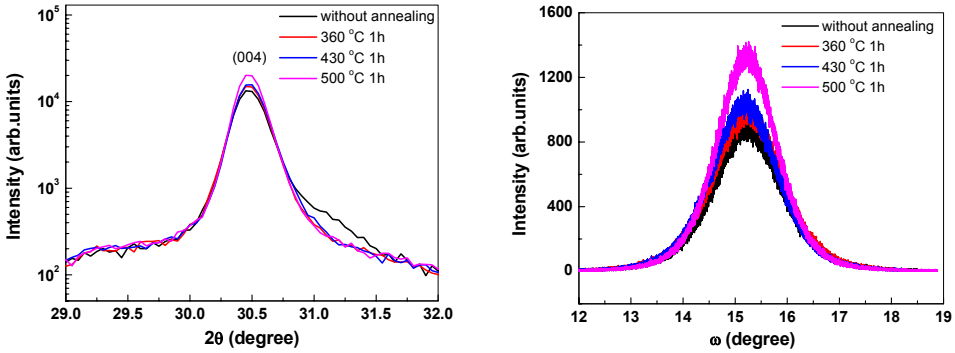

Figure 4.36 The variations of XRD peak (004) and rocking curve of the FeS film prepared on sapphire at 500 °C before and after the vacuum-annealing at 200, 360, 430 and 500 °C for 1h.

The XRD and rocking-curve measurements (Fig. 4.36) show that the XRD and rocking-curve peaks of the FeS film do not shift and just the intensity increases with the increase of the annealing temperature. At the same time, FWHM of the rocking curve decreases a little. It implies that the crystallinity of the FeS film is a little improved after the annealing, as expected.

The morphology of the FeS film before and after the vacuum-annealing at 500 °C for 1h is shown in Fig. 4.37. The only difference in these two films is that the fine particles in the as-prepared FeS film were no longer observable after the FeS film was annealed in vacuum at 500 °C.

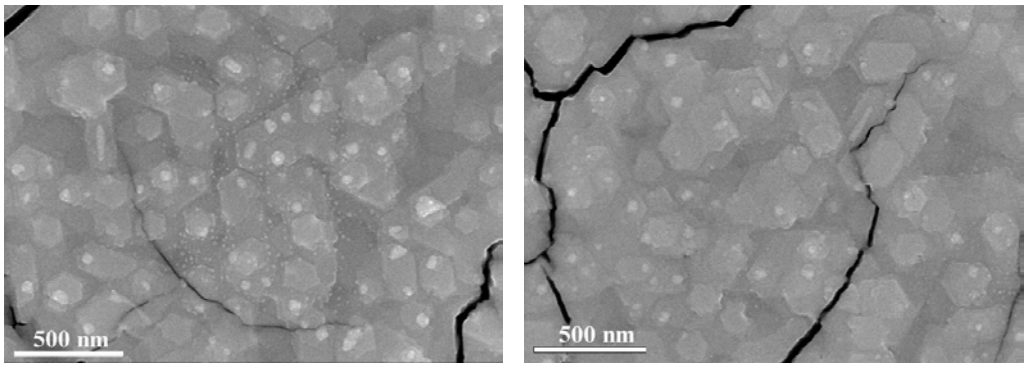

Figure 4.37 The SEM pictures of the FeS film on (0001)-oriented sapphire before (left) and after the vacuum-annealing at 500 °C for 1h (right).

Compared with FeS films on float glass, it can be found that the vacuum-annealing behavior of FeS films on sapphire is quite similar. The change of the residual stress inside the films is probably also the reason that FeS films on sapphire show different T_α and ΔT due to the vacuum-annealing process.

In summary, the thermal annealing effect of polycrystalline FeS thin films prepared by RF reactive sputtering was investigated. It has been found that the increase of the annealing temperature the metal-semiconductor transition temperature and the hysteresis width as well as the conductivity at room temperature first decrease and then increase. The residual stress is considered to contribute to the change of the metal-semiconductor transition of FeS films during the annealing process. The higher the residual stress is, the higher T_α and the conductivity at room temperature and the smaller ΔT the FeS films have. With the increase of the annealing temperature, the residual stress in FeS films is first released and then enhances, which gives rise to the abnormal change of MST of FeS films. With this assumption, the results in the section 4.2 that the transition temperature of FeS films decreases with the decreasing substrate temperature can be well explained. At high substrate temperatures, the deposited FeS films have high residual stress, which gives rise to high T_α.

4.4 Influence of the aging on MST of FeS films

Besides the vacuum-annealing, the aging also has a significant influence on MST of FeS films. It has been found out that T_α of FeS films varies with the aging time. In this section the aging behaviour of FeS films will be discussed.

Figure 4.38 shows the temperature dependent conductivity and T_α of the FeS film deposited at 200 ^{o}C before and after the air-aging for different time. With the increase of the aging time up to 105 d, T_α increases from 180 to 210 ^{o}C. And then the aged film is annealed in vacuum at 150 ^{o}C for 1h. It causes the decrease of T_α down to 195 ^{o}C. Further aging the film in air for 60 d, T_α decreases to 192 ^{o}C.

Figure 4.39 compares the conductivity and T_α of the FeS film before and after the aging in air and vacuum (10^{-5} Torr) for 45 d. In both cases, T_α increases but for the FeS film aged in air, it increases to a higher value.

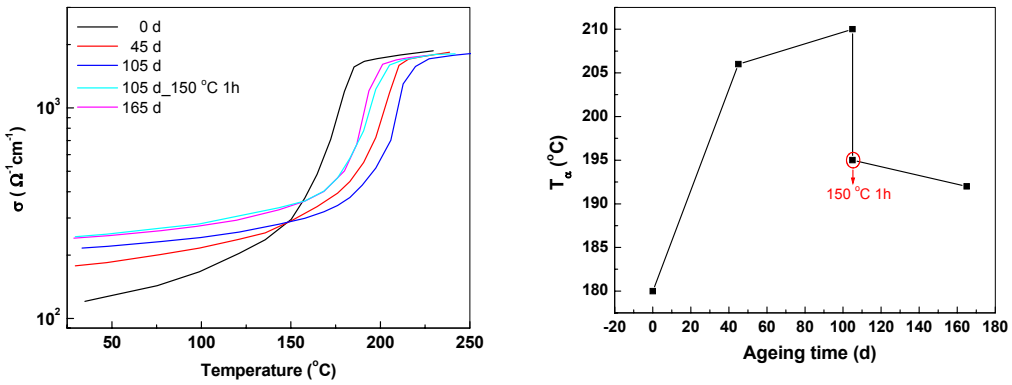

Figure 4.38 The temperature dependent conductivity and variation of T_α of the FeS film deposited at 200 °C before and after the aging in air for 45, 105 and 165 d.

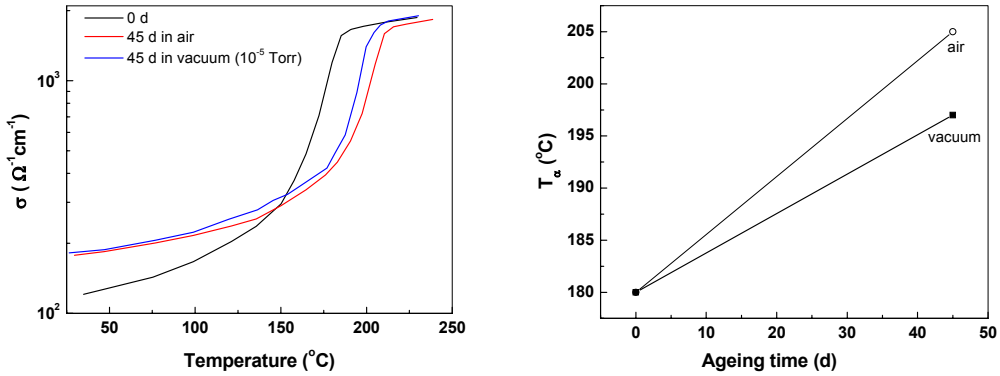

Figure 4.39 The temperature dependent conductivity and variation of T_α of the FeS film before and after the aging in air and vacuum (10^{-5} Torr) for 45 d.

For the FeS deposited at 500 °C, the aging behaviour is a little different. Figure 4.40 shows the temperature dependent conductivity and T_α of the FeS film before and after the air-aging for different time. After the film is aged in air for 45 d, T_α increases from 195 to 210 °C. Further aging in air results in the decrease of T_α from 210 to 192 °C. The next annealing of the sample in 150 °C decreases T_α down to 187 °C. Anyway, it can be concluded that with the increase of the aging time, T_α of FeS film first increases and then decreases. But the critical aging time is different for different samples. Figure 4.41 shows the change of the conductivity and T_α for another FeS film with the aging time. It can be seen that after the film is aged in air for 15 d, T_α increases. Further aging in air results in the decrease of T_α. These two FeS films only show a difference in composition.

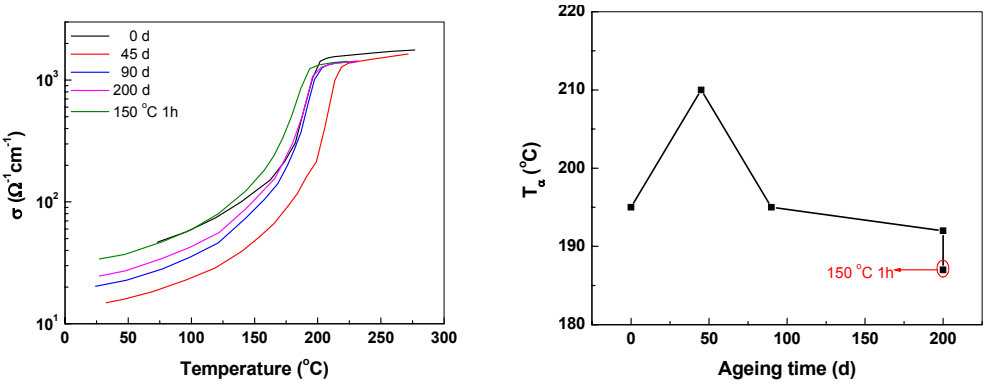

Figure 4.40 The temperature dependent conductivity and variation of T_α of the FeS film before and after the aging in air for 45, 90 and 200 d.

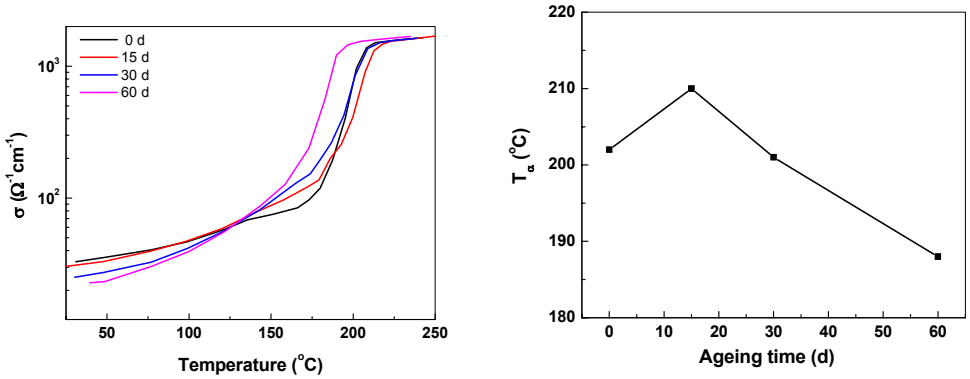

Figure 4.41 The temperature dependent conductivity and variation of T_α of the FeS film before and after the aging in air for 15, 30 and 60 d.

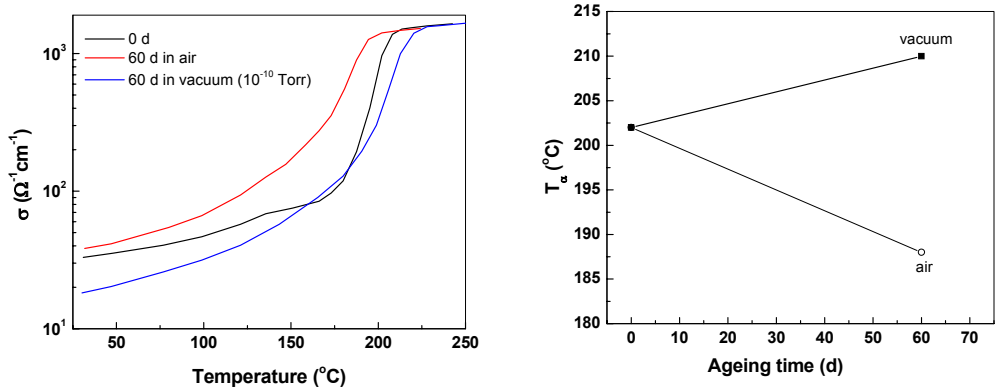

Figure 4.42 The temperature dependent conductivity and variation of T_α of the FeS film before and after the aging in air and vacuum for 60 d.

For the latter sample, the different aging behavior in air and vacuum (10^{-10} Torr) has also been compared, as shown in Figure 4.42. T_α of the FeS film decreases after aging in air for but increases after the aging in vacuum for 60 d.

From the results shown above, it can be concluded that with the increase of the aging time in air, T_α first increases and then decreases. There is a critical time. For iron sulfide films with different composition, the critical time is different. It is first supposed that the increase of T_α is probably caused by the gas adsorption. Taking the assumption that for FeS films after adsorbing some gas T_α increases, the aging behavior of FeS films can be well explained. With the increase of the aging time, more and more gas atoms are adsorbed onto the FeS films. It results in the increase of T_α. But there is a competitive process. In last section we have concluded that there is the residual stress inside the as-prepared FeS films. The residual stress will be also released in ambient although it is a very slow process. This process decreases T_α. So now we can imagine a picture: with the increase of the aging time in air, more and more gas atoms are adsorbed and the residual stress inside the FeS films is released. Due to the low release process, T_α increases. After a certain time the gas adsorption onto the FeS films is saturated, which keeps T_α stable. As a result, the release of the residual stress dominates, which decreases T_α. The critical time is different probably because FeS films with different composition have different adsorption saturation. If the FeS film is aged in vacuum, the situation is different. In high vacuum (10^{-5} Torr), there are much less atoms adsorbed onto FeS films. So after the same aging time, T_α increases less than that of FeS film aged in air. However, the aging behavior of FeS films in ultra high vacuum can't be understood by this assumption. In ultra high vacuum, only a few atoms adsorb onto FeS films. The release of the residual stress dominates so that T_α should have a lower value than that of the FeS film aged in air, which is different from our results. In addition, the SIMS depth profile of the FeS film before and after the aging in air and ultra high vacuum is compared. It has been found out that there is no obvious change of the intensities of O and N in FeS film after the air and ultra high vacuum-aging. That means that gas adsorption probably does not contribute the increase of T_α when FeS films are aged in air. The reason for the aging behavior of FeS films is still unclear.

4.5 Influence of the thickness of FeS films on MST

In the first section single phase FeS thin films were successfully prepared by the reactive sputtering. One of the advantages of thin films is that the film thickness can be easily varied in order to investigate the influence of the thickness and grain size on the structure and physical properties of the films. Here FeS films with different thicknesses were prepared and MST switching characterics were investigated. As before, FeS thin films were prepared at 500 ^{o}C on float glass at a sputter power of 300 W. The sputter time was varied from 3.5 to 14 min to get the FeS films with the thickness of 100 to 400 nm.

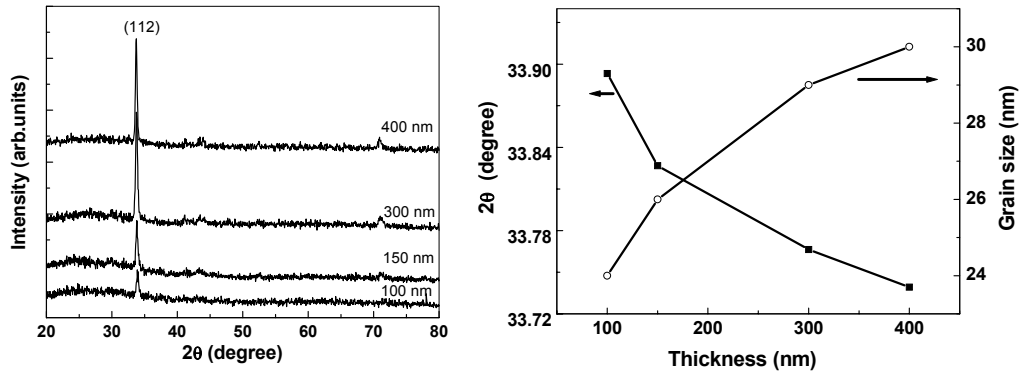

Figure 4.43 The XRD patterns and change of the (112) peak position and grain size of FeS films with thickness.

Figure 4.43 shows XRD patterns and variation of the (112) peak position and grain size of FeS films with thickness. All the films show the (112) orientation, in agreement with the previous results. With the increase of the thickness of FeS films, the intensity of the (112) peak increases, and its FWHM decreases, and its position shifts to lower values, close to the bulk value of 33.694. If we assume that only the finite size of the crystallites contributes to the broadening of the XRD peak, the average grain size of the films, *d*, could be estimated by the Scherrer formula. The grain size of FeS films increases from 24 to 30 nm with increasing film thickness from 100 to 400 nm. The morphology of FeS films is shown in Fig. 4.44. All the films are continuous and characterized by the compact packing of particles, whose size increases with the increase of the film thickness.

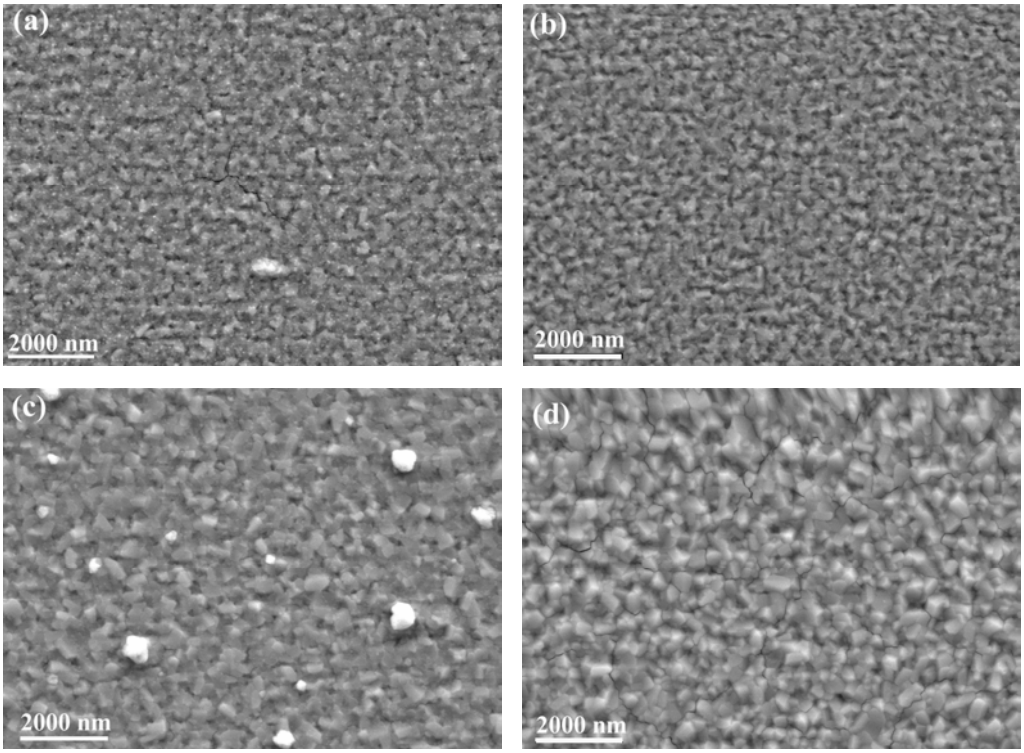

Figure 4.44 The morphology of FeS films with the thickness of 100 (a), 150 (b), 300 (c) and 400 nm (d).

Figure 4.45 shows the temperature dependent electrical conductivity and MST switching characteristics of FeS films with different thicknesses. When the film thickness is increased from 100 to 400 nm, T_α increases from 157 to 202 ^{o}C, ΔT decreases from 57 to 15 ^{o}C, the FWHM of the conductivity curves during heating decreases from 37 to 15 ^{o}C, and the electrical conductivity below T_α decreases dramatically.

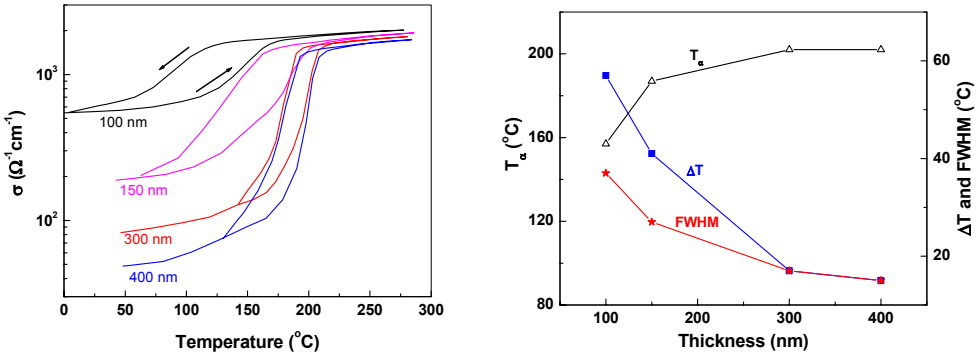

Figure 4.45 The temperature dependent electrical conductivity and variations of T_α, ΔT and FWHM of the conductivity curves during heating with the thickness of FeS films.

From the above results, it can be concluded that the film thickness has a great influence on MST of FeS films. First of all, when the film thickness is increased, the crystallinity of FeS films improved and then the density of the defects in the FeS films decreased. As reported by Keller-Besrest and Collin [58, 59], T_α decreases by the introduction of some defects into FeS. So in our case T_α increases with increasing film thickness. In addition, the change of the films thickness causes the variation of the grain size. FeS films with small grains contain a large density of grain boundaries, which tend to increase the conductivity of the semiconducting state (through the presence of defects levels in the gap). It leads thereby to a less intense and less abrupt transition.

According to the above discussion, one could expect that if the grain size of FeS films increases, T_α of the films will increase and the electrical conductivity below T_α will decrease. This has been approved by the annealing behavior of the FeS film of 100 nm.

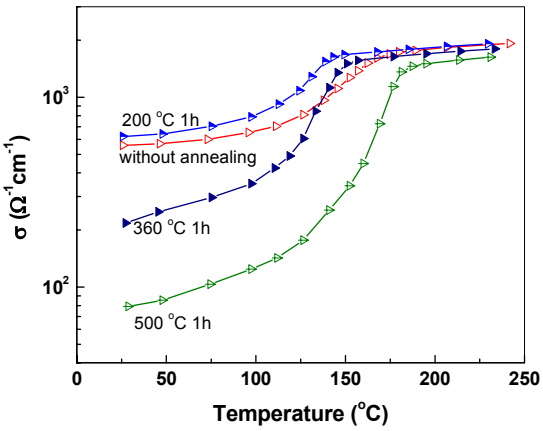

Figure 4.46 The temperature dependent electrical conductivity of the FeS film of 100 nm before and after the vacuum-annealing at 200, 360 and 500 °C for 1h.

Figure 4.46 shows the electrical conductivity of the FeS film of 100 nm before and after the vacuum-annealing at different temperatures. After the as-prepared FeS film was annealed at 200 °C for 1h, T_α decreases, which should be caused by the release of the residual stress in the films, as we discussed in section 4.3. After further increase of the annealing temperature, T_α increases and the conductivity below T_α decreases quickly. Figure 4.47 shows the morphology of the FeS film of 100 nm before and after the vacuum-annealing at 200, 360 and 500 °C for 1h. The as-prepared FeS film consists of some big particles, agglomerated from small grains, although some small particles are immersed

inside. When the film was annealed, these big particles decompose into some small grains with the size of 35~70 nm, obviously seen from Fig. 4.47 (c). With the further increase of the annealing temperature, the size of these small grains increases.

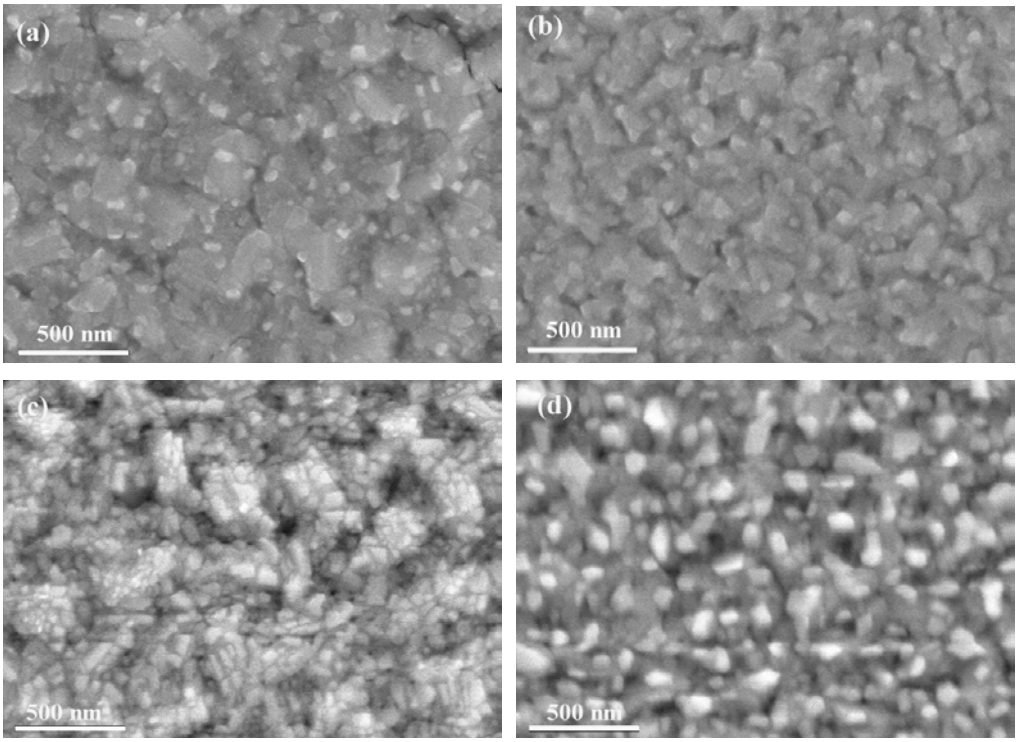

Figure 4.47 The morphology of the FeS film of 100 nm before (a) and after the vacuum-annealing at 360 (b), 500 (c) and 600 ^{o}C (d) for 1h.

In summary, FeS polycrystalline thin films with different thicknesses were prepared on float glass at 500 ^{o}C by RF reactive sputtering to investigate the influence of the film thickness on MST of a FeS film. The correlation between the film thickness (grain size) and the MST switching characteristics of FeS films was established. With the decrease of the grain size, the density of grain boundaries increases, causing the increase of the conductivity of the semiconducting phase. When the thickness of FeS films is increased, they contain smaller density of defects, which increases T_{α} of FeS films.

4.6 O doping in FeS films

As mentioned before, the mechanism of MST of FeS is still unclear. Different ways were used to try to clarify it. One way is doping. Some work has been done on alloying FeS with various MS sulfides, such as $Fe_{1-x}M_xS$ (M: Mn, Cr, Co, etc.) [61, 62]. A decrease of T_α was observed with increasing M concentration in the compound. The structure and physical properties of $Fe_{1-x}M_xS$ were discussed within the framework of conductivity by polarons. The α-transition occurs when the polaron concentration, thermally created or introduced by impurities, reaches the critical value. The driving mechanism for the α-transition is a reduction of the polaron dissociation energy by a temperature increase or by alloying. All these work focused on cation replacement. Anion replacement has never been done. Here some preliminary results of the O doping in FeS thin films are presented.

The O doping was achieved by introducing Ar (2.5 sccm), H_2S (12.8 sccm) and O_2 (0.10 ~ 0.34 sccm) into the vacuum chamber. The sputter power and temperature were 300 W and 500 ^oC, respectively. As usual, the thickness of all films was about 300 nm.

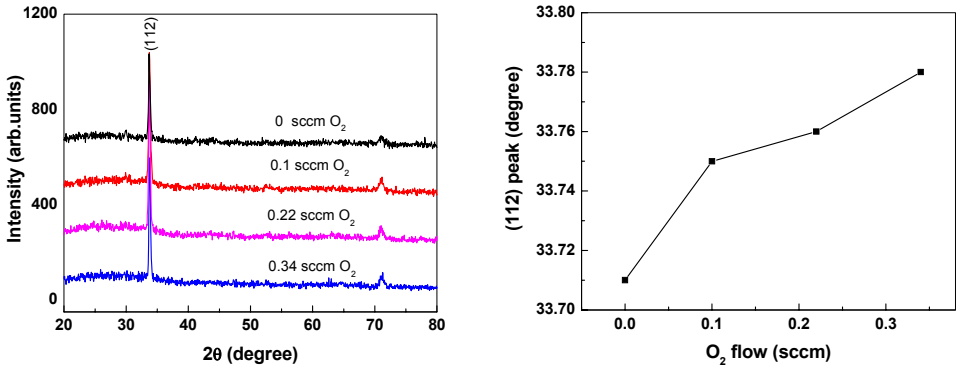

Figure 4.48 The XRD patterns and (112) peak position of FeS thin films with and without the O doping.

Figure 4.48 shows the XRD patterns and (112) peak position of FeS thin films with and without the O doping. The O doped FeS thin films still show the (112) preferential orientaion, same with pure FeS thin films. But the (112) peak position shifts to higher values with increasing O_2 flow. This means that the lattice constants decrease. It occurred also in $Fe_{1-x}M_xS$.

The incorporation of O in FeS films is qualitatively confirmed by SIMS measurement, as presented in Fig. 4.49. The intensity ratio of O to FeS increases with increasing O_2 flow.

The signal of O in a pure FeS film is caused by the O diffusion from the substrate during sputtering process.

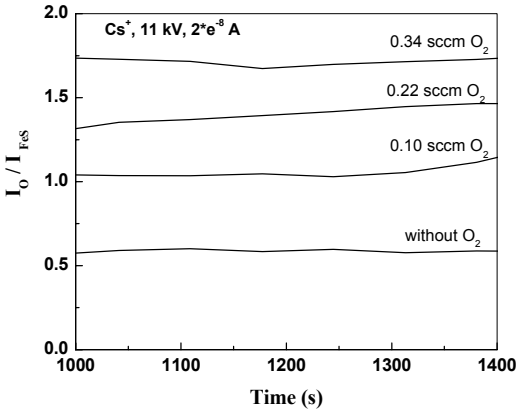

Figure 4.49 The intensity ratio of O to FeS in FeS films with and without O doping.

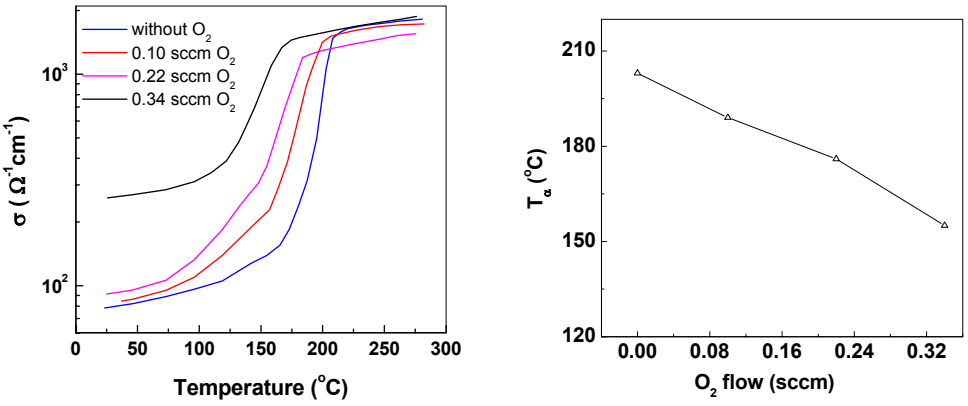

Figure 4.50 The temperature dependent electrical conductivity and the transition temperature T_α of FeS thin films with and without O doping.

Figure 4.50 shows the temperature dependent electrical conductivity and variation of T_α of FeS thin films with and without the O doping. T_α decreases when the O content in FeS films is increased. This behaviour is quite similar to the cation replacement in $Fe_{1-x}M_xS$.

In conclusion, O was doped into FeS thin films by introducing Ar, H_2S and O_2 into the sputter chamber. With the increase of O content in FeS films, the lattice constants and T_α decrease.

4.7 Summary

Iron sulfide thin films over a range of composition were prepared by reactive sputtering. The influence of the substrate, sputter power, substrate temperature and stoichiometry on the structure and MST of iron sulfide films was investigated. Iron sulfide films deposited at different temperatures show temperature dependent structure and MST. FeS films on float glass show (110) and (112) orientations when the substrate temperature is 200 and 500 ^{o}C, respectively. The transition temperature and width of the hysteresis loop determined from the temperature dependent conductivity curves of iron sulfide films decrease with the substrate temperature, which should be caused by the decrease of the residual stress inside the films. The sputter power has little influence on the structure and MST of FeS films. Fe and S excess in FeS films both result in the decrease of the transition temperature and width of the hysteresis loop. The vacuum-annealing affects the MST of FeS films significantly. When FeS films were annealed below the deposition temperature, the transition temperature decreases, otherwise increases. The residual stress plays an important role during the annealing process. The higher the residual stress inside the FeS films is, the higher the transition temperature of FeS films is. With the increase of the annealing temperature, the residual stress in FeS films is first released and then enhanced, which gives rise first to the decrease and then increase of the transition temperature of FeS films. This explains why the transition temperature of FeS films increases with increasing substrate temperature. At high substrate temperatures, the residual stress is higher. Consequently, the transition temperature of FeS films increases. In addition, the MST of FeS films was influenced by the ambient aging. With the increase of the aging time, the transition temperature first increases and then decreases. The subsequent decrease of the transition temperature is caused by the release of the residual stress inside the FeS films. Why the transition temperature first increases after a certain time of ambient aging is unclear, but it is probably not due to the gas adsorption onto FeS films.

Additionally, FeS films with different thicknesses were prepared. The correlation between the film thickness (grain size) and the MST switching characteristics of FeS films was established. With the decrease of the grain size, the density of grain boundaries increases, causing the increase of the conductivity of the semiconducting phase. Thicker FeS films contain smaller density of defects, which increases T_{α} of FeS films.

Finally, some preliminary results of the O doping into FeS films are presented. O was doped into FeS thin films by introducing Ar, H_2S and O_2 into the sputter chamber during the deposition process. With the increase of O content in FeS films, the lattice constants and T_α decrease.

Chapter 5 VO_2 material: a brief introduction

VO_2 is one of the most potential materials for the application as smart window. In this chapter, the structure, electronic and optical properties of VO_2 are briefly introduced.

5.1 Crystal structure

VO_2 belongs to the vanadium-oxygen system, as shown in Fig. 5.1. This system is complex due to the multivalent vanadium ion but also contains a very wide range of ordered and disordered defect structures [63]. These defect structures result in the large range of stoichiometry of vanadium oxides and the existence of the homologous series of separate oxides with the general formula V_nO_{2n-1} between V_3O_5 and VO_2. This latter series can be visualized to be composed of blocks of the parent VO_2 lattice bounded by defect places caused by the removal of every *n*th plane of anions.

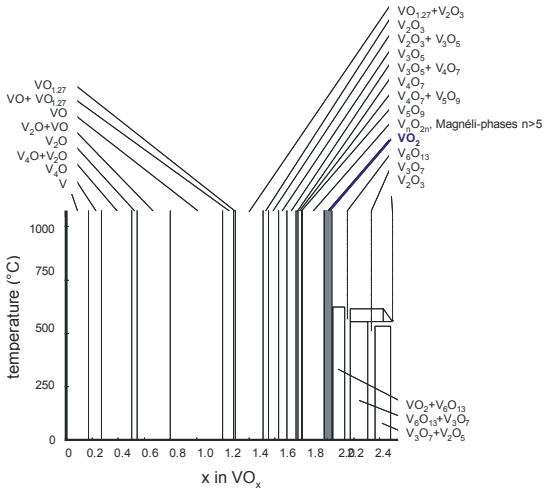

Figure 5.1 The phase diagram of vanadium oxygen system.

Figure 5.2 shows the structures of VO_2 in both metallic and semiconducting phases [16, 23, 64]. The semiconducting monoclinic phase of VO_2 (space group: $P2_1/c$) is characterized by a pairing of vanadium atoms along the c axis resulting in a doubling of

the unit-cell size; along the c axis one finds alternatively short and long metal-metal distances; at the same time, each vanadium "pair" is tilted with respect to the c axis, the vanadium atoms being no longer at the center of the distorted ligand octahedron.

The rutile structure belongs to the nonsymmorphic space group $P4_2/mnm$. The metal atoms form a body-centered-tetragonal array, with two vanadium atoms per unit cell; each is surrounded by a distorted octahedron of oxygen atoms in D_{2h} point-group symmetry. These octahedra share an edge along the c plane, whereas the octahedra surrounding the vanadium atoms at the corner and at the center of the cell share a common corner. Table 5.1 lists the crystal structure and the lattice constants of VO_2 in both phases.

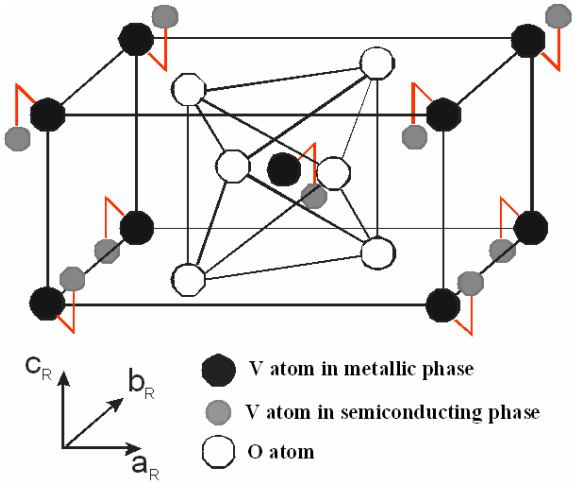

Figure 5.2 Crystal structure of VO_2.

Table 5.1 Summary of crystal structure, space group, and lattice constants of VO_2 in two phases.

Phase	Space group (class)	Lattice constant (Å)
monoclinic distorted rutile structure	$P2_1/c$ (14)	a = 5.751, b = 4.537, c = 5.382
tetragonal rutile structure	$P4_2/mnm$ (136)	a= b = 4.554, c= 2.855

5.2 Electronic properties

The band structure of VO_2 was extensively investigated from 1970 [16, 64-67]. In the metallic phase, the fivefold-degenerated d levels of the $V^{4+}(3d^1)$ ion are first split into

doubly degenerate e_g levels and triply degenerate t_{2g} levels in the octahedral crystal field. The e_g orbitals are strongly hybridized with the O 2pσ orbitals and have a large bandwidth. The V $3d_{3z-r}^2$ and $3d_{x}^2{}_{-y}^2$ orbitals point towards the ligands and form σ and σ* bands with the O 2p orbitals. The t_{2g} orbital $d_{x}^2{}_{-y}^2$ gives rise to a band $d_{||}$, whereas the other two t_{2g} orbitals (d_{xz} and d_{yz}) mix with the O 2p orbital fomring a wider π* band. The t_{2g} levels are further split into the $d_{||}$ and π* levels by the orthorhombic component of the tetragonal crystal field. Thus the $d_{||}$ and π* bands are situated at the lowest energies around the Fermi level. Since the π* orbitals are more hybridized with the O 2pπ than the $d_{||}$ orbitals, the π* bands have higher energies and a wider bandwidth. On the otherhand, the $d_{||}$ orbitals are rather nonbonding. Thus the $d_{||}$ and π* bands overlap at the Fermi level as shown in the schematic diagram in Fig. 5.3.

In the semiconducting phase, however, VO_2 has a monoclinic structure, where the pairing of the vanadium atoms along the c_r axis occurs as shown in Fig 5.2. Because of the change in the V-O hybridization, the energy of the more hybridized π* band rises above the Fermi level and becomes empty. Furthermore, the $d_{||}$ band is split into two states by the pairing of the vanadium ions along the c_r axis.

The metal-semiconductor transition in VO_2 appears to be remarkably complex and its origins are still not yet fully understood. Some argued the low temperature monoclinic phase is a Mott-Hubbard insulator [68], but others regarded it as an ordinary band (Peierls) insulator [69].

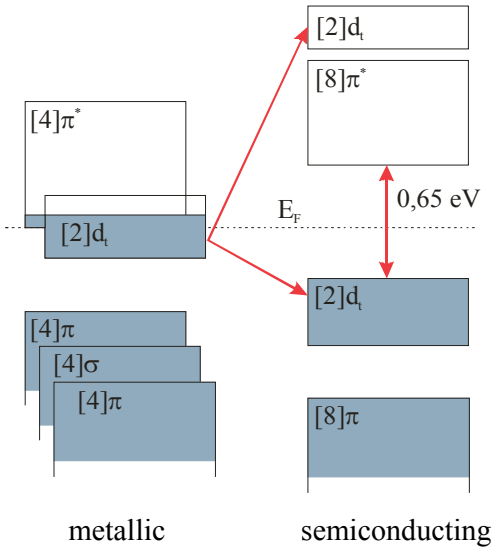

Figure 5.3 Schematic energy diagram of 3d bands around the Fermi level for VO_2.

5.3 Optical properties

As mentioned in chapter 1, VO_2 shows a big difference in optical transmittance below and above the transition temperature, as shown in Fig. 5.4. In the semiconducting phase, it has high transmittance due to the low free carrier concentration. The free carrier concentration increased a lot in the metallic phase. Consequently, the transmittance in the IR decreased. Here we define several parameters, λ_k, which is the maximum of the derivative of the transmittance of the metallic phase, representing the wavelength of optical absorption; T_{lum}, as defined in chapter 1, the transmittance of the semiconducting phase in the visible range; T_s and T_m, the transmittance of VO_2 of the semiconducting and metallic phases in the wavelength range of 250 to 3000 nm, respectively; and Q, the switching efficiency between two phases ($Q=T_s-T_m$), evaluating the switching behavior of VO_2 thin films.

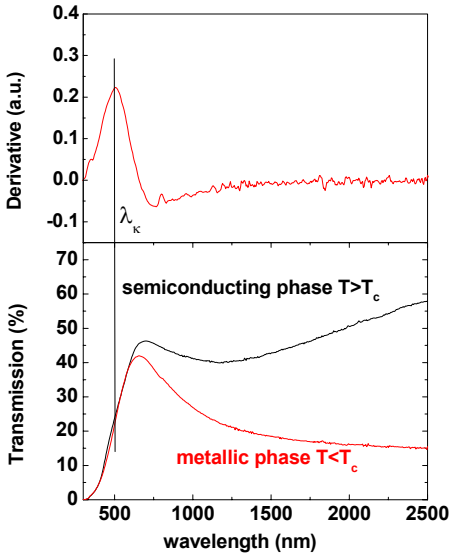

Figure 5.4 The transmittance spectra of a VO_2 film below and above the transition temperature (lower part of the figure). λ_k is set to the maximum of the derivative of the transmittance of the metallic phase (upper part).

Chapter 6 Li/H doping and thermal stability of VO_2 thin films

As mentioned in chapter 1, in order to make VO_2 thin films suitable for the application as smart window, the luminous transmittance of VO_2 thin films should be increased as high as possible and the color should be varied from green/yellow into blue or colorless. Several groups have tried to deposit antireflection layers, such as TiO_2, ZrO_2, SiO_2, etc., on the VO_2 layer to improve the luminous transimittance. However, the films still keep the original color. M. S. R. Khan et al. claimed that the VO_2 thin film was blueish and its luminous transmittance increased after the electrochemical lithiation [20]. According to the theoretical calculation, the band structure of Li_2O is very simple. The valence band is mostly formed from the oxygen 2p state, and the conduction band from the oxygen 3s state; there is no appreciable contribution of lithium to these two bands. The band gap is direct at the *G* point and the band-gap energy is 7.99 eV [70]. From this point, the band gap of VO_2 may increase after Li doping into VO_2. It may be the reason that the absorption edge of Li_xVO_2 films prepared by M. S. R. Khan et al. blue shifted.

In this chapter, Li and H were tried to dope VO_2 thin films by reactive sputtering. As we know, the melting point of Li and V is 180 and 3410 ^oC, respectively. The difference in the melting points is so huge that it is hard to make the Li-V alloy target. So here two kinds of target were used: the V target with Li foil and VO_2: Li_2O targets (Li/V =0.1and 0.28). For the H doping, V and VO_2 targets were applied and Ar, O_2 and H_2 were input into the chamber at the same time.

In addition, the thermal stability of VO_2 thin films is also an important issue that one should address for applications. Some work has been done on the annealing behavior of VO_2 thin films [71-75]. But they focused on the annealing of VO_2 films in Argon or vacuum with very low O_2 pressure, quite different from air as the usual working atmosphere. In the present work, the air-annealing of the as-prepared VO_2 thin films at different temperatures was performed to investigate the thermal stability. In comparison, the vacuum-annealing behavior of VO_2 films is also discussed.

6.1 Li doping

6.1.1 Li doping by the V target with Li foil

The V target with Li foil was used first. Since Li has such low melting point that it can be reevaporated easily during sputtering if the substrate temperature is high enough. In order to avoid the loss of Li during sputtering, the substrate temperature was kept between 60 and 120 ^{o}C. According to the previous work in our group [76], at such low substrate temperatures, a TiO_2 buffer layer should be first deposited on the substrate (float glass) in order to maintain the switching efficiency of VO_2 thin films sputtered. The parameters for the deposition of TiO_2 and Li_xVO_2 layers are shown in table 6.1.

Table 6.1 The parameters for the deposition of TiO_2 and Li_xVO_2 layers.

Film	Target	Sputter power (W)	Temperature (^{o}C)	Sputter time (min)	Gas flow (sccm)	
					Ar	O_2
TiO_2	Ti	300	200	20	3.4	1.36
Li_xVO_2	V with Li foil	300	60~120	20~24	3.5	1.20

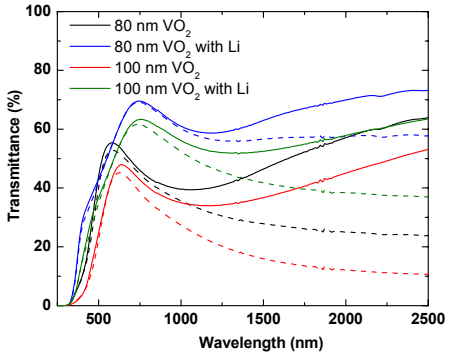

Figure 6.1. The transmittance spectra at 20 (solid lines) and 70 ^{o}C (dashed lines) for VO_2 and Li_xVO_2 thin films with different thicknesses.

Figure 6.1 shows the transmittance spectra at 20 and 70 ^{o}C of VO_2 and Li_xVO_2 thin films with different thicknesses. In this chapter the transmittance spectra at 20 and 70 ^{o}C are depicted by the solid and dash lines, respectively, if not stated otherwise. The transmittance of VO_2 layers increases after the Li doping. The layers turned to blueish

from the original yellow color. Unfortunately, there is too much loss of the switching efficiency after the Li doping. Taking the 100 nm-VO_2 thin film as an example, after the Li doping, λ_k, the maximum of the derivative of the transmittance of the metallic phase, decreases from 502 to 396 nm; the luminous transmittance T_{lum} increases from 36% to 44% and Q, the switching efficiency, decreases from 6.4% to 3.5%.

The transmittance at 2000 nm vs. temperature for VO_2 and Li_xVO_2 thin films with the thickness of 100 nm is shown in Fig. 6.2. From this figure, the transition temperature of the pure VO_2 thin film can be calculated to be 52 and 44 ^oC for the heating and cooling processes, respectively. The transition temperature of the Li doped VO_2 thin film in both processes is around 44 ^oC. It means that the Li doping causes the decrease of the transition temperature of VO_2 films.

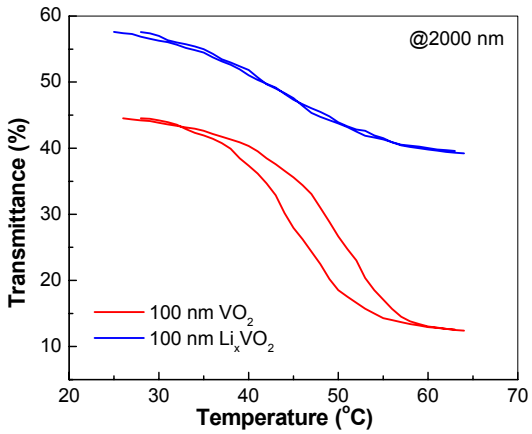

Figure 6.2. The transmittance at 2000 nm vs. temperature for VO_2 and Li_xVO_2 thin films.

From the above discussion, it can be realized that the Li doping in VO_2 thin films indeed increases the transmittance and blue shifts the absorption edge. More systematic work should be performed to investigate how the Li content affects the switching property of VO_2 thin films. Although Li is doped into VO_2 thin films here by using the V target with Li foil, it is too difficult to control the Li content in VO_2 thin films due to the low melting point of Li. So we turn to the ceramic target.

6.1.2 Li doping by VO_2:Li_2O targets

In the last section, we have attempted to dope Li into VO_2 thin films by using the V target with Li foil. Due to the difficulty in controlling the Li content in VO_2 thin film, we should use the ceramic target. Usually, VO_2 thin films are deposited by using V target. There are few investigations on the deposition of VO_2 layers by using the ceramic target. The only work is from Y. Shigesato et al. who deposited thermochromic VO_2 films by using V_2O_3 and V_2O_5 targets with the introduction of oxygen/Argon and hydrogen/Argon, respectively [77]. But they just presented the transmission spectra of the very thick VO_2 film (440 nm). There existed other vanadium oxides in thinner VO_2 films. In our experiments, before VO_2: Li_2O targets were used for sputtering, the pure VO_2 target was studied first.

6.1.2.1 Pure VO_2 target

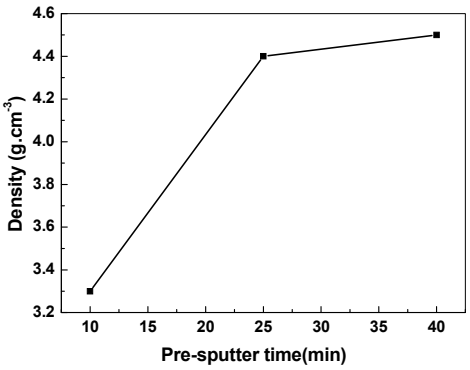

Figure 6.3. The density of the sputtered films as a function of the pre-sputter time.

As we know, for the ceramic target, some gases may be adsorbed on it so that long time pre-sputtering is necessary. Figure 6.3 shows the density of the sputtered films on float glass (sputter power: 200 W; sputter time: 15 min; sputter gas: 10 sccm Ar) with the change of the pre-sputter time by using the pure VO_2 target. It can be seen that the density of the film after 10 min-pre-sputtering is only 3.29 g/cm^3, much lower than the bulk value of VO_2, 4.34 g/cm^3. Only after 25 min-pre-sputtering, the density of the sputtered films gets almost constant. That means that the pre-sputter time should be not less than 25 min for this VO_2 target otherwise the sputtered films will be inhomogeneous. As a consequence, in the case of this ceramic target, all the films were deposited on float glass

after 25 min-pre-sputtering. The parameters for the deposition of VO_2 thin films are listed in Table 6.2.

Table 6.2 The parameters for the deposition of VO_2 thin films with the VO_2 target.

Film	Target	Sputter power (W)	Temperature (^oC)	Sputter time (min)	Gas flow (sccm)	
					Ar	O_2
80 nm VO_2	VO_2	200	500	40	10	0.35
80 nm VO_2	VO_2	300	500	30	10	0.58

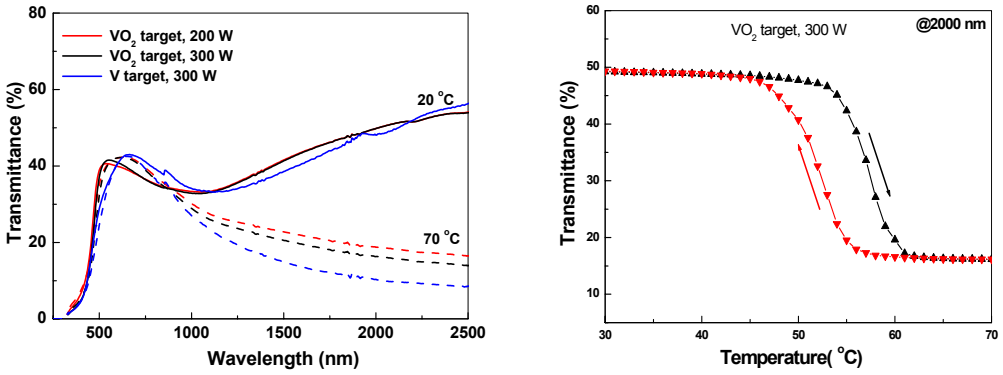

Figure 6.4. The transmittance spectra at 20 and 70 ^oC and transmittance at 2000 nm vs. temperature for 80 nm- VO_2 films by using VO_2 and V targets.

Figure 6.4 shows the transmittance spectra and transmittance at 2000 nm vs. temperature for 80 nm VO_2 films by using VO_2 and V targets. We can see that the switching property of VO_2 films sputtered from the VO_2 target is a little poorer than that from the V target. The transition temperature of VO_2 layers from VO_2 target in the heating process is 58 ^oC, a little lower than that from V target (~60 ^oC). Both the decrease of the switching efficiency and transition temperature should be caused by the introduction of the impurities of the VO_2 target. After all, it is much easier to remove the impurities from the metallic target than from the ceramic target by the pre-sputtering.

In conclusion, we have demonstrated that VO_2 thin films can be prepared by using the VO_2 target. In comparison with the film sputtered from the V target, the VO_2 thin film sputtered from the VO_2 target has poorer switching efficiency and lower transition temperature.

Next, VO_2:Li_2O targets were applied for sputtering. Here two VO_2: Li_2O targets with the mass ratio of Li_2O to VO_2 of 2 and 5 % were used. They are labelled as 2 % and 5 %

targets. Based on the mass ratio the atomic ratio of Li to V in these two targets can be calculated to be 0.11 and 0.28, respectively.

6.1.2.2 The VO_2: Li_2O target (2%)

Three kinds of substrate, float glass, float glass with 80 nm-ITO buffer layer and float glass with 20 nm-TiO_2 buffer layer (for simplicity, they are called float glass, ITO and TiO_2, respectively) were used. Table 6. 3 shows the parameters for the deposition of Li_xVO_2 films with the 2 % target.

Table 6.3 The parameters for the deposition of Li_xVO_2 layers with the 2 % target.

Film	Target	Atomic ratio of Li to V	Sputter Power (W)	Gas flow (sccm)	
				Ar	O_2
Li_xVO_2	VO_2: Li_2O (2%)	0.11	200	5.0	0.45
			300	5.0	0.60

6.1.2.2.1 Optical analysis

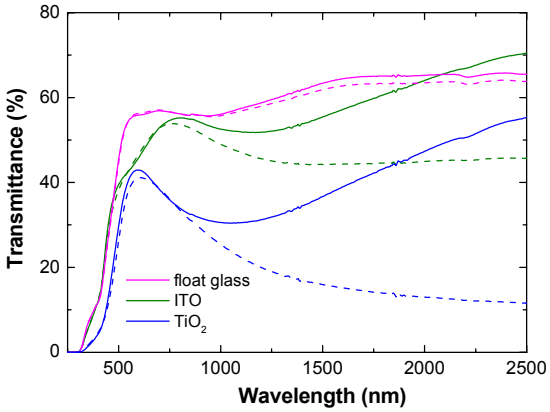

Figure 6.5. The transmittance spectra at 20 and 70 °C of the films sputtered at 300 °C on different substrates.

Figure 6.5 shows the transmittance spectra of the films sputtered at 300 °C on float glass, ITO and TiO_2 for 20 min. In agreement with the previous results, the film does not switch on bare float glass and just shows weak switching on ITO. Only the film on TiO_2 shows the similar switching behaviour as pure VO_2 films.

Figure 6.6 shows the change of density and thickness of the sputtered films on float glass and TiO_2 with the substrate temperature. For the sputtered films on TiO_2, their density, a little higher than that of bulk VO_2, keeps almost constant with the variation of the deposition temperature. However, the density of the sputtered films on float glass increases with increasing deposition temperature. When the substrate temperature is equal or lower than 300 ^oC, the density is only about 3.0 g/cm^3 and the thickness is about 90 nm. Above 300 ^oC, the density increases up to 4.4 g/cm^3 and the thickness decreases to about 55 nm. As we know, Li is a very light element. If Li is doped in the VO_2 thin film, the density of the film should not change unless the structure varies. In this case, our results indicate that the sputtered films on TiO_2 keep the structure of VO_2 but the films on float glass only keep the structure of VO_2 at the substrate temperature equal or higher than 400 ^oC. Otherwise, it transforms into some other structure.

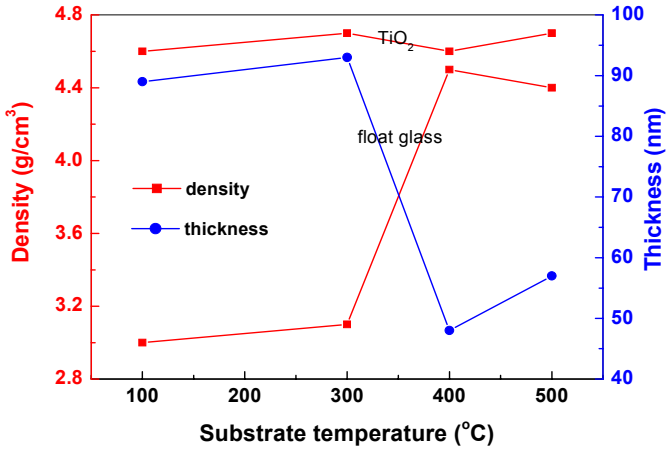

Figure 6.6. The change of the density and thickness of the sputtered films on float glass and TiO_2 with the substrate temperature.

Figure 6.7 shows the transmittance spectra and the transmittance at 2000 nm vs. temperature for the films sputtered on float glass at different temperatures. The films deposited below 300 ^oC do not switch, as depicted in Fig. 6.5. Only when the deposition temperature is higher than 300 ^oC, the sputtered film begins to show weak switching. From the transmittance at 2000 nm vs. temperature, it can be calculated that the transition temperature of the Li_xVO_2 film deposited at 400 ^oC is 51 and 45 ^oC for the heating and cooling process, respectively.

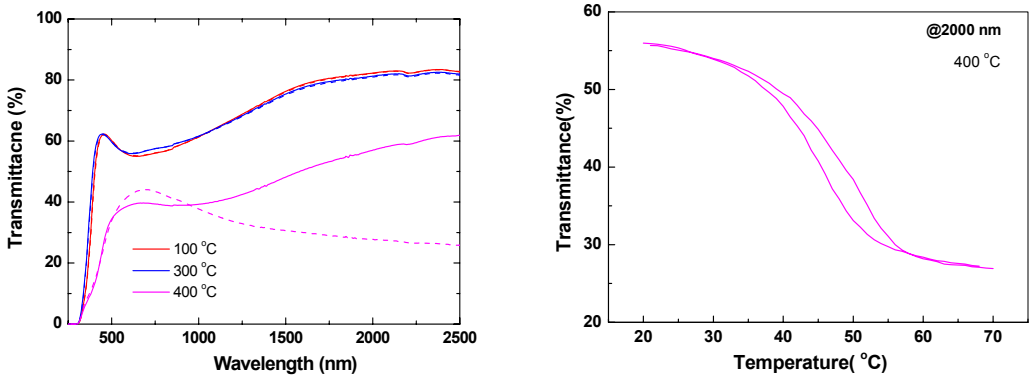

Figure 6.7. The transmittance spectra at 20 and 70 °C (left) and transmittance at 2000 nm vs. temperature (right) of the films sputtered on float glass at different substrate temperatures.

Figure 6.8 shows the transmittance spectra and transmittance at 2000 nm vs. temperature for Li_xVO_2 films deposited on TiO_2 at 400 and 100 °C. The film sputtered at low substrate temperature just shows a little increase of the luminous transmittance and a little decrease of the transition temperature. This change may result from the increase of Li content in the film deposited at 100 °C, which will be discussed later.

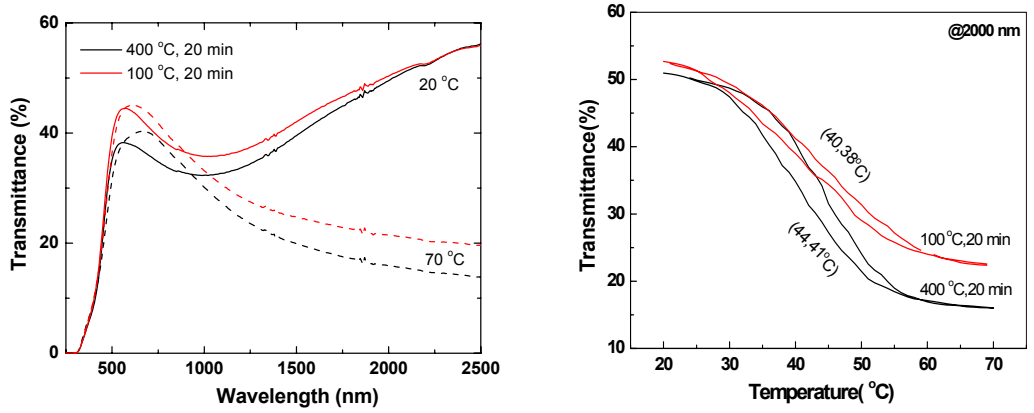

Figure 6.8. The transmittance spectra (left) and transmittance at 2000 nm vs. temperature (right) of Li_xVO_2 films sputtered on TiO_2 at different substrate temperatures.

Figure 6.9 shows the transmittance spectra and transmittance at 2000 nm vs. temperature for Li_xVO_2 films deposited on TiO_2 at 400 °C for different time. The film with short sputter time just shows an increase of the transmittance in the whole range and a little decrease of transition temperature. This is in good agreement with previously published results [78].

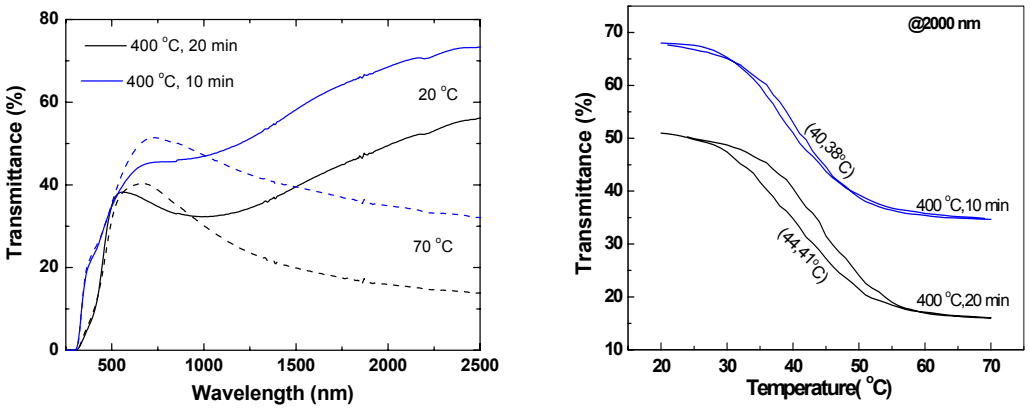

Figure 6.9. The Transmittance spectra (left) and transmittance at 2000 nm vs. temperature (right) of sputtered Li_xVO_2 films on TiO_2 at 400 °C with different sputter time.

6.1.2.1.2 SIMS analysis

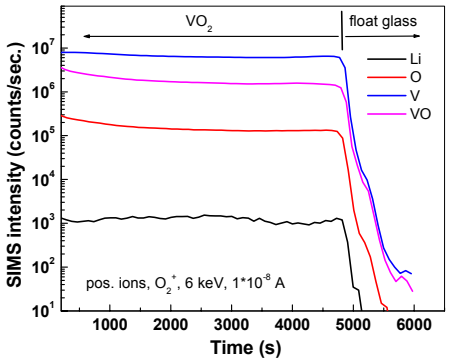

Figure 6.10. The depth profile of a pure VO_2 thin film on float glass.

The depth profiles of the sputtered layers were measured by SIMS. Figure 6.10 shows the depth profile of a pure VO_2 layer on float glass. As one can see, the elements V and O are homogeneously distributed through the layer. The intensity of Li in the VO_2 layer, diffused from the substrate is very low. After the Li doping into the VO_2 layers on TiO_2 and float glass, the depth profiles are varied, as shown in Fig. 6.11. The intensity of the Li signal keeps almost constant through the whole thickness of the layer on TiO_2. In the layer deposited directly on float glass, the intensity of the Li signal increases towards the interface and then decreases in float glass. The intensity ratio of Li to V in these two layers is shown in Fig. 6.12. It shows that the Li content is much higher in the sputtered layer on

TiO_2 than that on float glass. That means that a TiO_2 buffer layer is helpful to avoid the reevaporation of Li from the substrate besides to lower the deposition temperature of VO_2 thin films.

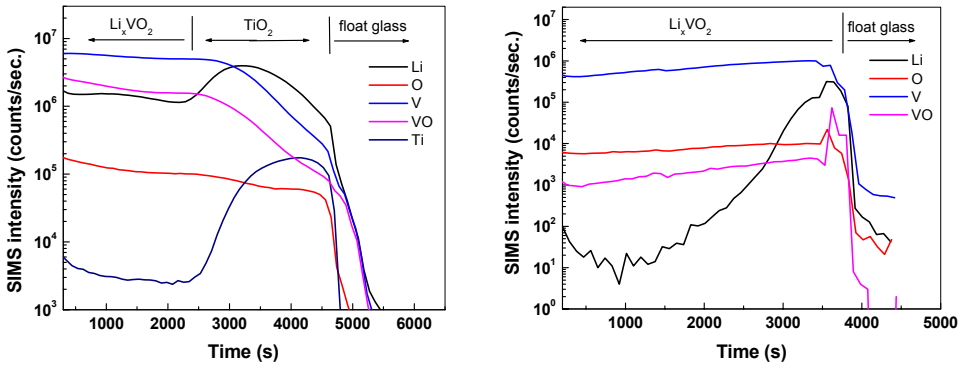

Figure 6.11. The depth profiles of Li_xVO_2 layers on TiO_2 (left) and float glass (right) at about 100 ^oC.

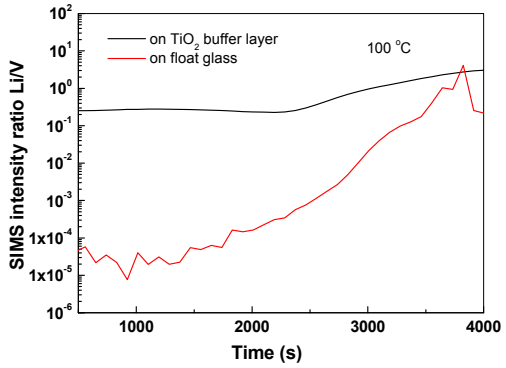

Figure 6.12. The intensity ratio of Li to V for the sputtered Li_xVO_2 layers on float glass and TiO_2.

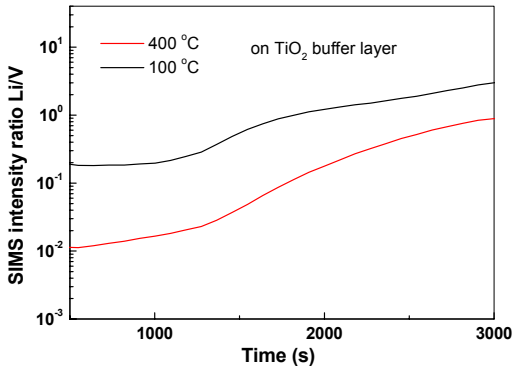

Figure 6.13. The change of the intensity ratio of Li to V for Li_xVO_2 layers sputtered at 400 and 100 ^oC.

Figure 6.13 represents the change of the intensity ratio of Li to V for the sputtered layers with the substrate temperature. Obviously, the intensity ratio of Li to V in the layer deposited at lower temperature is higher. It is reasonable because the layer prepared at higher temperature has lost more Li due to the reevaporation during sputtering.

6.1.2.3 The VO_2: Li_2O target (5%)

From last section, it is clear that by using the 2% target the Li content in VO_2 is not high enough to increase the transmittance significantly. A target with higher Li content, VO_2: Li_2O target with the mass ratio of Li_2O to VO_2 of 5%, therefore, was applied for sputtering. In this case, only float glass and TiO_2 were used as substrate.

Figure. 6.14 shows the transmittance spectra of the sputtered films on TiO_2 at 100 and 400 ^oC with different O_2 flows. At 100 ^oC, with the increase of the O_2 flow, the luminous transmittance and switching efficiency increase. Further increase of the O_2 flow, the luminous transmittance continuously increases but the switching efficiency deteriorated rapidly. The same phenomenon occurs in the layers deposited at 400 ^oC.

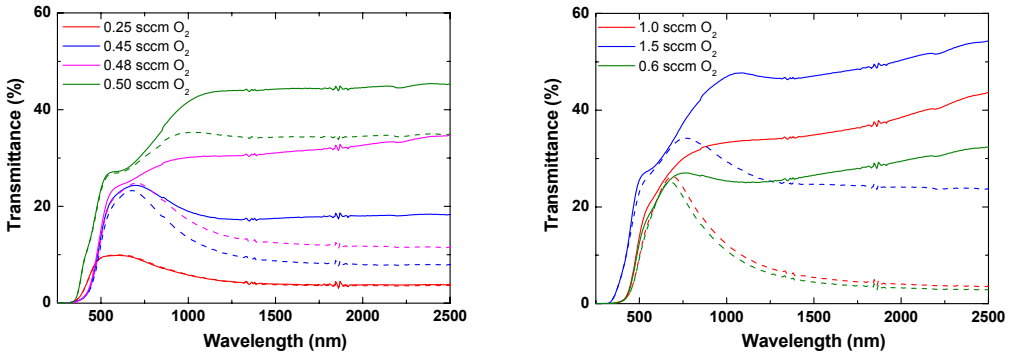

Figure 6.14. The transmittance spectra at 20 and 70 ^oC of sputtered Li_xVO_2 films on TiO_2 at 100 (left) and 400 ^oC (right) with different O_2 flows (Ar flow was fixed at 5.0 sccm).

The conten of Li in the films was measured by ERDA. Figure 6.15 shows depth profile of a Li_xVO_2 film prepared on float glass at 100 ^oC. The atomic density of Li in the film is inhomogeneous, in good agreement with Fig. 6.11. We can roughly divide it into two parts: A and B. The atomic ratio of Li to V in part A and B is calculated to be 3.2 and 5.6 %, respectively, much lower than the value of 28 % in the target. According to the ref.

[20], only high Li content in VO_2 thin films caused the significant increase of the transmittance. Around 5% content of Li in VO_2 layer in our case does not bring a big increase of the transmittance.

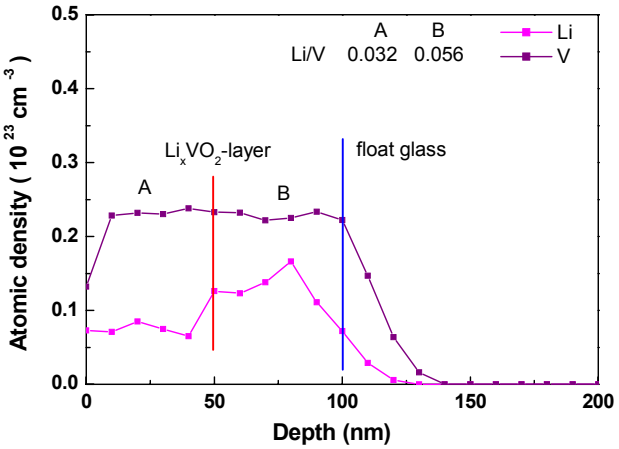

Figure 6.15. The depth profile of a Li_xVO_2 film prepared on float glass at 100 ^oC measured by ERDA.

6.1.3 Conclusion

We have demonstrated how to dope Li into VO_2 thin films by using V and VO_2:Li_2O targets. The results by using the V target with Li foil show the Li doping indeed increases the transmittance and blue shifts the absorption edge of VO_2 films. More systematic work on investigating how the Li content affects the switching property of VO_2 thin films is frustrated by the difficult control of the Li content due to its low melting point. In the case of VO_2:Li_2O targets (2% and 5%), TiO_2 as the buffer layer not only helps to decrease the substrate temperature but also avoid the loss of Li during sputtering. Although we can adjust the Li content in VO_2 films by changing the substrate temperature, the Li content is too low to give a significant increase of the transmittance. In order to get higher Li content in VO_2 films, a VO_2: Li_2O target with the content of Li_2O much higher than 5% should be applied.

6.2 H doping

Since the Li doping in VO_2 films increases the transmittance and blue shifts the absorption edge, it is supposed that the doping of H, another element in group I, probably modifies the transmittance spectra of VO_2 thin films in a similar way to the Li doping. The H doping into VO_2 thin films is rather easy in comparison to the Li doping. V and VO_2 targets were used for sputtering. During the sputter process, Ar, O_2 and H_2 were input into the chamber. The flows of Ar and O_2 were fixed at 3.5 and 1.28 sccm for the sputtering of metallic target but at 5.0 and 0.7 sccm for VO_2 target, respectively. The sputter power was 300 W. The substrate was float glass and TiO_2 at the deposition temperature of 500 and 200 ^oC, respectively. Figure 6.16 shows the partial pressure of Ar, O_2 and H_2 in the used range in our sputter chamber. As you can see, the partial pressure of H_2 is of the same order as O_2 in our experiments.

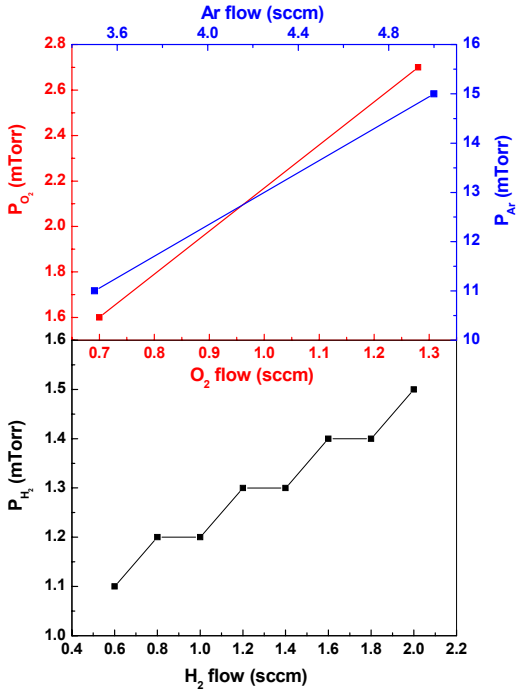

Figure 6.16. The partial pressure of Ar, O_2 and H_2 in our experiment.

6.2.1 Metallic target

At first V target was applied. Before we sputter H doped VO_2 layer, VH_x layers were first deposited to check if H can be bound with V. Figure 6. 17 shows the transmittance spectra and density of VH_x layers with the change of H_2 flow during sputtering. As one can see, the transmittance of the layers first increases with increasing H_2 flow. Further increase of the H_2 flow causes the decrease of the transmittance of the layer. The density of the layers measured by XRR has a similar trend. The density of the sputtered layer without H_2 is about 5.94 g/cm^3, a little higher than the bulk value of 5.8 g/cm^3. With the increase of the H_2 flow, the density first decreases and then increases. From the variations of transmittance and density, it can be concluded that H can be easily bound with V to form some compounds.

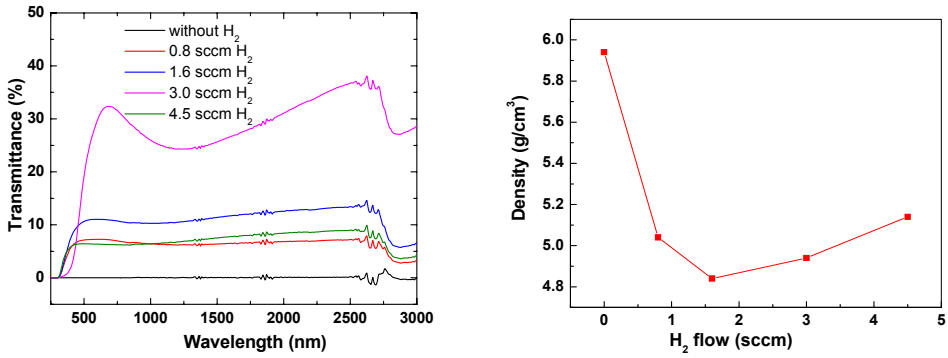

Figure 6. 17. The transmittance spectra (left) and density (right) of VH_x layers with the change of H_2 flow during sputtering.

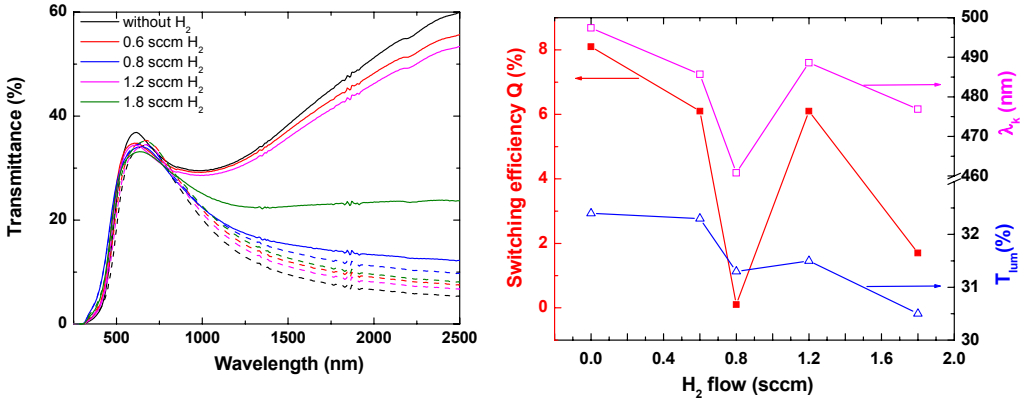

Figure 6.18. The transmittance spectra at 20 and 70 ^oC (left) and corresponding switching characteristics (right) of the deposited H_xVO_2 films at 500 ^oC with the change of the H_2 flow.

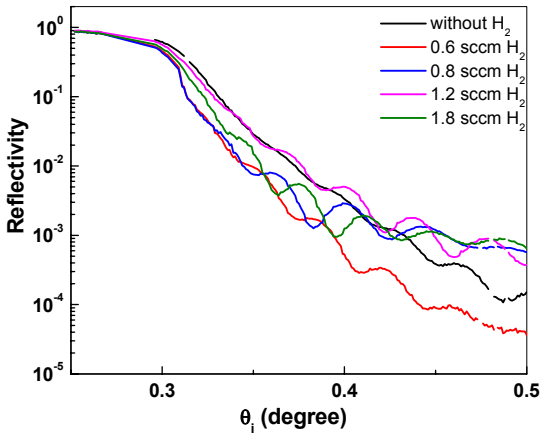

Figure 6.19. The measured reflectivity of sputtered H_xVO_2 films with the variation of H_2 flow.

Figure 6.18 shows the transmittance spectra and corresponding switching characteristics of the deposited H_xVO_2 films at 500 ^oC with the change of the H_2 flow. With the increase of the H_2 flow, Q, T_{lum} and λ_k first decrease and then increase. The density of these films, according to the XRR measurements, has the similar trend, as shown in Fig. 6.19. But the transition temperature always decreases with increasing H_2 flow (as shown in Fig. 6.20).

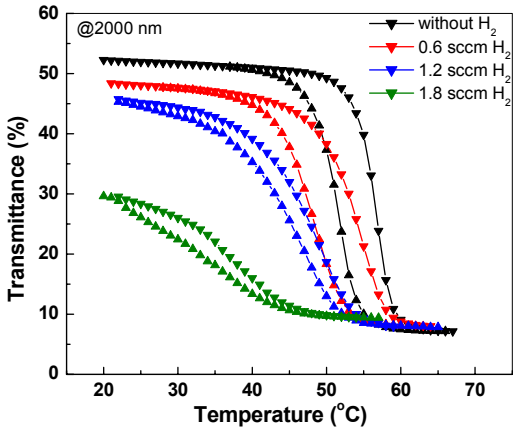

Figure 6.20. The transmittance at 2000 nm vs. temperature of the deposited films.

The films sputtered at 200 ^oC show the similar behavior. Their transmittance spectra and hysteresis are shown in Fig. 6.21. According to the XRR measurement, the film thickness is about 93 nm and the density is about 4.64 g/cm^3, in agreement with the density of the sputtered VO_2 film.

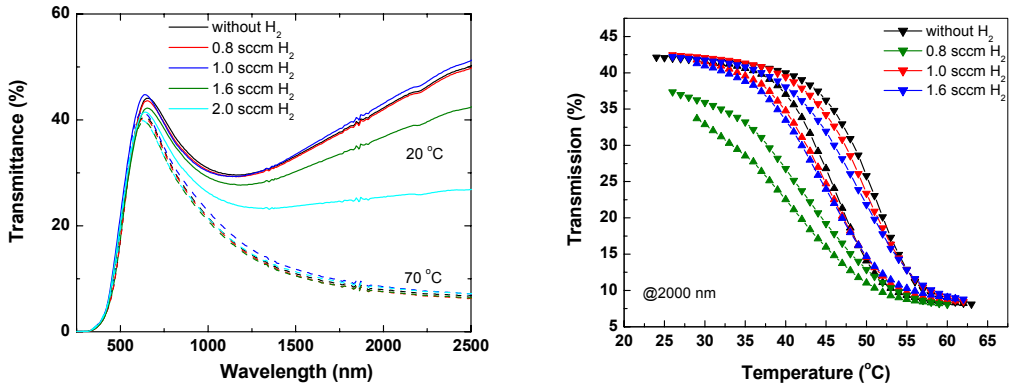

Figure 6.21. The transmittance spectra (left) and hysteresis (right) of the deposited H_xVO_2 films at 200 °C with the change of the H_2 flow.

6.2.2 VO_2 target

Figure 6.22 shows the transmittance spectra and corresponding switching characteristics of the deposited H_xVO_2 films at 500 °C with the change of the H_2 flow. With increase of H_2 flow, the switching efficiency Q and the luminous transmittance of the metallic phase in the visible range T_{lum} first decrease and then increase. The density of these films, according to the XRR measurements, shows the similar behavior to the case of metallic target. But the transition temperature always decreases with increasing H_2 flow (as shown in Fig. 6.23).

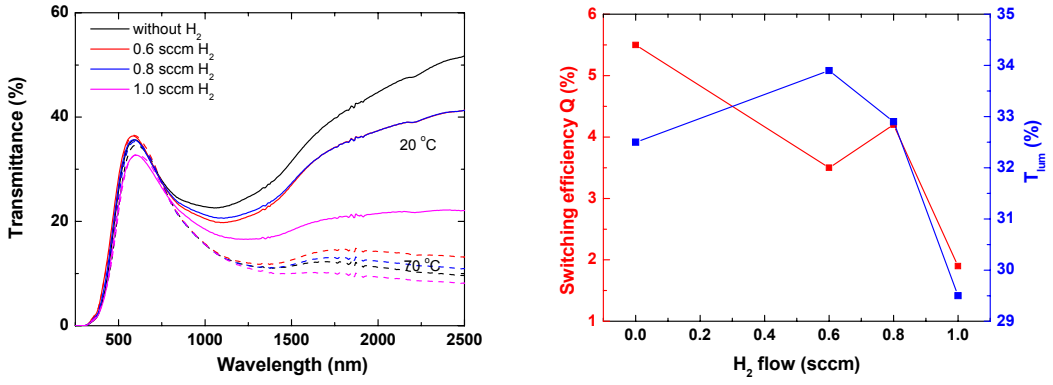

Figure 6.22. The transmittance spectra and corresponding switching characteristics of the deposited H_xVO_2 films at 500 °C with the change of the H_2 flow.

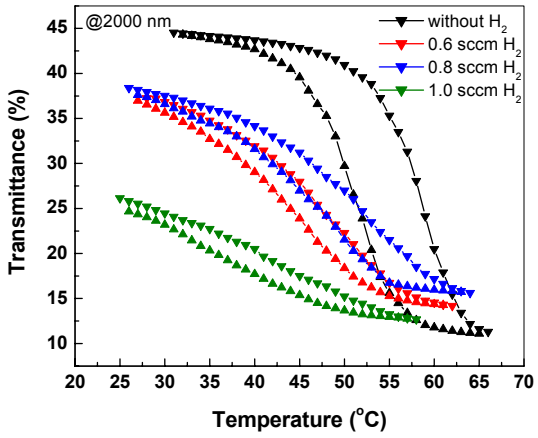

Figure 6.23. The transmittance at 2000 nm vs. temperature of the deposited films.

6.2.3 Conclusion

H was doped into VO_2 thin films by reactive sputtering with V and VO_2 targets. With the increase of the H content in VO_2 films, the transition temperature decreases and the switching characteristics, such as Q, T_{lum} and λ_k only have a little improvement after optimizing the sputter parameters.

6.3 Thermal stability of VO_2 films

6.3.1 Experimental details

In this part, two VO_2 thin film systems were studied. One is a pure VO_2 film with the thickness of 60 nm on float glass, the other is a W doped VO_2 film within a layer system of $Si_xN_y/TiO_2(2)/VO_2$:W/$TiO_2(1)$ on float glass. The two TiO_2 layers and the Si_xN_y layer were deposited as buffer layer, capping layer and antireflection layer, respectively. Pure VO_2 thin films were prepared by radio-frequency reactive sputtering of a pure V target (purity: 99.5%). For W doping three small W rods (99.95%) were screwed into the V target. The TiO_2 and Si_xN_y films were prepared by sputtering of a Ti target and a Si target, respectively. The deposition conditions for VO_2, TiO_2 and Si_xN_y are listed in Table 1. The float glass substrates were ultrasonically cleaned in acetone and methanol for 5 min,

respectively. The chamber was evacuated usually to 10^{-3} Pa before the gases were introduced. The annealing in vacuum was performed at a pressure of 10^{-3} Pa.

Table 6.4. Deposition conditions for VO_2, TiO_2 and Si_xN_y layers.

Film	Target	Power (W)	Pressure (Torr)	Ar (sccm)	O_2 (sccm)	N_2 (sccm)	T_{sub} (^oC)
VO_2	V	300	$1.5*10^{-2}$	3.5	1.31	0	500
W doped VO_2	W doped V	500	$1.5*10^{-2}$	3.5	1.31	0	270
TiO_2	Ti	300	$1.6*10^{-2}$	3.4	1.46	0	210
Si_xN_y	Si	300	$2.5*10^{-2}$	0	0	7.8	230

6.3.2 Results and discussion

Figure 6.24 shows the transmittance spectra and transmittance hysteresis loops measured at 2000 nm for the as-deposited VO_2 thin film before and after annealing in air at 100, 200 and 300 ^oC for 2 h, respectively. The switching efficiency *Q* of the VO_2 thin film after air-annealing at 100 and 200 ^oC shows marginal changes compared with that of the as-deposited VO_2 film. The transmittance hysteresis loops for the three samples are almost same, indicating the unchanged transition temperature. The XRD pattern of the VO_2 film without annealing (in Fig. 6.25) shows only one peak corresponding to the VO_2 (011) reflection. Besides this peak, after annealing at 100 and 200 ^oC for 2 h, a small peak coming from the VO_2 (210) reflection appeared. All these findings indicate the VO_2 thin film is quite stable in air below 200 ^oC. However, after annealing at 300 ^oC for 2 h, the switching property of the film has deteriorated, as seen in Fig. 6.24. Its XRD spectrum (in Fig. 6.25) is composed of two new peaks coming from a V_2O_5 phase. It does mean that during annealing in air at 300 ^oC the VO_2 film was oxidized. The variations of the thickness and the density of the film (shown in Fig. 6.26) are another evidences for oxidization. One can see from Fig. 6.26 that the density and the thickness of the film do not change after the annealing at 100 and 200 ^oC. After annealing at 300 ^oC, the density has decreased and the thickness has increased. Obviously, the variations of the density and the thickness of the film are due to the oxidization of VO_2. Figure 6.27 shows the SEM pictures of VO_2 thin films before and after air annealing at 300 ^oC for 2 h. After oxidization, the film consists of some columnar particles instead of spherical particles. The

interesting thing is that V_2O_5 thin film can be reconverted to VO_2 thin film under a temperature above 400 ^oC and a pressure below 2 Pa in air [79].

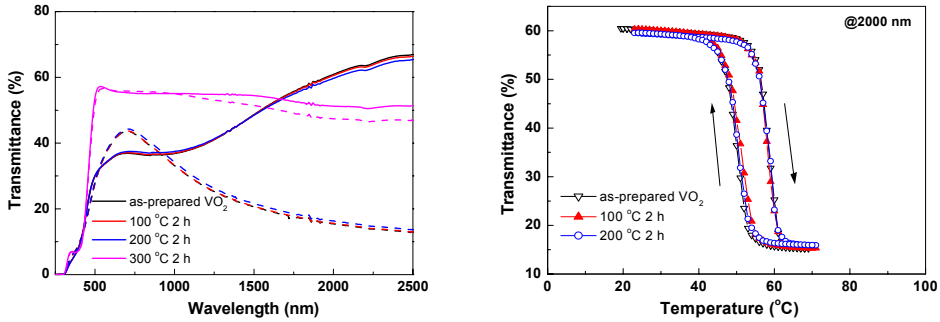

Figure 6.24. The transmittance spectra (left) at 20 and 70 ^oC and transmittance (right) at 2000 nm vs. temperature for a VO_2 thin film without and after annealing in air at 100, 200 and 300 ^oC for 2 h.

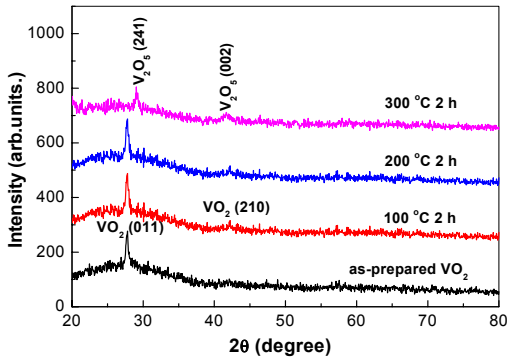

Figure 6.25. XRD patterns of VO_2 thin films before and after air annealing at 100, 200 and 300 ^oC for 2 h.

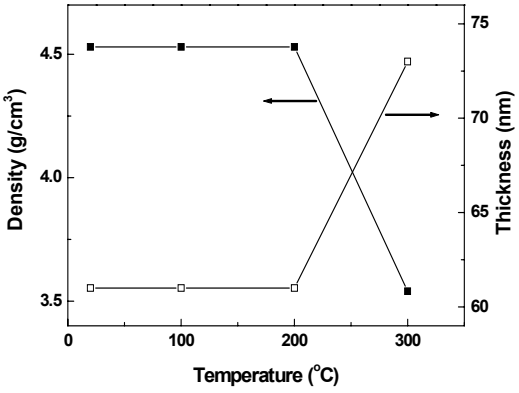

Figure 6.26. The dependence of the density and of the thickness of VO_2 thin films on the annealing temperature.

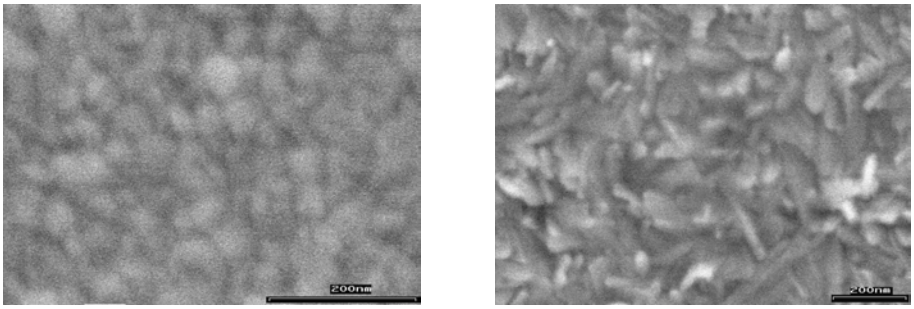

Figure 6.27. The SEM pictures of VO_2 films before (left) and after air annealing at 300 ^oC (right) for 2 h.

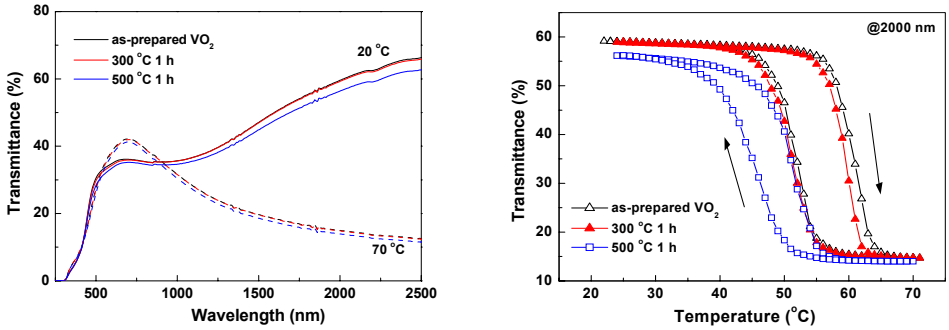

Figure 6.28. The transmittance spectra (left) at 20 and 70 ^oC and transmittance (right) at 2000 nm vs. temperature for VO_2 thin films before and after the annealing in vacuum at 300 and 500 ^oC.

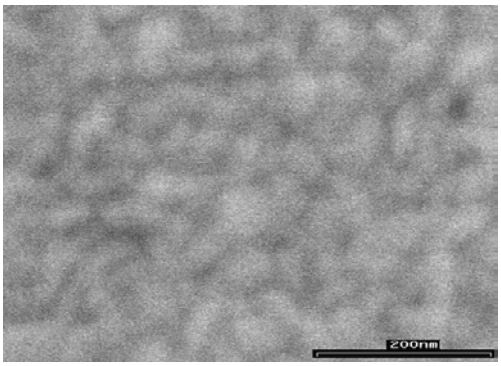

Figure 6.29. The SEM pictures of VO_2 thin films after vacuum annealing at 500 ^oC for 2 h.

For comparsion, vacuum-annealing was conducted on the VO_2 films. Figure 6.28 exhibits the transmittance spectra and transmittance at 2000 nm vs. temperature for an as-deposited VO_2 thin film before and after annealing in vacuum at 300 and 500 ^oC for 1 h, respectively. After annealing at 300 ^oC for 1 h in vacuum, the film does not change the Q and hysteresis behavior. The annealing at 500 ^oC results in a little decrease in the transmittance for both metallic and semiconducting phases, and the transition temperature T_t decreased from 62 to

52 °C. ΔT_t (the difference of the transition temperature during heating and cooling) also lowered from 10 to 4 °C. The decrease of the transmission, T_t and ΔT_t should be related to the increase of the grain size of the VO_2 film. As reported previously, with the increase of the grain size of VO_2 particle, the transition temperature and ΔT_t decreased [80]. Figure 6.29 shows the pictures of VO_2 thin films after vacuum annealing at 500 °C for 2 h. In comparison to Fig. 6. 27, we can see that the particle size of this VO_2 thin film shows little change after the vacuum-annealing at 500 °C for 1h. Probably, the decrease of transition temperature of the VO_2 thin film is caused by the decrease of the residual stress inside the film after annealing at 500 °C, similar to the case of FeS in chapter 4.

For an application of VO_2 films as thermochromic coating, the deposition and the transition temperature of the VO_2 film should be as low as possible. This can be solved by using a TiO_2 buffer layer (deposition temperature can be decreaed to 210 °C) and W doping (transition temperature lowering down to 20 °C) into the VO_2 film. Another TiO_2 layer and a Si_xN_y layer were deposited onto W doped VO_2 layer successively as a capping layer and antireflection layer, respectively, to protect the VO_2 layer and to enhance the transmission in the visible range. The inset of Fig. 6.30 shows the layout of the layer stack. With this structure, the W doped VO_2 layer can be deposited below 300 °C, as seen in Table 6.4, and the transition temperature can be lowered to 33 °C. Figure 6.30 shows the change of transmittance spectra measured at 20 and 60 °C and of hysteresis loop for the sample before and after stored in ambient air for 5 years. There are minor changes, indicating that the sample is very stable at room temperature. Figure 6.31 shows the transmittance spectra of the sample before and after annealing in air at 400 °C. Surprisingly, after annealing at 400 °C only for 10 min, the sample does not longer switching. The depth profiles of the film measured by SIMS, as shown in Fig. 6.32, reveal that for the as-prepared sample, there is a distinct interface between the TiO_2 and the VO_2 layer. After annealing at 400 °C for 10 min, the interfaces smeared out due to the diffusion of Ti into the VO_2 layer and the diffusion of V into the TiO_2 layers. The diffusion of Ti and V changes the composition of the VO_2 film, which is the reason for the deterioration of switching property of the sample.

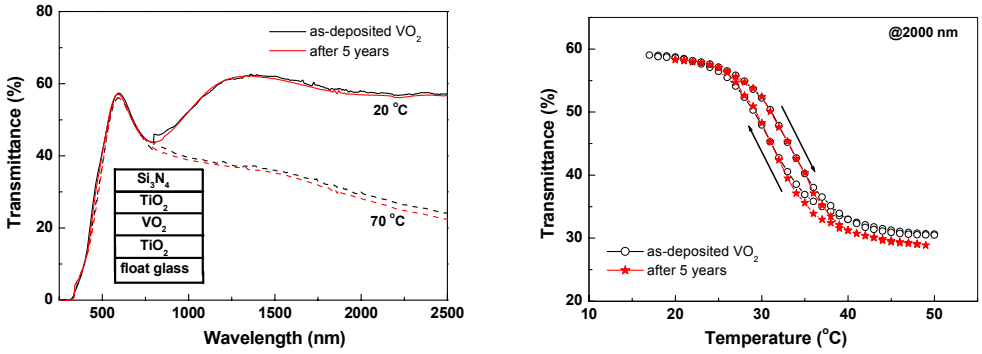

Figure 6.30. The transmittance spectra (left) at 20 and 70 °C and transmittance (right) at 2000 nm vs. temperature of a VO_2 containing layer system of $Si_xN_y/TiO_2(2)/VO_2$:W/$TiO_2(1)$ before and after 5 years in ambient. The inset shows the structure of the layers.

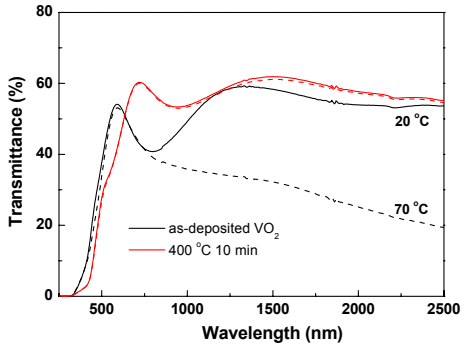

Figure 6.31. The transmittance spectra for VO_2 thin film embedded in a layer system of $Si_xN_y/TiO_2(2)/VO_2$:W/$TiO_2(1)$ after annealing at 400 °C for 10 min.

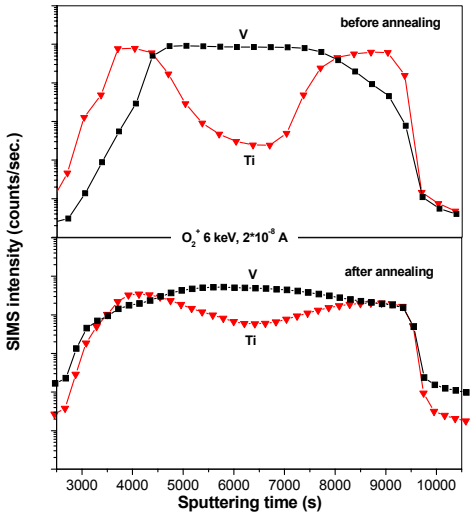

Figure 6.32. Depth profiles of V and Ti in the sample with the structure of $Si_xN_y/TiO_2/VO_2$:W/TiO_2 on float glass before and after annealing at 400 °C for 10 min.

6.3.3 Conclusion

The thermal stability of VO_2 thin films prepared by RF reactive sputtering was investigated. The VO_2 film is stable in air below 200 ^oC. At room temperature the film can keep the switching property at least for 5 years. However, the 2 h-annealing in air at 300 ^oC resulted in the disappearance of the opitical switching of the film due to oxidization. In vacuum, the VO_2 film is quite stable. The annealing in vacuum at 300 and 500 ^oC makes little change of the switching property. For the W doped VO_2 interlayer between two TiO_2 layers, after annealing in air at 400 ^oC for 10 min, the diffusion of V and Ti deteriorated the switching property of the film.

6.4 Summary

In this chapter, we have demonstrated how to dope Li and H into VO_2 thin films by using metallic and ceramic targets. It has been realized that the Li doping increases the transmittance and blue shifts the absorption edge of VO_2 thin films. But due to the low melting point of Li, it is very difficult to control the dopant content in VO_2 thin films by using the V target with Li foil. In the case of VO_2:Li_2O targets (2% and 5%), TiO_2 as the buffer layer not only decrease the substrate temperature but also avoid the loss of Li during sputtering. Although we can adjust the Li content in VO_2 films by changing the substrate temperature, the Li content is too low to give a significant increase of the transmittance. In order to get higher Li content in VO_2 films, a VO_2: Li_2O target with the content of Li_2O much higher than 5% should be applied.

The H doping only shows little increase of the transmittance and blue-shift of the absorption edge of the VO_2 thin films. With the increase of the H content in VO_2 films, the transition temperature decreases and the switching characteristics, such as Q, T_{lum} and λ_k only have a little improvement after optimizing the sputter parameters.

The thermal stability of VO_2 thin films prepared by RF reactive sputtering was investigated. The VO_2 film is stable in air below 200 ^oC. At room temperature the film can keep the switching property at least for 5 years. However, the 2 h-annealing in air at 300 ^oC resulted in the disappearance of the opitical switching of the film due to oxidization. In vacuum, the VO_2 film is quite stable. The annealing in vacuum at 300 and 500 ^oC makes

little change of the switching property. For the W doped VO_2 interlayer between two TiO_2 layers, after annealing in air at 400 ^oC for 10 min, the diffusion of V and Ti deteriorated the switching property of the film.

Chapter 7 Summary

MST materials show the abrupt change of some physical properties. The switching devices triggered by heat, pressure, etc., can be realized by detecting the variation of these physical properties. For example, VO_2 thin film shows different transmittance between the semiconducting and metallic phases. It is one of the most potential materials for the application as smart window. But this application is restricted by the low luminous transmittance and uncomfortable color of VO_2 thin film. Another MST material, FeS, shows an abrupt change on two orders of magnitude in the electrical conductivity at T_α. Accompanied the change of the electrical conductivity, the optical transmittance and reflectance probably changes also. But it has never been investigated. The prerequisite for studying the optical properties is the successful preparation of FeS films.

In the present work, two MST systems, FeS and VO_2 thin films were investigated.

Iron sulfide thin films over a range of composition were prepared by reactive sputtering. The influence of the substrate, sputter power, substrate temperature and stoichiometry on the structure and MST of iron sulfide films was investigated. Iron sulfide films deposited at different temperatures show temperature dependent structure and MST. FeS films on float glass show (110) and (112) orientations when the substrate temperature is 200 and 500 ^oC, respectively. The transition temperature and width of the hysteresis loop determined from the temperature dependent conductivity curves of iron sulfide films decrease with the substrate temperature, which should be caused by the decrease of the residual stress inside the films. The sputter power has little influence on the structure and MST of FeS films. Fe and S excess in FeS films both result in the decrease of the transition temperature and width of the hysteresis loop.

The vacuum-annealing affects the MST of FeS films significantly. When FeS films were annealed below the deposition temperature, the transition temperature decreases; otherwise increases. The residual stress plays an important role during the annealing process. The higher the residual stress inside the FeS films is, the higher the transition temperature of FeS films. With the increase of the annealing temperature, the residual stress in FeS films is first released and then enhances, which gives rise first to the decrease and then increase of the transition temperature of FeS films. This explains why the transition temperature of

FeS films increases with increasing substrate temperature. At high substrate temperatures, the residual stress is higher. Consequently, the transition temperature of FeS films increases.

In addition, the MST of FeS films was influenced by the ambient aging. With the increase of the aging time, the transition temperature first increases and then decreases. The subsequent decrease of the transition temperature is caused by the release of the residual stress inside the FeS films. Why the transition temperature first increases after a certain time of ambient aging is unclear, but it is probably not due to the gas adsorption onto FeS films.

FeS films with different thicknesses were prepared. The correlation between the film thickness (grain size) and the MST switching characteristics of FeS films was established. With the decrease of the grain size, the density of grain boundaries increases, causing the increase of the conductivity of the semiconducting phase. Thicker FeS films contain smaller density of defects, which increases T_α of FeS films.

Finally, some preliminary results of the O doping into FeS films are presented. O was doped into FeS thin films by introducing Ar, H_2S and O_2 into the sputter chamber during the sputter process. With the increase of O content in FeS films, the lattice constants and T_α decrease.

The strategy for improving the luminous transmittance and changing the color of VO_2 film is the Li and H doping. In this work, we have demonstrated how to dope Li and H into VO_2 thin films by using metallic and ceramic targets. It has been realized that the Li doping increases the transmittance and blue shifts the absorption edge of VO_2 thin films. But due to the low melting point of Li, it is very difficult to control the dopant content in VO_2 thin films by using the V target with Li foil. In the case of VO_2:Li_2O targets (2% and 5%), TiO_2 as the buffer layer not only decrease the substrate temperature but also avoid the loss of Li during sputtering. Although we can adjust the Li content in VO_2 films by changing the substrate temperature, the Li content is too low to give a significant increase of the transmittance. In order to get higher Li content in VO_2 films, a VO_2: Li_2O target with the content of Li_2O much higher than 5% should be applied.

The H doping only shows little increase of the transmittance and blue-shift of the absorption edge of the VO_2 thin films. With the increase of the H content in VO_2 films, the transition temperature decreases and the switching characteristics, such as Q, T_{lum} and λ_k only have a little improvement after optimizing the sputter parameters.

The thermal stability of VO_2 thin films prepared by RF reactive sputtering was investigated. The VO_2 film is stable in air below 200 ^oC. At room temperature the film can keep the switching property at least for 5 years. However, the 2 h-annealing in air at 300 ^oC resulted in the disappearance of the opitical switching of the film due to oxidization. In vacuum, the VO_2 film is quite stable. The annealing in vacuum at 300 and 500 ^oC makes little change of the switching property. For the W doped VO_2 interlayer between two TiO_2 layers, after annealing in air at 400 ^oC for 10 min, the diffusion of V and Ti deteriorated the switching property of the film.

Chapter 8 Zusammenfassung

Materialien, die einen Metall-Halbleiter-Übergang (MST – metal semiconductor transition) aufweisen, zeigen bei diesem Übergang abrupte Änderungen einiger ihrer physikalischen Eigenschaften. Daraus ergibt sich die Möglichkeit, schaltende Bauelemente, die z. B. durch Temperatur oder Druck gesteuert werden, zu realisieren.

Beispielsweise zeigt eine VO_2-Schicht unterschiedliches Transmissionsverhalten in der halbleitenden und in der metallischen Phase. Dieses Material hat damit ein hohes Potential für die Anwendung als intelligente Architekturglasbeschichtung. Einschränkungen für den Einsatz ergeben sich aber aus der relativ geringen Lichttransmission und der Farbe der VO_2-Schichten.

Ein weiteres Material mit Metall-Halbleiter-Übergang ist FeS. Eisensulfid ändert bei der Phasenübergangstemperatur seine elektrische Leitfähigkeit abrupt um zwei Größenordnungen. Diese Modifikation kann mit einer Änderung der optischen Transmission und Reflexion von dünnen FeS-Schichten einhergehen, was aber bisher nicht untersucht wurde. Eine Voraussetzung die optischen Eigenschaften zu studieren, ist die erfolgreiche Herstellung von FeS-Filmen.

In der vorliegenden Arbeit wurden die Eigenschaften der zwei MST-Systeme VO_2 und FeS untersucht.

Dünne Eisensulfid-Schichten wurden in einem weiten Kompositionsbereich durch reaktive Kathodenzerstäubung hergestellt. Anschließend wurden die Struktur der Schichten und der Metall-Halbleiter-Übergang in Abhängigkeit von verschiedenen Parametern, wie Art des Substrats, Substrattemperatur, Sputterleistung und Stöchiometrie, studiert. Der Einfluss der Substrattemperatur auf die untersuchten Eigenschaften ist deutlich. FeS-Schichten auf Floatglas sind bei einer Wachstumstemperatur von 200°C in (110)-Richtung und von 500°C in (112)-Richtung orientiert. Die Phasenübergangstemperatur und die Breite des Temperaturintervalls des Übergangs sinken mit der Substrattemperatur, was auf die Verringerung der intrinsischen Verspannungen in den Schichten zurückgeführt werden kann. Abweichungen von der Stöchiometrie, das heißt, Eisen- oder Schwefelüberschuss in den Schichten, resultieren ebenfalls in der Abnahme der Übergangstemperatur und der Breite der Leitfähigkeitshysterese. Die Sputterleistung hat nur geringen Einfluss auf die Struktur und den Phasenübergang der FeS-Filme.

Der Metall-Halbleiter-Übergang von FeS wird durch Tempern der Schichten im Vakuum signifikant beeinflusst. Für Ausheiltemperaturen unterhalb bzw. oberhalb der Depositionstemperatur sinkt bzw. steigt die Phasenübergangstemperatur. Bei diesem Prozess spielen intrinsische Verspannungen eine wichtige Rolle. Je höher die Verspannungen in dem FeS-Film sind, desto höher ist die Phasenübergangstemperatur für diese Schicht. Mit steigender Ausheiltemperatur werden die Verspannungen erst abgebaut und dann wieder erhöht, was erst zu einer Verringerung und dann zu einem Anstieg der Übergangstemperatur führt. Das erklärt auch den Anstieg der Phasenübergangstemperatur für FeS-Schichten, die bei höherer Substrattemperatur abgeschieden wurden und somit stärker verspannt sind.

Zusätzlich wird der Metall-Halbleiter-Übergang von FeS auch durch die Lagerung in Raumluft beeinflusst. In Abhängigkeit von der Alterungsdauer steigt die Übergangstemperatur erst an und sinkt dann wieder. Die Verringerung der Phasenübergangstemperatur kann auf den Abbau der Verspannungen in der FeS-Schicht zurückgeführt werden. Der zuerst beobachtete Anstieg der Übergangstemperatur während der Alterung ist nicht geklärt. Die Gasadsorption auf dem FeS-Film kann als Ursache vermutlich ausgeschlossen werden.

Weiterhin wurde die Korrelation zwischen der Schichtdicke (Korngröße) und den Schalteigenschaften des Metall-Halbleiter-Übergangs von FeS-Schichten untersucht. Mit Verringerung der Korngröße und somit der Erhöhung der Dichte der Korngrenzen steigt die Leitfähigkeit der FeS-Schichten in der halbleitenden Phase an. Die Phasenübergangstemperatur erhöht sich für dickere FeS-Schichten, da sie eine geringere Defektdichte aufweisen.

Schließlich wurden einige Voruntersuchungen zur Sauerstoff-Dotierung von FeS-Filmen durchgeführt. Dabei wurde Sauerstoff als Reaktivgas zusätzlich zu Argon und Schwefelwasserstoff im Sputterprozess zugegeben. Mit Erhöhung des Sauerstoffgehaltes in den Proben verringern sich die Gitterkonstante und die Phasenübergangstemperatur.

Ein Ziel dieser Arbeit war die Verbesserung der Lichttransmission und die Änderung der Farbe von VO_2-Schichten. Dazu wurden Proben mittels Zerstäubung eines metallischen Vanadium-Targets bzw. eines keramischen Vanadiumoxid-Targets hergestellt und mit Lithium und Wasserstoff dotiert.

Die Dotierung mit Li erhöht die Lichttransmission und bewirkt eine Blauverschiebung der Absorptionskante von VO_2. Aufgrund des geringen Schmelzpunktes von Lithium ist es aber sehr schwierig, den Einbau von Li in die VO_2-Schichten mit Hilfe von Li-Folie auf dem Sputtertarget zu kontrollieren. Aus diesem Grund wurden VO_2:Li_2O-Targets mit 2 bzw. 5%

Li_2O-Anteil zur Schichtabscheidung eingesetzt. Es hat sich gezeigt, dass die zur Absenkung der Depositionstemperatur eingefügte TiO_2-Pufferschicht auch den Li-Verlust während des Herstellungsprozesses der VO_2:Li-Probe verringert. Obwohl der Li-Gehalt in den VO_2-Schichten, die von den legierten Targets abgeschieden wurden, über die Änderung der Substrattemperatur eingestellt werden konnte, war die Li-Konzentration zu klein, um eine signifikante Erhöhung der Transmission nachzuweisen. Für eine erfolgreiche Li-Dotierung von VO_2 müssen VO_2:Li_2O-Targets mit deutlich mehr als 5% Li_2O zum Einsatz kommen.
Die Dotierung mit Wasserstoff ergab nur eine geringe Erhöhung der Lichttransmission und Blauverschiebung der Absorptionskante für die VO_2-Proben. Mit der Erhöhung des H-Gehalts im VO_2 sinkt die Phasenübergangstemperatur und die Schalteigenschaften verbessern sich auch nach Optimierung der Prozessparameter nur wenig.

Weiterhin wurde die thermische Stabilität von im RF-Sputterprozess hergestellten VO_2-Dünnschichten untersucht. Eine 5-jährige Lagerung bei Raumtemperatur hat keinen Einfluss auf die Eigenschaften des Phasenübergangs. An Luft sind die Filme bis 200°C stabil, eine 2-stündige Temperung bei 300°C zerstört das optische Schaltverhalten aufgrund der Oxidation der VO_2-Schicht. Eine W-dotierte VO_2-Schicht, die in einem Schichtsystem von 2 TiO_2-Schichten umgeben war, verliert ihr Schaltverhalten nach Ausheilung in Luft bei 400°C für 10 min aufgrund der Diffusion von Ti und V. Nach Temperung bei 500°C für 1 Stunde unter Vakuum zeigen die VO_2-Schichten nur leicht verändertes Schaltverhalten.

References

[1] F. J. Morin, Phys. Rev. Lett. 3, 34 (1959).

[2] D. Adler, J. Feinleib, H. Brooks, W. Paul, Phys. Rev. 155, 851 (1967).

[3] D. Adler, Rev. Mod. Phys. 40, 714 (1968).

[4] S. N. Mott, Rep. Prog. Phys. 47, 909 (1984).

[5] M. Imada, A. Fujimori, Y. Tokura, Rev. Mod. Phys. 70, 1039 (1998).

[6] N. F. Mott, Metal-Insulator Transitions, Taylor & Francis, 1990.

[7] H. W. Verleur, A. S. Barker, Jr., C. N. Berglund, Phys. Rev. B 172, 788 (1968).

[8] H. Jerominek, F. Picard and D. Vincent, Opt. Eng. 32, 2092 (1993).

[9] T. D. Pope, H. Jerominek, etc., Proc. SPIE. 3436 (Pt 1-2), 325 (1998).

[10] C. G. Granqvist, CRC Crit. Rev. Solid-State. Mater. Sci.16, 291 (1990).

[11] C. M. Lampert, Presented at Window Innovation 95, Toronto, Canada, June 5-6, 1995.

[12] M. Tayawa, P. Jin and S. Tanemura, Appl. Opt. 37, 1858 (1998).

[13] P. Jin and S. Tanemura, Jpn. J. Appl. Phys. 34, 2459 (1995).

[14] W. Burkhardt, T. Christmann, etc., Thin Solid Films. 402, 226 (2002).

[15] T. J. Hanlon, J. A. Coath and M. A. Richardson, Thin solid Films. 436, 269 (2003).

[16] J. B. Goodenough, J. Solid. State. Chem. 3, 490 (1971).

[17] M. H. Lee, J. S. Cho, Thin. Solid. Films. 365, 5 (2000).

[18] G. Xu, P. Jin, M. Tazawa, K. Yoshimura, Solar Energy Materials & Solar Cells 83, 29 (2004).

[19] P. Jin, G. Xu, M. Tazawa, K. Yoshimura, Appl. Phys. A 77, 455 (2003).

[20] M. S. R. Khan, K. A. Khan, W. Estrada, C. G. Granqvist, J. Appl. Phys. **69**, 3231 (1991).

[21] J. R. Gosselin, M. G. Townsend, R. J. Tremblay, Solid State Communications, 19, 799 (1976).

[22] Y. B. He, Dissertation: I. Phys. Inst., Justus-Liebig-Universität Giessen, 2003.

[23] M. Theis, Dissertation: I. Phys. Inst., Justus-Liebig-Universität Giessen, 2002.

[24] D. L. Smith, Thin-film deposition: principles and practice, McGraw-Hill, Inc. 1995.

[25] B. Chapman, Glow discharge process, John Wiley & Sons, Inc. 1980.

[26] K. Wasa, S. Hayakawa, Handbook of sputtering deposition technology, Noyes publications, Westwood, New Jersey, USA, 1992.

[27] G. Bauer, W. Richter, Optical characterization of epitaxial semiconductor layers, Springer, 1996.

[28] B. E. Warren, X-ray diffraction, Addison-Wesley Publishing Company, 1969.

[29] O. C. Wells, Scanning Electron Microscopy, McGraw-Hill Book Company, 1974.

[30] D. E. Newbury, D. C. Joy, P. Echlin, C. E. Fiori, J. I. Goldstein, Advanced Scanning Electron Microscopy and X-Ray Microscopy, Plenum Press, New York, 1986.

[31] H. Bubert, H. Jenett, Surface and thin film analysis, Wiley-VCH Verlag, 1992.

[32] R. G. Wilson, F. A. Stevie, C. W. Magee, Secondary ion mass spectrometry; a practical handbook for depth profiling and bulk impurity analysis, John Wiley & Sons, New York, 1989.

[33] J. C. Vickerman, A. Brown, N. M. Reed, Secondary ion mass spectrometry: Principles and applications, Clarendon Press, Oxford, 1989.

[34] J. Tirira, P. Trocellier, J. Radioanal. Nucl. Chem. 130, 311 (1989).

[35] C. F. Klingshirm, Semiconductor Optics, Springer-Verlag Berlin Heiderberg, Germany, 1995.

[36] L. J. van der PAUW, Philips Technical Review. 20, 220 (1958/1959).

[37] H. H. Wieder, Laboratory notes on electrical and galvanomagnetic measurements, Elsevier scientific publishing company, 1979.

[38] E. Hirahara, M. Murakami, J. Phys. Chem. Solids. 7, 281 (1958).

[39] R. C. Thiel, C. B. Van den Berg, Phys. Stat. Sol. 29, 837 (1968).

[40] C. B. Van den Berg, J. E. Van Delden, J. Bouman, Phys. Stat. Sol. 36, K89 (1969).

[41] W. Moldenhager, W. Brückner, Phys. Stat. Sol. (a) 34, 565 (1976).

[42] J. L. Horwood, M. G. Townsend, A. H. Webster, J. Solid. Stat. Chem. 17, 35 (1976).

[43] K. Kusaba, Y. Syono, T. Kikegawa, O. Shimomura, J. Phys. Chem. Solids. 58, 241 (1997).

[44] K. Kusaba, Y. Syono, T. Kikegawa, O. Shimomura, J. Phys. Chem. Solids. 59, 945 (1998).

[45] S. Takele, G. R. Hearne, Phys. Rev. B 60, 4401 (1999)

[46] H. Kobayashi, N. Takeshita, N. Môri, Hiroki, Takahashi, T. Kamimura, Phys. Rev. B 63, 115203 (2001).

[47] H. E. King, C. T. Prewitt, Acta. Crystallogr. B 38, 1877 (1982).

[48] F Li, H. F. Franzen, J. Alloys and Compounds 238, 73 (1996).

[49] S.G. Shyu, J.S. Wu, C.C. Wu, S. H. Chuang, K.M. Chi, Inorganica Chimica Acta. 334, 276(2002).

[50] H. D. Wang, B. S. Xu , J. J. Liu, D. M. Zhuang, Appl. Surf. Sci. 252, 1084 (2005).

[51] I. Lee, I. Park, Surf & Coatings. Tech. 200, 3540 (2006).

[52] T. Drüsedau, J. Bläsing, Thin solid Films 377, 27 (2000).

[53] S. Wu, L. Wu, Y. Shen, F, Chang, Jpn. J. Appl. Phys., Part 1 40, 794 (2001).

[54] M. Clement, E. Lborra, J. Sangrador, A. Sanz-Hervás, L. Vergara, M. Aguilar, J. Appl. Phys. 94, 1495 (2003).

[55] J. Ttpel-Schadt, W. F. Müller, Phys Chem Minerals. 8, 175 (1982).

[56] D. Brassard, S. Fourmaux, M. Jean-Jacques, J.C. Kieffer, M.A. EL Khakani, Appl. Phys.Lett. 87, 051910 (2005).

[57] O. Kruse, American Mineralogist, 75, 755 (1990).

[58] F. Keller-Besrest, G. Collin, J. Solid State Chem. 84, 211 (1990).

[59] F. Keller-Besrest, G. Collin, J. Solid State Chem. 84, 194 (1990).

[60] H.K. Kim, H. You, R.P. Chiarello, H.L.M. Chang, T.J. Zhang, D.J. Lam, Phys. Rev.B 47, 12900 (1993).

[61] G. Collin, M. F. Gardette, R. Comes, J. Phys. Chem. Solids. 48, 791 (1987).

[62] G. Collin, M. F. Gardette, G. Keller, R. Comes, J. Phys. Chem. Solids. 46, 809 (1985).

[63] C. H. Griffiths, H. K. Eastwood, J. Appl. Phys. 45, 2201 (1974).

[64] J. B. Goodenough, H. Y-P. Hong, Phys. Rev. B 8, 1323 (1973).

[65] A. Zylbersaztejn, N. F. Mott, Phys. Rev. B 11, 4383 (1975).

[66] E. Caruthers, L. Kleinman, H. I. Zhang, Phys. Rev. B 7, 3753 (1973).

[67] E. Caruthers, L. Kleinman, Phys. Rev. B 7, 3760 (1973).

[68] R. M. Wentzcovitch, W. W. Schulz, P. B. Allen, Phys. Rev. Lett. 72, 3389 (1994).

[69] S. Biermann, A. Poteryaev, A. I. Lichtenstein, A. Georges, Phys. Rev. Lett. 94, 026404 (2005).

[70] M. Itoh, J. Murakami, Y. Ishii, Phys. Stat. Sol. (b) 213, 243 (1999).

[71] A. Rayavi, L. Bobyak and P. Fallon, J. Vac. Sci. Technol. A 8, 1391 (1990).

[72] M. B. Sahan, G. N. Subbanna and S. A. Shivashankar, J. Appl. Phys. 92, 6485 (2002).

[73] V. A. Klimov, I. O. Timofeeva, S. D. Khanin, E. B. Shadrin, A. V. LL'inskii and F. Silva-Andrade, Semiconductors. 37, 370 (2003).

[74] S. J. Jiang, C. B. Ye, M. S. R. Khan, and C. G. Granqvist, Appl. Opt. 30, 847 (1991).

[75] A. Ilinski, F. Silva-Andrade, E. Shadrin, V. Klimov, J. of Non-Crystal. Solids. 338, 266 (2004).

[76] T. J. Christmann, Dissertation: I. Phys. Inst., Justus-Liebig-Universität Giessen, 1998.

[77] Y. Shigesato, M. Enomoto, H. Odaka, Jpn. J. Appl. Phys. 39, 6016 (2000).

[78] G. Xu, P. Jin, M. Tazawa, K. Yoshimura, Jpn. J. Appl. Phys. 43, 186 (2004).

[79] N. Y. Yuan, J. H. Li, C. L. Lin, Appl. Surf. Sci. 191, 176 (2002).

[80] R. Lopez, T. E. Haynes, L. A. Boatner, L. C. Feldman and R. F. Haglund, Jr., Phys.Rev. B 65, 224113 (2003).

Publications

1) G. H. Fu, A. Polity, W. Kriegseis, D. Hasselkamp, B. K. Meyer, B. Mogwitz, J. Janek, Reactive sputter deposition and metal-semiconductor transitiont of FeS films, **Appl. Phys. A** 84, 309 (2006).

2) Ganhua Fu, Angelika Polity, Niklas Volbers, Bruno K Meyer, Boris Mogwitz, Jürgen Janek, Adjustable metal-semiconductor transition of FeS thin films by thermal annealing, **Appl. Phys. Lett**. 89, 262113 (2006).

3) Ganhua Fu, Angelika Polity, Niklas Volbers, Bruno K Meyer, Annealing effects of VO_2 thin films deposited by reactive sputtering, ***Thin Solid Films*** 515, 2519 (2006).

Acknowledgements

I would like to acknowledge many people for helping me during my doctoral work.

First of all, I would especially like to thank my advisor, Prof. Dr. Bruno. K. Meyer, who provided me the opportunity to work in his active group with open and friendly air. His diligence and creative ideas enlighten me the way to success. He continually stimulated my analytical thinking and greatly assisted me with scientific writing. Without the exceptionally valuable guidance and support I have received from him, this dissertation would not have been possible.

I am also grateful to my day-to-day supervior, Dr. Angelika Polity. She helped me in almost every detail of the doctoral work. She revised all my papers and the dissertation and wrote the Zusammenfassung. Her intrinsic carefulness and patience made them more readable. Without her help, I could hardly finish the work smoothly.

I would like to thank the colleagues: Dr. Eberhard Pitt for helping me get the work contract. Dr. Stefan Merita and Dr. Thorsten Krämer for introducing me the RF sputtering apparatus and helping me solving a lot of problems of this setup; Dr. Wilhelm Kriegsies and Niklas Volbers for SIMS measurements; Swen Graubner and Dr. Daniel Pfisterer for the help in electrical resistivity measurements; Dr. Baker Farangis for helping me register in the university; Prof. Dr. Hasselkamp for RBS measurements; Mrs. Ursula Frisch for the assistance at the XRD and XRR measurements; Mr. Hausner, Mr. Bachmann, Mr. Laudenbach, Mr. Bellof, Mr. Nimmerfroh, et al., in the mechanic and electronic workshops for solving a lot of problems occurred on the RF sputter setup; Mr. Hans Peter Jorde for the assistance in solving computer problems.

I am especially indebted to Changzhong Wang, Dr. Huijuan Zhou, Dr. Bin Yang, Dr. Yunbin He and Yinmei Lu for their help when I arrived in Giessen.

My acknowledgments are also to other members in I. Physikalisches Insisitut for their help and support.

In addition, I would like to thank Dr. Boris Mogwitz in Physikalisch-Chemisches Institut, Justus-Liebig-Universität Giessen for the SEM and EDX measurements and Dr. Ulrich Kreissig in Institut für Ionenstrahlphysik und Materialforschung,

forschungszentrum Rossendorf for the ERDA measurements and Dr. Thomas Wübben in Max-Planck-Institut für Metallforschung for the stress measurements.

Last, but far from least, I thank my parents and my brother for their love and support. I want to express my deep appreciation and love for my wife, Mrs. Yanjie Gan, who has suffered more for this dissertation than anyone. She has endured with selflessness the countless hours of solitude and detachment. I cannot imagine that I could have completed this work without her support.

Ganhua Fu

June 2007
Giessen, Germany